Physical processes in organic solar cells

Physical processes in organic solar cells

PROEFSCHRIFT

ter verkrijging van de graad van doctor aan de
Technische Universiteit Eindhoven, op gezag van de
rector magnificus, prof.dr.ir. C.J. van Duijn, voor een
commissie aangewezen door het College voor
Promoties in het openbaar te verdedigen
op dinsdag 17 december 2012 om 14.00 uur

door

Dominique Joseph Wehenkel

geboren te Luxemburg, Luxemburg

Dit proefschrift is goedgekeurd door de promotor:

prof.dr.ir. R.A.J. Janssen

Copromotor:
dr.ir. M.M. Wienk

Cover photo : Andreas Krappweis, *" Green field landscape",*www.sxc.hu

Printed by CPI Koninklijke Wöhrmann

A catalogue record is available from the Eindhoven University of Technology Library
ISBN: 978-90-386-3294-0

The research was supported by a TOP grant of the Chemical Sciences (CW) division of the Netherlands Organization for Scientific Research (NWO) and is part of the Joint Solar Programme (JSP). The JSP is co-financed by the Foundation for Fundamental Research on Matter (FOM), Chemical Sciences of NWO and the Foundation Shell Research. This work was further supported by the "Europees Fonds voor Regionale Ontwikkeling" (EFRO) in the Interreg IV-A project Organext.

Contents

1 Introduction

Abstract

Organic solar cells are emerging as a viable technology for solar energy conversion as a result of an increase in power conversion efficiency and device stability in combination with the prospect of high-volume, low-cost production using abundant and environmentally benign materials. The focus of the work described in this thesis is to contribute to the understanding of the physical processes that occur in organic solar cells and explore and develop measurement techniques that enable characterizing these devices. This first chapter provides an introduction to the field of organic solar cells and presents a brief review of the history, the state of the art, and the operational mechanisms of these devices. In addition, this chapter introduces the reader to the characterization methods and numerical modeling methods used to interrogate and describe the operation of organic solar cells.

1.1 Organic photovoltaics: A future renewable energy?

The continuous increase in power conversion efficiency of organic photovoltaic (OPV) cells during the three last decades makes that these novel devices are now emerging as a new technology for solar energy conversion. In 1986 C. W. Tang published a first organic bilayer solar cell using complementary electron donor and acceptor organic molecules, exhibiting a power conversion efficiency close to 1% in sunlight.[1] A patent describing these results actually dates back to 1979,[2] at which time the desire to develop new energies was borne out of the 1972 report of the Club of Rome[3] and the 1973 oil crisis.[4] Nowadays the global interest for photovoltaics (PV) has the additional motivation of reducing the emission of carbon dioxide associated with fossil fuels. Since the report of Tang, the certified power conversion efficiency of organic solar cells reached 9.2% for polymer solar cells[5] and 10.1% for proprietary materials.[6] Equally important for future application of OPV, is the fact that there has been a strong increase in the stability of these devices, with reports providing evidence of stabilities of 7 years.[7] These recent developments give increasing credence that OPV can be a viable alternative technology to the present inorganic solar cells. Compared to inorganic solar cells, organic solar cells have the additional advantage that they can be processed at modest temperature from solution, without the need of vacuum, and by fast roll-to-roll (R2R) processes.[8] The organic photoactive materials used in organic solar cells show high absorption coefficients, which makes that only a very thin photoactive layer (100 to 200 nm) is required to absorb sufficient light. Apart from a small amount of organic material needed to fabricate large area solar cells, the materials commonly employed contain abundant and environmentally benign elements like carbon, nitrogen, oxygen, and sulfur, which make them stand out against other new thin film photovoltaic technologies based on polycrystalline CdTe or $Cu(In,Ga)Se_2$ absorber layers. The low temperature, R2R processing of organic solar cells gives the perspective of low cost solar cells with payback times of a few days.[9] Furthermore, fast R2R production of OPV modules −similar to printing newspapers− would enable large area production of OPV cells at very high volume in high manufacturing rates and, compared to silicon solar cells, a reduced capital expenditure. A high production volume is the foremost requirement to meet the future energy demand −the TW challenge− with photovoltaics. Other advantages of OPV cells are that they can be made flexible and lightweight, that they have various colors and can even be transparent to visible light. The lightweight is convenient for off grid power production for application in developing countries such as the one child laptop[10] or solar-lamps.[11] All of these characteristics make that organic solar cells have a promise to become a significant

source of renewable energy, converting the sunlight into electrical energy. However it is clear that, before OPV can be mass produced scientific and technological hurdles regarding efficiency, stability, and production technology must be overcome. The power conversion efficiency and stability of an organic solar cell strongly relies on the physical processes involved in the generation of electricity. Each process, from absorption of light to the generation, transport, and collection of free carriers, is crucial for the efficiency.

This thesis addresses questions regarding physical processes that occur in organic solar cells and the techniques to characterize these novel devices. The aim is to improve our understanding of the operational principles of OPV cells and develop and explore measurement techniques. The work consists of three main parts: First, electro-absorption (EA) spectroscopy is explored as a tool to probe the internal electric fields in the photoactive layers of organic single junction and tandem solar cells. Then, photocurrent measurements on organic solar cells are investigated experimentally and theoretically, which provides new insights in charge recombination mechanisms and reveal conditions that lead to photocurrent multiplication. Finally, the techniques to measure the external quantum efficiency with solar bias illumination are revisited, giving attention to both the intensity and wavelength of the bias light.

The remainder of this chapter provides a further introduction to the field of organic solar cells, outlining the state-of-the art, the working principles, characterization, the modeling and some of the loss mechanisms that presently limit the power conversion efficiency. The last section provides an outline of the thesis.

1.2 Organic photovoltaic cells: a brief review

OPV cells typically consist of a thin organic semiconducting film sandwiched between two electrodes. At least one electrode needs to be transparent such that light can be absorbed by the organic film and transformed into electricity. The organic materials used in OPV cells owe their semiconducting properties to their molecular and electronic structure. Typical organic semiconducting molecules and polymers contain alternating double (−C=C−) and single carbon bonds (−C−C−) that form a conjugated system in which the p_z orbitals on adjacent atoms overlap and cause the valence electrons to delocalize over the entire molecule. The overlapping p_z orbitals yield an occupied π band and an empty π* band, separated by an energy gap. The molecular structures of typical conjugated molecules and polymers are illustrated in Figure 1.1.

The first studied organic solar cell architecture was a homojunction, *i.e.* a single organic material, sandwiched between two electrodes. In 1959, Kallmann and Pope

reported the first homojunction organic solar cell made of a single crystal of anthracene (Figure 1.1).[12] A photovoltage of 200 mV and an extremely low efficiency of 2×10^{-6}% were reported. Much later, solar cells based on organic homojunctions were further improved, but the power conversion efficiency remained below 0.7%.[13,14] The limited performance in homojunction solar cells is related to the low dielectric constant of organic materials −typically around 3 to 4− compared to a dielectric constant above 10 for inorganic materials. Because of the low dielectric constant, absorption of light in organic materials results in the formation of a strongly bound electron-hole pair –known as exciton– with a binding energy of around 0.5 eV. This is much larger than the thermal energy at room temperature (25 meV) which makes that excitons in organic solids cannot easily dissociate into free charge carriers. To dissociate the excitons in a homojunction they need to diffuse close to an electrode where they may produce free carriers and contribute to a photocurrent. As the diffusion length of excitons in organic solids is between 5 to 20 nm, only excitons close to the electrode can generate a photocurrent while most of the excitons generated in the bulk decay before reaching the electrode.[15-17]

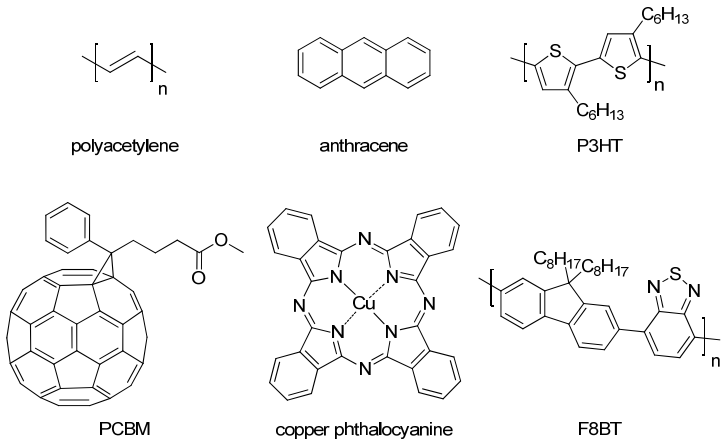

Figure 1.1: Molecular structures of some conjugated molecules and polymers.

The major breakthrough in OPV came in 1986 when C.W. Tang introduced the donor-acceptor heterojunction architecture by evaporating two different organic materials on top of each other.[1] At the interface between the two organic materials an energy offset is created because of the difference in the ionization potentials and electron affinities of both materials. When an exciton reaches the heterojunction, the interfacial energy offset drives the dissociation of the exciton into an electron and a hole. The material with the lowest oxidation potential, the donor, transfers an electron to the material with the highest electron affinity, the acceptor, as shown Figure 1.2. The process is a photoinduced charge transfer, the creation of charges by

illumination, similar to the primary step in photosynthesis. An important point to notice is that after photoinduced charge transfer the electron and hole are spatially separated in two different phases and can only meet again at the heterojunction. By introducing the heterojunction, Tang created an elegant way to dissociate a strongly bound electron-hole pair into a spatial separated electron and hole. The heterojunction concept is at the heart of all current efficient organic solar cell architectures, including hybrid architectures such as dye-sensitized solar cells.

Tang's bilayer solar cells had an efficiency of about 1%.[1] Bilayer heterojunctions, however, are often limited by the low exciton diffusion length in organic materials (5 to 20 nm) and the small surface area of the planar heterojunction. Only excitons generated within a distance of the exciton diffusion length from donor-acceptor interface may reach the interface and dissociate into free charge carriers. Photons absorbed further away from the donor-acceptor interface are lost. Both shortcomings of the bilayer solar cell were overcome by the introduction of the bulk heterojunction architecture.

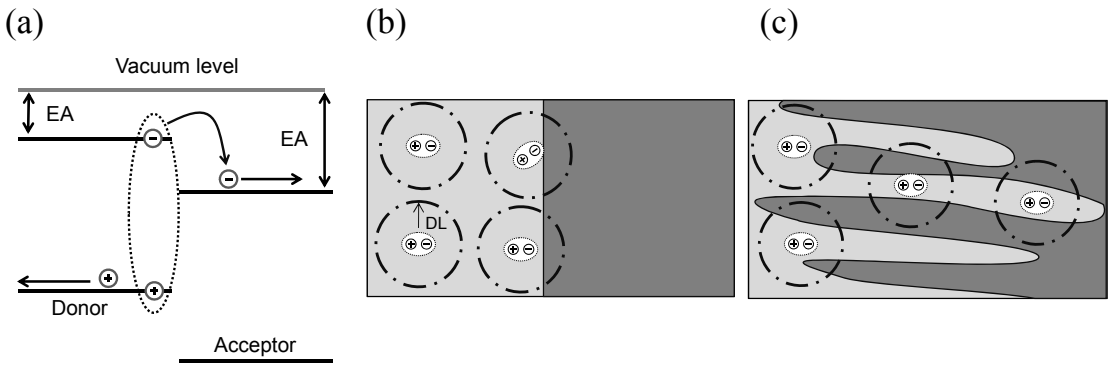

Figure 1.2: (a) Dissociation of an exciton at the donor-acceptor interface. (EA = electron affinity). Panels (b) and (c) represent bilayer and bulk heterojunction cell architecture, respectively. The diffusion range of an exciton is indicated by the dashed-dotted circle. *DL* is the diffusion length. In the bilayer, only the excitons close to the interface have a chance to be dissociated. For the bulk heterojunction the chance for exciton dissociation is very high because the interface is within a distance of the diffusion length.

In bulk heterojunction solar cells, the acceptor and the donor materials are blended together to form a bicontinuous interpenetrating network which extends over the complete active layer of the solar cell (Figure 1.2(c)). The surface area of donor-acceptor interface is dramatically increased in the bulk heterojunction compared to the bilayer configuration. This results in a high probability for the exciton to dissociate across the entire active layer when the domain size of the separated phases is in the order of the exciton diffusion length (*DL*). The first report of a working bulk

heterojunction solar cell appeared in 1991 by Hiramoto *et al*.[18] The active layer consisted of co-evaporated small acceptor and donor molecules as a blend.

In 1995, the first bulk heterojunction solar cells processed from solution were independently reported by Halls *et al.*[19] and Yu *et al.*[20] Still, power conversion efficiencies remained below 1%. A significant improvement of the power conversion efficiency to 2.5% was achieved Shaheen *et al.* by optimizing the acceptor-donor blend morphology with solvent processing.[21] In recent years, the efficiency of organic solar cell has increased dramatically by the availability of new, tailored materials. The new polymers and molecules have absorption spectra that better match the solar emission spectrum, have optimized energy levels, exhibit enhanced electronic transport, feature an optimized phase separation and domain size, and are incorporated in improved device structures. These developments were guided by the improved understanding of the fundamental physical processes in organic solar cells. Recently, He *et al.* accomplished a certified efficiency of 9.2% using an inverted device structure.[5] This improvement is close to the 12 % efficiency considered as feasible limit for organic solar single junction solar cells.[22-24] An impression of the progress made in recent years is given in Figure 1.3.

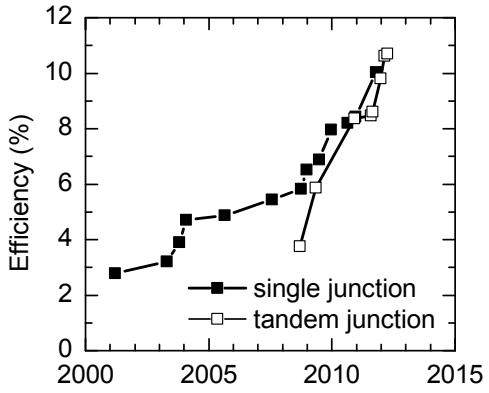

Figure 1.3: Increase of the power conversion efficiency of organic single junction and tandem junction solar cells in the last decade.

One way to further enhance the power conversion efficiency is by making tandem and multi-junction solar cells. In a tandem cell, two solar cells with different band gaps are stacked together by a recombination layer. Each subcell of the tandem cell is designed to absorb a different part of the solar emission spectrum. Generally, the front cell first absorbs the high energy photons with a high band gap material while the back cell absorbs a fraction of the remaining low energy photons with a small band gap material. By absorbing the high energy photons with a large band material and the low energy photons with a small band gap material, thermalization and

transmission losses are reduced, compared to a single junction solar cell. Hence, tandem solar cells convert the photons from solar the spectrum more efficiently than a single junction solar cell. For organic tandem solar cells an achievable efficiency of at least 15 % has been estimated.[25]

In 1990, Hiramoto *et al*.[26] prepared the first organic tandem cell by connecting two identical bilayer solar cells of evaporated small molecules via a thin gold layer acting as a recombination layer. A significant improvement of 5.7 % in organic tandem solar cell's efficiency was reached in 2004 by Xue *et al.* with a tandem cell consisting of hybrid planar mixed heterojunction where a blend of donor and acceptor molecules was co-evaporated and sandwiched between homogeneous donor and acceptor layers.[27] Silver nanocrystals were used to form a good recombination layer. In the same year, Drechsel *et al.* and Männig *et al.* introduced the p-i-n type heterojunction architecture in which the recombination contact consisted of doped, *i.e.* conducting, electron transport (ET) and hole transport (HT) layers that differ from the materials in the photoactive layer.[28,29] Dennler *et al.* made the first step towards polymer based tandem cells in 2006 by evaporating on top of a P3HT:PCBM solution processed solar cell a 1 nm thick gold recombination layer followed by an evaporated small molecule bilayer solar cell.[30] The first tandem cell consisting of two solution processed polymer:fullerene subcells was realized by Kawano *et al.* in 2006.[31] As recombination layer, Kawano used a sputtered indium tin oxide layer, covered by a spin coated PEDOT:PSS layer. The next step was to make tandem cells with a recombination layer processed from solution. This is an important technological requirement for R2R production of organic tandem solar cells. Gilot *et al.* fabricated one of the first tandem and triple junction solar cells with the subcells and the recombination layers processed completely from solution.[32] The recombination layers in these devices were fabricated by first spin casting a layer of ZnO nanoparticles on top of the active layer of the lower subcell and then spin casting a layer of transparent conducting polymer, poly(3,4-ethylenedioxythiophene) :poly(styrenesulfonate) (PEDOT:PSS), on top of the ZnO layer. ZnO acts as the electron collecting electrode of the lower subcell and PEDOT:PSS collects holes from the upper subcell, the collected electrons and holes recombine at the interface of ZnO and PEDOT:PSS. In the last years, the efficiencies of organic tandem cells improved significantly (Figure 1.3),[33,34] and recently Heliatek reported a 10.7 % efficiency for an organic tandem cell of evaporated small molecules.[35,36]

Though, organic single junction and especially organic tandem solar cells reach commercially viable efficiencies, many technological and scientific challenges have to be overcome. One of the main technological challenge is to reproduce on a large scale with R2R processes the high efficiencies obtained on a lab scale. Another

challenge is to increase the stability of organic solar cells to reach lifetimes in the order of 20 years or more. Also, the power conversion efficiencies of organic solar cells need to be further increased. To further increase the efficiencies, a complete understanding of the fundamental physical processes in organic solar cell is needed. Furthermore, accurate experimental characterization techniques are needed to study these fundamental processes and to characterize correctly the performance of organic solar cells.

1.3 Working principle of bulk heterojunction organic solar cells

In this section the basic processes involved in the generation of electricity upon illumination of an organic solar cell will be discussed. Each process is crucial for the device performance and needs to be optimized in order to maximize the solar cell's power conversion efficiency.

The device architecture of a typical bulk heterojunction organic solar cell is illustrated in Figure 1.4(a). Indium tin oxide (ITO) with a thickness of ~120 nm, patterned on glass, serves as transparent electrode. On top of the ITO electrode a ~50 nm layer of PEDOT:PSS is deposited which reduces the ITO's surface roughness and has higher work function than ITO, creating a better hole collecting contact with the donor material. The photoactive layer made of an acceptor-donor blend is sandwiched between the PEDOT:PSS layer and a low work function electron collecting electrode consisting of lithium fluoride (1 nm) and aluminum (~100 nm). The thickness of the photoactive layer is usually optimized for optimal performance and varies roughly in the range from 50 to 300 nm, depending on the actual nature of the organic semiconductor.

To produce electricity from sunlight with a photovoltaic device three steps need to occur: (*i*) absorption of light, (*ii*) generation of free charge carriers, and (*iii*) transport and collection of the free carriers at the electrodes. The exact mechanism of absorption, charge generation, charge transport and collection varies for different types of solar cells. Each of these steps can further be divided in different processes. The processes involved in the generation of electric current upon illumination in an organic bulk heterojunction solar cell are illustrated in Figure 1.4(a) from a spatial and from an energetic perspective in Figure 1.4(b), which shows the cell at short circuit conditions (V = 0 V). At short circuit, the energies of the ITO/PEDOT:PSS and the Li/Al electrodes align and, in consequence, the energy levels of the highest occupied molecular orbital (HOMO) and lowest unoccupied molecular orbital (LUMO) of donor and acceptor are tilted over the thickness of the active layer by the internal built-in electric field caused by the difference of the work functions of the

two electrodes. First, a photon is absorbed, *e.g.* in the donor material, and an exciton is formed (step (1)).

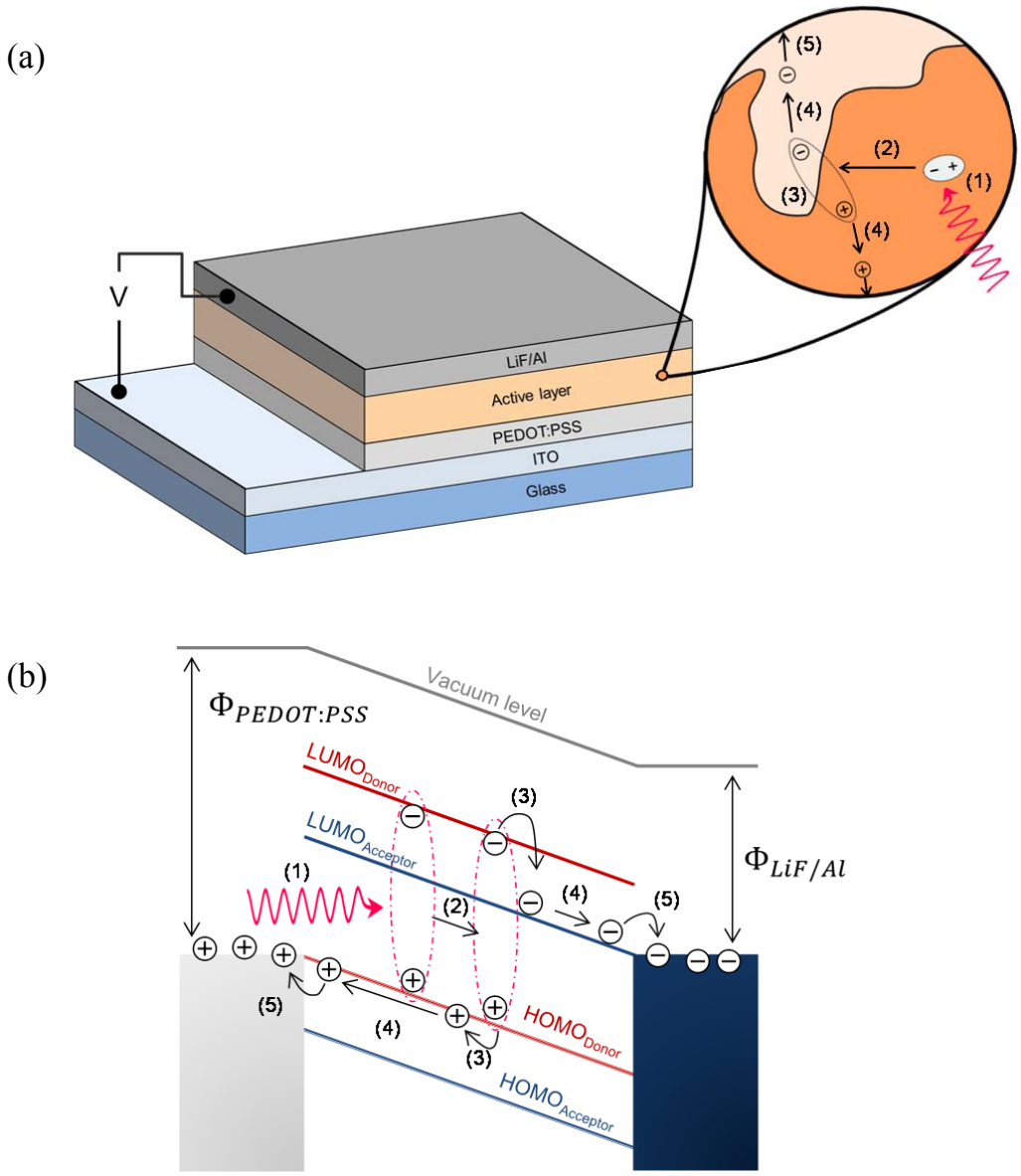

Figure 1.4: (a) Device architecture of an organic solar cell including a close up zoom at the nanoscale level of the acceptor-donor blend. (b) Energy diagram of a bulk heterojunction solar cell at short-circuit. The operation involves five steps: (1) Generation of an exciton by absorption of a photon. (2) Exciton diffusion to the acceptor-donor interface. (3) Dissociation into an interfacial electron-hole pair. (4) Separation of the electron and hole from the interface and subsequent transport. (5) Collection of the charges at the electrodes.

Within its lifetime the exciton has to reach the donor-acceptor interface by diffusion (step (2)) where it can be dissociated by charge transfer into an interfacial electron-hole pair also called charge transfer (CT) state (step (3)). After photoinduced

charge transfer, the electron is located in the acceptor phase in the LUMO energy level of the acceptor, while the hole is located in the donor phase in the HOMO energy level. The weakly bound electron hole pair in the CT state must then be spatially separated (step (4)), possibly assisted by the electric field present in the device that arises from the work function differences of the two electrodes (Figure 1.4(b)), and be transported to the electrodes. Finally, the electron and hole must be collected at the respective electrodes (Li/Al and ITO/PEDOT:PSS) (step (5)), to contribute to the photocurrent and photovoltage. Unfortunately, each of the five steps depicted in Figure 1.4 are prone to losses and are influenced by the acceptor and donor material properties and by the composition and morphology of acceptor-donor blend. The challenge for the field of organic solar cells is to identify and elucidate these loss mechanisms and find ways, either by developing new materials or by advanced cell architectures to militate against them.

1.4 Characterization of organic solar cells

1.4.1 Current density - voltage characteristics

To characterize the performance of an organic solar cell the current density-voltage ($J-V$) characteristics are measured in the dark (J_D) and under (simulated) solar illumination (J_L). A typical $J-V$ measured in dark and under illumination is shown in Figure 1.5(a). Because OPV cells are rectifying, the dark $J-V$ is similar to the $J-V$ curve of a diode. Below a positive threshold voltage and in reverse bias no dark current flows through the solar cell and above current starts to flow (see dashed curve). The illumination current density (J_L) results from the sum of the photocurrent density (J_{PH}), which is generated under illumination, and the dark current density (J_D).

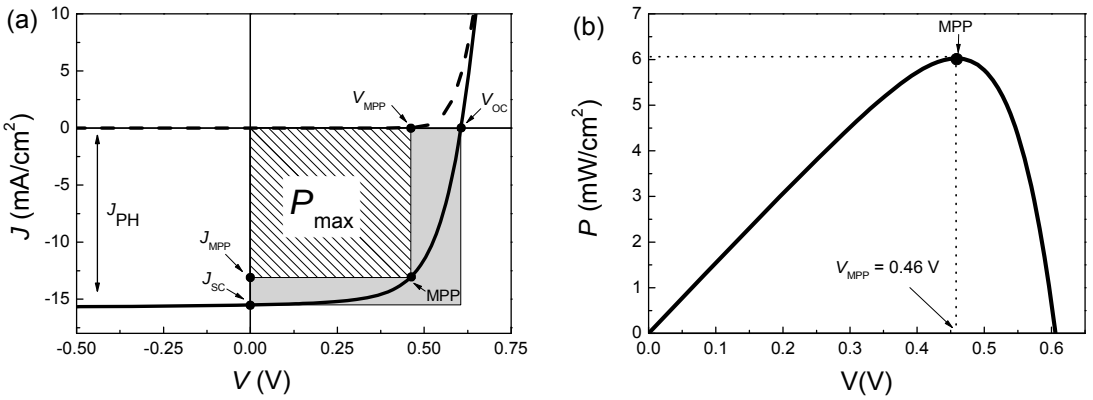

Figure 1.5: (a) Typical $J-V$ characteristics in dark (dashed line) and under illumination (solid line) of an organic solar cell. (b) Power density as a function of applied voltage.

The dark $J-V$ curve gives useful information about the electrical quality of an organic solar cell. Any noticeable current in reverse bias indicates leakage current across the solar cell which may be caused by imperfections in the active layer. Furthermore, the magnitude of the dark current in forward bias above the threshold voltage gives a first indication about the conductivity of the active layer and the quality of the contacts between the electrodes and active layer. A low dark current in forward bias may indicate either a poor charge carrier transport across the active layer or an (semi-)insulating contact between the active layer and the electrodes.

The performance of the organic solar cell can be determined from the $J-V$ curve under illumination. The relevant quantities determined from the $J-V$ curve under illumination are the short circuit current density (J_{SC}), the open circuit voltage (V_{OC}), the maximum power (P_{max}), and the fill factor (FF). The short circuit current density is the current delivered by the solar cell at 0 V. At open circuit voltage, the illumination current is zero and, hence, the dark current is canceled by the illumination current. The power density of a solar cell is given by the product of the illumination current density and voltage:

$$P = -J_L V \tag{1.1}$$

The negative sign in Equation (1.1) sets the power density according the sign convention. According this convention, for positive power densities the solar cell delivers power to an external load. Figure 1.5(b) shows the power density as a function of applied voltage of the solar cell in the fourth quadrant. Between 0 V and V_{OC} the power density is positive and the solar cell delivers net power to a load. The maximum power (P_{max}) a solar cell can deliver is located at the maximum of the power density voltage curve (Figure 1.5(b)). The (J,V) coordinates at which the output power maximizes are referred to as the maximum power point (MPP) which is designated as (J_{MPP},V_{MPP}). The maximum power conversion efficiency (η) of a solar cell is given by:

$$\eta = \frac{P_{max}}{I_L} = \frac{J_{MPP} V_{MPP}}{I_L} \tag{1.2}$$

where I_L is the intensity (in W/m^2) of the light. The maximum extractable power $P_{max} = J_{MPP} \times V_{MPP}$ corresponds to hatched area in Figure 1.4(a) and can be compared to the product $J_{SC} \times V_{OC}$, represented by the grey rectangle and their ratio

defines the fill factor:

$$FF = \frac{J_{MPP} V_{MPP}}{J_{SC} V_{OC}} \tag{1.3}$$

The *FF* indicates the quality of *J*−*V* curve under illumination. In the ideal case when the *FF* is close to unity, the *J*−*V* curve would be squared and V_{MPP} would be located closely to V_{OC}. However, in reality the *FF* is reduced by various loss mechanisms, affecting the extraction of photogenerated carriers. Combining Equations (1.2) and (1.3), the power conversion efficiency can be defined as follows:

$$\eta = \frac{J_{SC} V_{OC} FF}{I_L} \tag{1.4}$$

The latter equation shows clearly that the J_{SC}, V_{OC} and the *FF* have to be maximized in order to increase the power conversion efficiency.

1.4.2 Spectral response and external quantum efficiencies measurements

The monochromatic spectral response (*S*) relates the short-circuit photocurrent density (*J*) of a solar cell to a monochromatic illumination with intensity *I*:

$$S(\lambda) = \frac{J(\lambda)}{I(\lambda)} \tag{1.5}$$

where λ is the wavelength of the light. The spectral response (in A/W) can be used to calculate the short circuit current expected under standard test conditions. Standard test conditions (STC) have been established to compare the performance (efficiencies) of photovoltaic cells. Under STC the solar cell is illuminated with the AM 1.5 G (AM: air mass) global reference spectrum at an intensity (irradiance) of I = 1000 W/m^2. The short circuit current at AM 1.5 G illumination condition can be obtained by integrating the spectral response of the test solar ($S_T(\lambda)$) cell over the spectral irradiance of the AM 1.5 G reference spectrum ($E_R(\lambda)$):

$$J_{SC} = \int S_T(\lambda, E_R) E_R(\lambda) d\lambda \tag{1.6}$$

Because organic solar cells may present intensity dependent losses at 1 sun intensity, the solar cell is biased with additional light at one sun intensity during the spectral response measurement.[37] Another interesting quantity that is related to the

spectral response is the external quantum efficiency (*EQE*). The *EQE* is the ratio between the number of extracted electrons to the number of photons incident on the solar cell and is related to spectral response by:

$$EQE(\lambda) = S(\lambda)\frac{hc}{q\lambda} \tag{1.7}$$

where q is the elementary charge, h the Planck constant, and c the speed of light. The *EQE* is directly related to the efficiencies of the different steps (Section 1.3) involved in the generation of a photocurrent upon illumination at a given wavelength. When the fraction of absorbed photons ($A(\lambda)$) of the active layer is determined either experimentally or by optical modeling the internal quantum efficiency, $IQE(\lambda)$, can be calculated by dividing the $EQE(\lambda)$ by this fraction. The *IQE* itself can be formally expressed as:

$$IQE = \eta_{\mathrm{D}} \cdot \eta_{\mathrm{CT}} \cdot \eta_{\mathrm{CS}} \cdot \eta_{\mathrm{T}} \cdot \eta_{\mathrm{C}} \tag{1.8}$$

where η_D is the probability that a generated exciton reaches the acceptor-donor interface, η_{CT} the probability that it will form a CT state, η_{CS} the probability that the electron and hole of the CT state are separated from the interface, η_{T} is probability that the free carriers are transported to the correct electrodes without recombining, and η_C the probability that the free carriers are collected at the electrodes. Equation (1.8) shows that the *IQE* can give insight into the quantum efficiency of the various steps that occur in converting light into electricity in an organic solar cell. In Equation (1.8) we have dropped the wavelength dependence of the various η parameters. It is however likely that η_{D}, η_{CT}, and η_{CS} depend, to some extent, on the photon energy used.

Chapters 5 and 6 of this thesis address a new technique to accurately measure the *EQE* for organic solar cells as function of the intensity and the wavelength of the bias light that effects $A(\lambda)$ and $IQE(\lambda)$ by a variety of processes.

1.4.3 Numerical simulation of *J*−*V* curves

To analyze dark, illumination, and photocurrent voltage curves, drift-diffusion modeling of the *J*−*V* curves can be used as a tool. By numerical drift-diffusion simulation a better understanding of the relevant physical processes occurring in bulk heterojunction solar cells can be gained. In this thesis, the drift-diffusion program developed by Koster *et al*. is used. A detailed description of the program and

numerical method can be found in Ref [38]. The basic equations used in the simulation code describing charge carrier transport are discussed in this section.

The numerical program of Koster considers drift and diffusion of free carriers in one dimension across the active layer, bimolecular recombination between electron and holes, and the effect of space charge on the electric field across the active layer. The effective medium approach is applied to the active layer, the acceptor and donor blend is considered as one intrinsic semiconductor. The band gap (E_g) of the "fictive" intrinsic semiconductor is chosen as the energy difference between the donor HOMO and the acceptor level LUMO energy levels. Electron and hole mobilities determined on acceptor-donor blends can be used as mobility (μ) of the intrinsic semiconductor. The contact between the electrodes and the active layer is generally considered as an Ohmic contact.

The total current density (J_{TOT}) across the solar cell as a function of voltage is the sum of the electron (J_n) and current hole (J_p) current densities at any point x in the active layer:

$$J_{TOT}(V) = J_n(x,V) + J_p(x,V) \tag{1.9}$$

The local current density of electrons and holes in the active layer is the sum of the drift and diffusion currents:

$$J_n(x) = qn(x)\mu_n F(x) + qD_n \nabla n(x) \tag{1.10a}$$
$$J_p(x) = qp(x)\mu_p F(x) - qD_p \nabla p(x) \tag{1.10b}$$

where $n(x)$ and $p(x)$ are the electron and hole densities, D_n and D_p the diffusion coefficient for electron and holes, and μ_n and μ_p their charge carrier mobilities. In Equation (1.10) the drift current (1st term on the right hand side) scales with carrier density mobility and the electric field, while the diffusion current (2nd term on the right hand side) scales with the gradient of carrier density and the diffusion coefficient. The diffusion coefficient is related to the mobility *via* the Einstein relation:

$$D_{n,p} = \mu_{n,p} \frac{kT}{q} \tag{1.11}$$

where k is the Boltzmann coefficient and T is the temperature.

The Poisson equation relates the electron and carrier density to the electric field and to the potential (ψ):

$$-\nabla F(x) = \nabla^2 \psi(x) = \frac{q}{\varepsilon}[n(x) - p(x)] \tag{1.12}$$

where the difference $n(x) - p(x)$ is the net space charge and ε the dielectric constant.

The continuity equation relates the electron (hole) current density to the generation rate, $G(x)$, of carriers under illumination and to their recombination rate, $R(x)$:

$$\nabla J_n(x) = -q[G(x) - R(x)] \tag{1.13a}$$

$$\nabla J_p(x) = q[G(x) - R(x)] \tag{1.13b}$$

A bimolecular recombination rate between electrons and holes is considered by a Langevin recombination rate equation:[39]

$$R(x) = \frac{q(\mu_n + \mu_p)}{\varepsilon}[n(x)p(x) - n_i^2] \tag{1.14}$$

where n_i is the intrinsic carrier density of electrons and holes due to thermal excitations.

To numerically simulate a $J-V$ curve, the Poisson equation and continuity equation are solved iteratively. The electron and hole current densities relate the currents of the continuity equations to the carrier densities of the Poisson equation. In order to find a unique solution to the set of Equations (1.10)−(1.14), boundary conditions are set by the carriers densities and the potentials at the contacts.

Ohmic contacts are considered by the Boltzmann statistics. At the bottom contact ($x = 0$) which is defined as the electron Ohmic contact the boundary condition on the carrier density is:

$$n(0) = N_{CV} \tag{1.15a}$$

$$p(0) = N_{CV} \exp\left(-\frac{E_g}{kT}\right) \tag{1.15b}$$

with N_{CV} the effective density of states of the valence (donor HOMO) and conduction (acceptor LUMO) bands. At the top contact ($x = L$) which is defined as the hole

Ohmic contact the boundary condition on the carrier density is:

$$n(L) = N_{CV} \exp\left(-\frac{E_g}{kT}\right) \quad (1.16a)$$

$$p(L) = N_{CV} \quad (1.16b)$$

The boundary condition on the potential difference of the contact at an applied voltage V is given by:

$$\psi(L) - \psi(0) = \frac{E_g}{q} - V \quad (1.17)$$

The drift-diffusion model of charge transport as developed by Koster *et al*.[38] allows to model the $J-V$ characteristics of organic solar cells and will be used extensively in Chapters 3 and 4 to elucidate the photocurrent of these cells in reverse and forward voltage bias.

1.5 Loss mechanisms in organic solar cells

The power conversion efficiency of an organic solar is reduced by different loss mechanisms. The most fundamental loss mechanisms are thermalization and transmission losses which ultimately limit the efficiency of a single junction solar cell. Thermalization losses, illustrated in Figure 1.6 (a), occur when photons with higher energy than the energy band gap of the organic material are absorbed and produce hot excitons. The hot excitons quickly relax to the band edge of the absorber by releasing the excess energy as heat. By thermalization, the available energy of the photon is reduced to the energy of the band gap. Transmission losses, illustrated in Figure 1.6 (b), occur when the photon energy is smaller than the energy band gap. In this case, the photons cannot be absorbed and cannot generate a current. Thermalization losses limit the open circuit voltage while transmission losses limit the short circuit current of the solar cell.

The spectral irradiance at AM 1.5 G solar illumination is shown in Figure 1.6(c) and compared to the corresponding spectral power density of a solar cell with a band gap of 1.9 eV. By reducing the band gap, the J_{SC} will increase and the V_{OC} will decrease. Increasing the energy band gap, the opposite will be observed, V_{OC} increases and J_{SC} decreases. In bulk heterojunction solar cell an additional loss in V_{OC} occurs due to the energy offset between the lowest singlet energy of donor and acceptor and the energy of the CT state at the interface.

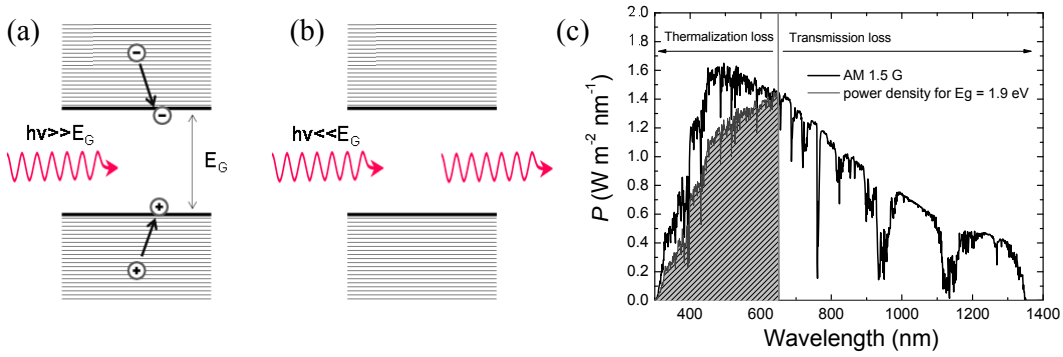

Figure 1.6: (a) Thermalization loss of a photon with a higher energy than the semiconductor band gap. (b) Transmission loss of a photon with a lower energy than the semiconductor band gap. (c) The AM 1.5 G solar spectrum compared to the power density harvested by a material with a band gap of 1.9 eV (or sharp absorption onset at 650 nm).

Equation (1.4) shows that the power conversion efficiency scales with J_{SC}, V_{OC}, and *FF*. The *FF* is dependent on electric field dependent losses. When the voltage is increased from reverse bias to V_{OC} the electric field across the active layer decreases and losses will be more pronounced. Geminate recombination of interfacial CT states is one loss process that is electric field dependent. In many efficient bulk heterojunction solar cells, a small electric field is sufficient to separate the CT states into free carriers. In such materials, geminate recombination may occur close to V_{OC} where the electric field across the active layer is small. Geminate recombination *vs.* CT state dissociation is extensively discussed in Ref. [40].

A relevant loss of photogenerated charge carriers at low electric fields is due to the competition between diffusion and drift of photogenerated carriers. Figure 1.7(a) and (b) show the energy diagram of an organic solar cell at a potential close to V_{OC}. Because the electric field is small, diffusion of photogenerated charges will occur in a direction that is primarily determined by their generation gradient in the device and will be subsequently collected at both electrodes, Figure 1.7(a), or will recombine bimolecularly, Figure 1.7(b). Electrons collected at the hole collecting contact (under operating condition $V < V_{OC}$) and holes collected at the electron collecting contact can be considered as a contact loss. Only few carriers are collected by drift and these generate a small net photocurrent. When the electric field is increased, more and more carriers are extracted by drift at the correct electrodes and the net photocurrent increases. The effect of the competition between drift and diffusion with increasing field (effective voltage, V_{EFF}) on the photocurrent is shown in Figure 1.7(c). As the effective voltage increases, the photocurrent converges to the saturation photocurrent which is limited by the generation rate (G) in the device.

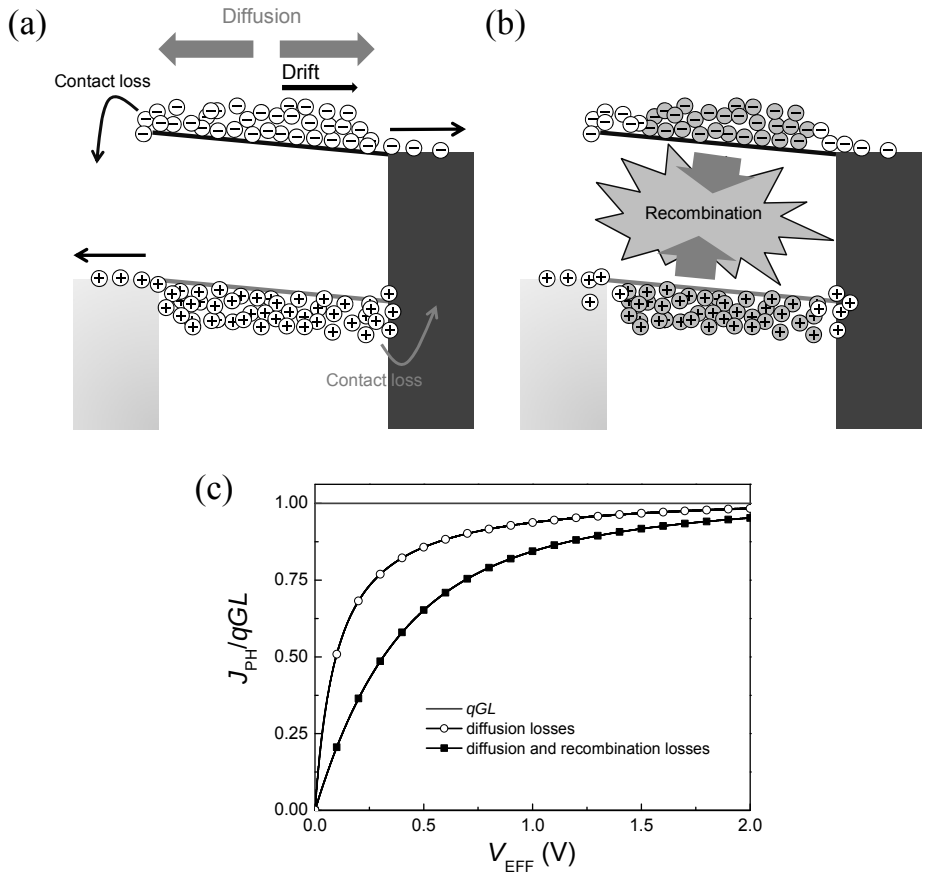

Figure 1.7: (a) Illustration of contact losses due to diffusion close to open circuit voltage. (b) Illustration of bimolecular recombination losses close to open circuit voltage. (c) Photocurrent as normalized to the saturation current (qGL) as a function of effective applied voltage V_{EFF} ($V_{EFF} = |V_{OC} - V|$). Photocurrents calculated with the model described in Section 1.4.3 considering diffusion losses with and without bimolecular recombination.

Another loss mechanism that occurs in organic solar cells is bimolecular recombination, which can be described by Equation (1.14). When the electric field is small, *e.g.* close to $V_{OC,}$ photogenerated carriers accumulate in the device because the charge extraction time is large. Hence, electron and hole densities increase and probability that electrons and holes meet and recombine bimolecularly thereby increases (Figure 1.7(b)). This is also reflected in Equation (1.14) by the product of electron and hole densities. When the electric field in the device is increased by increasing the effective voltage, the extraction time of carriers is reduced and thereby the carrier density and bimolecular recombination become smaller. This is also observed in the photocurrent curve in Figure 1.7(c). At low effective voltages the photocurrent that includes bimolecular recombination is smaller than the photocurrent when only diffusive contact losses are considered but with increasing effective voltage recombination losses decrease and the photocurrent converges to the saturation photocurrent.

1.6 Outline and aim of this thesis

The focus of the work presented in this thesis is on gaining a better understanding of various physical processes that affect the efficiency of organic solar cells. Also a strong aim of this thesis is exploring new experimental techniques and improving existing experimental techniques to characterize organic solar cells and study physical processes occurring in organic solar cells. Though the efficiencies of organic solar cells are reaching commercially competitive values, a detailed and more complete understanding of all the physical processes is needed to further increase the power conversion efficiencies by rational design. In addition, these physical processes have to be probed correctly by experimental techniques that accurately account for possible artifacts that otherwise may result in wrong interpretation. The balance between exploring new, improved measurement techniques and establishing the effects of processes such as carrier injection, recombination, and intensity and wavelength dependence of loss processes is a recurring theme. In several examples we use electrical and optical modeling to support the conclusions.

In Chapter 2, electroabsorption spectroscopy is explored as a non-invasive optical experimental technique to probe electric fields in organic tandem and in organic single junction solar cells. As shown in previous sections the electric field across the active layer is crucial for efficient charge transport and collection. Moreover, it is not fully understood how the recombination layer in an organic tandem solar cell distributes the electric fields over the individual sub cells.

In Chapter 3, photocurrents in organic solar cells are studied experimentally and theoretically with drift-diffusion modeling. First the technique on how to measure photocurrents correctly in reverse, but especially in forward bias is addressed. The effect of increased recombination rate and different injecting properties of the contacts on the photocurrent is studied.

In Chapter 4, photocurrent multiplication, *i*.e. a photocurrent that exceeds the number of photons absorbed per unit time, is observed experimentally and in simulations. The simulations show that photocurrent multiplication is the result of the space charge in the device under illumination and can occur when bimolecular recombination rates are very low and when electron and hole mobilities differ.

In Chapter 5, we demonstrate experimentally and analytically that the current method used by the organic solar cell community to measure spectral responsivity of a solar cell with bias illumination is not correct when the solar cell presents non-linear light intensity dependent losses. A new method is proposed that determines accurately the spectral response under bias illumination. With the new method a much more accurate estimate of the power conversion efficiency can be obtained under bias illumination.

Chapter 6 explores the influence of monochromatic light on the current-voltage characteristics. Monochromatic light is more easier to use than white light in determining the efficiency of organic tandem cells but hitherto it is not clear under which conditions this can be done. The effect of the beam intensity profile and the optical electrical field will be addressed experimentally and supported by device modeling.

1.7 References

[1] C. W. Tang, *Appl. Phys. Lett.* **1986,** *48*, 183.

[2] C. W. Tang, U.S. Patent 4,164,431, August 14, **1979**.

[3] D. H. Meadows, D. L. Meadows, J. Randers, W.W. Behrens III*, The Limits to Growth, a report of the Club of Rome's Project on the Predicament of Mankind,* Universe Books, New York, **1972**.

[4] The OPEC oil embargo lasted from October 1973 to March 1974.

[5] Z. He, C. Zhong, S. Su, M. Xu, H. Wu, Y. Cao, *Nat. Photon.* **2012**, *6*, 593.

[6] M. A. Green, K. Emery, Y. Hishikawa, W. Warta, E. D. Dunlop, *Prog. Photovolt: Res. Appl.* **2012**, *20*, 12.

[7] C. H. Peters, I. T. Sachs-Quintana, J. P. Kastrop, S. Beaupre, M. Leclerc, M. D. McGehee, *Adv. Energy Mater.* **2011**, *1*, 491.

[8] F. C. Krebs, *Sol. Energy Mater. Sol. Cells.* **2009**, *93*, 394.

[9] N. Espinosa, M. Hosel, D. Angmo, F. C. Krebs, *Energy Environ. Sci.* **2102**, *5*, 5117.

[10] http://one.laptop.org/

[11] F. C. Krebs, T. D. Nielsen, J. Fyenbo, M. Wadstrøm, M. S. Pedersen, *Energy Environ. Sci*. **2010**, *3*, 512.

[12] H. Kallmann, M. Pope, *J. Chem. Phys.* **1959**, *30*, 585.

[13] G. A. Chamberlain, *Sol. Cells* **1983**, *8*, 47.

[14] A. K. Ghosh, T. Feng, *J. Appl. Phys.* **1978**, *49*, 5982.

[15] A. Haugeneder, M. Neges, C. Kallinger, W. Spirkl, U. Lemmer, J. Feldmann, U. Scherf, E. Harth, A. Gügel, K. Müllen, *Phys. Rev. B.* **1999**, *59*, 15346.

[16] M. Theander, A. Yartsev, D. Zigmantas, V. Sundstrom, W. Mammo, M. R. Andersson, O. Inganäs, *Phys. Rev. B.* **2000**, *61*, 12957.

[17] D. E. Markov, E. Amsterdam, P. W. M. Blom, A. B. Sieval, J. C. Hummelen, *J. Phys. Chem. A* **2005**, *109*, 5266.

[18] M. Hiramoto, H. Fujiwara, M. Yokoyama, *Appl. Phys. Lett.* **1991**, *58*, 1062.

[19] J. J. M. Halls, C. A. Walsh, N. C. Greenham, E. A. Marseglia, R. H. Friend, S. C. Moratti, A. B. Holmes, *Nature* **1995**, *376*, 498.

[20] G. Yu, J. Gao, J. C. Hummelen, F. Wudl, A. J. Heeger, *Science* **1995**, *270*, 1789.

[21] S. E. Shaheen, C. J. Brabec, N. S. Sariciftci, F. Padinger, T. Fromherz, J. C. Hummelen, *Appl. Phys. Lett.* **2001**, *78*, 841.

[22] M. C. Scharber, D. Mühlbacher, M. Koppe, P. Denk, C. Waldauf, A. J. Heeger, C. L. Brabec, *Adv. Mater.* **2006**, *18*, 789.

[23] L. J. A. Koster, V. D. Mihailetchi, P. W. M. Blom, *Appl. Phys. Lett.* **2006**, *88*, 093511.

[24] D. Veldman, S. C. J. Meskers, R. A. J. Janssen, *Adv. Funct. Mater*. **2009**, *19*, 1939.

[25] G. Dennler, M. C. Scharber, T. Ameri, P. Denk, K. Forberich, C. Waldauf, C. J. Brabec, *Adv. Mater.* **2008**, *20*, 579.

[26] M. Hiramoto, M. Suezaki, M. Yokoyama, *Chem. Lett.* **1990**, 327.

[27] J. G. Xue, S. Uchida, B. P. Rand, S. R. Forrest, *Appl. Phys. Lett.* **2004**, *85*, 5757.

[28] J. Drechsel, B. Männig, F. Kozlowski, D. Gebeyehu, A. Werner, M. Koch, K. Leo, M. Pfeiffer, *Thin Solid Films* **2004**, *451-452*, 515.

[29] B. Männig, J. Drechsel, D. Gebeyehu, P. Simon, F. Kozlowski, A. Werner, F. Li, S. Grundmann, S. Sonntag, M. Koch, K. Leo, M. Pfeiffer, H. Hoppe, D. Meissner, N, S. Sariciftci, I. Riedel, V. Dyakonov, J. Parisi, *Appl. Phys. A*. **2004**, *79*, 1.
[30] G. Dennler, H. J. Prall, R. Koeppe, M. Egginger, R. Autengruber, N. S. Sariciftci, *Appl. Phys. Lett.* **2006**, *89*, 073502.
[31] K. Kawano, N. Ito, T. Nishimori, J. Sakai, *Appl. Phys. Lett.* **2006**, *88*, 073514.
[32] J. Gilot, M. M. Wienk, R. A. J. Janssen, *Appl. Phys. Lett.* **2007**, *90*, 143512.
[33] V. S. Gevaerts, A. Furlan, M. M. Wienk, M. Turbiez, R. A. J. Janssen, *Adv. Mater.* **2012**, *24*, 2130.
[34] L. Dou, J. You, J. Yang, C.-C. Chen, Y. He, S. Murase, T. Moriarty, K. Emery, G. Li, Y. Yang, *Nat. Photon.* **2012**, *6*, 180.
[35] Heliatek, http://www.heliatek.com/
[36] NREL, **2012**, http://www.nrel.gov/ncpv/images/efficiency_chart.jpg
[37] J. M. Kroon, M. M. Wienk, W. J. H. Verhees, J. C. Hummelen, *Thin Solid Films* **2002**, *403*, 223.
[38] L. J. A. Koster, E. C. P. Smits, V. D. Mihailetchi, P. W. M. Blom, *Phys. Rev. B*. **2005**, *72*, 085205.
[39] P. Langevin, *Ann. Chim. Phys. VII* **1903**, *28*, 433.
[40] T. M. Clarke, J. R. Durrant, *Chem. Rev.* **2010**, *110*, 6736.

2 Probing electric fields in polymer tandem and single junction cells with electroabsorption spectroscopy

Abstract

For polymer tandem solar cells it is not easy to determine the individual internal electric fields across each of the two individual photoactive layers, because the intermediate contact is often buried in the device stack and cannot be contacted. In this chapter we explore electroabsorption (EA) spectroscopy as a possible tool to investigate these electric fields in polymer tandem solar cells. EA spectroscopy is a non-invasive electro-optical technique that can be used to probe internal electrical fields in organic thin film devices. The tandem cell investigated consists of a wide band gap front cell and a small band gap back cell, connected *via* an intermediate recombination contact. We demonstrate that the EA spectra of the individual subcells and their dependence on applied external bias can be distinguished in the EA spectrum of the tandem cells, but that a quantitative interpretation of the EA spectra in terms of individual internal fields is hampered by a non-linear bias dependence of the EA intensity on the applied external bias, especially for the small band gap cell. By studying the corresponding single junction wide and small band gap cells, we establish that the non-linear bias dependence finds its origin in a spectral shift of the EA signal due to a change in the ratio of two different components contributing to the EA spectrum. The two components have been identified as being due to the Stark effect and to charges induced into the active layer in the EA experiment.

2.1 Introduction

To date the most efficient single junction organic solar cells reach 9.2% power conversion efficiency.[1−3] This is close to the 12% which is presently considered as a practical value for the maximum efficiency of single layer bulk-heterojunction organic solar cells,[4−6] although it is not considered a fundamental limit.[7−10] In a single junction organic solar cell the efficiency is limited by two fundamental loss mechanisms. The first loss mechanism is thermalization of excitations and occurs when photons with higher energy than the energy band gap of the polymer or organic semiconductor are absorbed. The hot excitons relax to the band edge. This corresponds to a loss of the available electrochemical potential of the photons and reduces their energy to that of the optical band gap. The second loss mechanism is the transmission of photons which cannot be absorbed by the polymer because their energy is lower than the optical band gap of the polymer. The maximum power conversion efficiency is a tradeoff between maximizing the number of absorbed photons and maximizing the potential energy.

The power conversion efficiency can be further enhanced by using the tandem or multiple junction architectures. For organic tandem cells it is estimated that the efficiency can be increased to at least 15%.[11] In a tandem cell, transmission and thermalization losses are reduced by absorbing the high energy photons and the low energy photons of the solar spectrum in separate layers with wide and small optical band gaps. In the most common series-connected configuration, the high-energy photons are first absorbed by the wide band gap front cell that transmits the low-energy photons to the small band gap back cell where they can be absorbed. Compared to a single junction cell, thermalization losses are reduced in the tandem cell since high energy photons are absorbed in a material with a wider optical band gap and the transmission losses are reduced by extending the absorption range with the small optical band gap sub cell.

In most tandem solar cells, the two subcells are connected in series by a transparent intermediate recombination layer. The recombination layer is crucial for the correct functioning of the tandem cell. The recombination layer has to ensure that the generated electrons in the front cell and holes in the back cells are collected by Ohmic contacts, not to lose energy, and recombine efficiently. In organic solar cells this can be achieved by making a dual contact layer consisting of a stack of doped n-type and p-type transparent semiconductors. For polymer solar cells that are fabricated by solution based deposition techniques, also the recombination layer is preferably deposited from solution to enable in the future a cheap roll-to-roll processing of polymer tandem cells. In recent years several fully-solution processed

polymer tandem cells have been reported both with conventional and inverted polarity configurations.[12–21]

In organic solar cells charge carrier generation, transport, and collection are strongly affected by the electric field across the active layer. In a tandem configuration both cells have to work in concert, and consequently, the electric field across the active layer of each subcell is important for efficient device operation. In studying the operation of organic solar cells it is useful to have information on the electric field that is inside the active layers. In a single junction solar cell the net-electric field is determined by voltage and thickness, but for a tandem cell one does not *a priori* know how the total voltage is distributed over the two layers, although it is possible to use a configuration with a proximate middle contact to probe the intermediate potential.[22] The recombination layer of the tandem imposes a boundary condition which makes that the photocurrent across the tandem cell cannot exceed the current of the subcell with the lowest photocurrent. This implies that in the non-current limiting subcell the potential drop will be adjusted to deliver the same current as the current limiting subcell. The effect of the recombination layer on the electric field distribution in the organic tandem cell is not yet fully understood, yet crucial for efficient device operation.

Electroabsorption (EA) spectroscopy is an elegant technique to probe optically and non-invasively electric fields in thin film devices. EA has frequently been applied to organic light-emitting devices (OLEDs) to determine the built-in voltage which results from difference in work function between the two electrodes.[23–35] EA spectroscopy has also been applied to determine the internal electric field in organic solar cells.[36–39]

Electroabsorption spectroscopy exploits the Stark effect which is the shifting or splitting of spectral lines by a static electric field.[40] When a static electric field is applied on a molecule its energy levels shift due to the perturbation caused by the electric field on the electronic wave function. The shift of the energy levels causes a shift of the absorption spectrum. The change of the absorption coefficient ($\Delta\alpha$) caused by the applied electric field is measured in EA. For excitation of randomly oriented molecules with neutral excited states with a small transition dipole, the EA signal resembles the first derivative of the absorption band.[41] When there is a large transition dipole moment, like a strongly polar CT transition, the EA spectrum will resemble the second derivative of the absorption band.[41]

The aim of the research described in this chapter is to investigate the use of EA spectroscopy to determine the internal electric field in tandem polymer solar cells. The polymer tandem solar cells studied in this chapter are based on the fully solution processed cells developed by Gilot *et al.*[15]

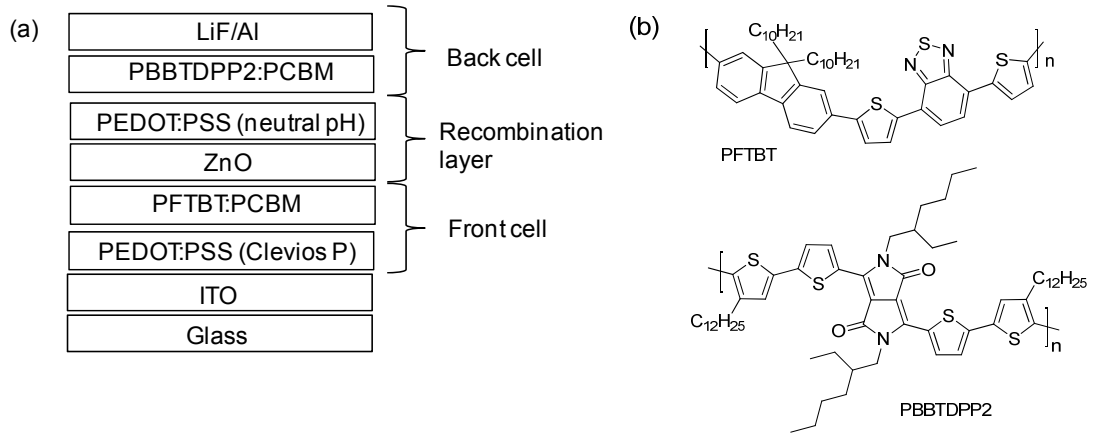

Figure 2.1: (a) Layer stack of the tandem solar cell. (b) Molecular structure of PFTBT (wide band gap polymer) and PBBTDPP2 (small band gap polymer).

The device layout and layer stack of the tandem solar cell is shown in Figure 2.1(a) and consists of a wide band gap bulk-heterojunction front cell connected to a small band gap bulk-heterojunction back cell in series with a recombination layer.
The front cell consists of a blend of poly[2,7-(9,9-didecylfluorene)-*alt*-5,5-(4′,7′-di-2-thienyl-2′,1′,3′-benzothiadiazole)] (PFTBT) as wide band gap donor material with [6,6]-phenyl-C_{61}-butyric acid methyl ester (PCBM) as acceptor material. The front cell is connected to the back cell *via* a recombination layer, consisting of a bilayer of ZnO nanoparticles and pH-neutral poly(3,4-ethylenedioxy-thiophene):poly(styrenesulfonic acid) (PEDOT:PSS). The back cell consists of a blend of poly[3,6-bis(4′-dodecyl-[2,2′]bithiophenyl-5-yl)-2,5-bis(2-ethylhexyl)-2,5-dihydropyrrolo[3,4-]pyrrole-1,4-dione] (PBBTDPP2) as small band gap donor material with PCBM as acceptor material. The molecular structures of PFTBT and PBBTDPP2 are shown in Figure 2.1 (b).

2.2 Electroabsorption spectroscopy

Electroabsorption (EA) spectroscopy measures the change of the absorption coefficient ($\Delta\alpha$) of a material in the presence of an electric field (E). The effect finds its origin in the fact that the electric field affects the electronic wave function of the material. For most organic materials $\Delta\alpha(\lambda)$ varies with the square of the electric field and the imaginary part of the third order susceptibility, $\mathrm{Im}\,\chi^3(\lambda)$, and can be expressed as function of the wavelength (λ) as:[23,24,40]

$$\Delta\alpha(\lambda) \propto \mathrm{Im}\,\chi^3(\lambda)\cdot E^2 \qquad (2.1)$$

For organic electronic devices with a layered sandwich structure with one transparent electrode and with one non-transparent metallic top electrode, such as

organic solar cells, the change of absorption ($\Delta\alpha$) due to an electric field can be related to a change in reflectance (ΔR) of the light passing through the cell. The change of the absorption coefficient is related to the reflectance by:[26]

$$\frac{\Delta R(\lambda)}{R(\lambda)} \propto \Delta\alpha(\lambda) \propto \mathrm{Im}\,\chi^3(\lambda)\cdot E^2 \tag{2.2}$$

To experimentally detect a small change in reflectance due to the perturbation of the electric field, a constant dc bias (V_{dc}) and a modulated ac bias (V_{ac}) with frequency f are simultaneously applied to the device:

$$V(t) = V_{dc} + V_{ac}\cdot\cos(2\pi f t) \tag{2.3}$$

In a first approximation, the active layer of an organic solar cell can be considered as an uniform dielectric such that the electric field across the layer equals $E = (V(t) - V_{BI})/L$, with V_{BI} the built-in voltage that typically arises from the difference in work function of the two electrodes and L is the thickness of the film. Combining Equations (2.2) and (2.3), the EA signal can be described by:

$$\frac{\Delta R(\lambda)}{R(\lambda)} \propto \frac{\mathrm{Im}\,\chi^3(\lambda)}{L^2}\cdot\left[(V_{dc}-V_{BI})^2 + \tfrac{1}{2}V_{ac}^2 + \tfrac{1}{2}V_{ac}^2\cdot\cos(2\cdot 2\pi f t) + 2V_{ac}(V_{dc}-V_{BI})\cdot\cos(2\pi f t)\right] \tag{2.4}$$

Equation (2.4) reveals that the EA is modulated at two different frequencies f and $2f$. For the first (f) harmonic of the EA we see that:

$$\left.\frac{\Delta R(\lambda)}{R(\lambda)}\right|_{1f} \propto \frac{2\,\mathrm{Im}\,\chi^3(\lambda)}{L^2}\cdot(V_{dc}-V_{BI})\cdot V_{ac}\cdot\cos(2\pi f t) \tag{2.5}$$

While for the second ($2f$) harmonic of the EA signal we find:

$$\left.\frac{\Delta R(\lambda)}{R(\lambda)}\right|_{2f} \propto \frac{\mathrm{Im}\,\chi^3(\lambda)}{2L^2}\cdot V_{ac}^2\cdot\cos(2\cdot 2\pi f t) \tag{2.6}$$

In a typical EA experiment, the first harmonic EA signal is determined with phase-sensitive lock-in detection referenced at the ac modulation frequency f and then measured as a function of applied dc bias (V_{dc}) with fixed small ac modulation amplitude (V_{ac}). According to Equation (2.5), V_{BI} can be determined as the V_{dc} bias where the first harmonic EA signal ($\Delta R/R|_{1f}$) cancels.

2.3 Experimental

The tandem cells used in this study have the configuration: glass/ ITO/PEDOT:PSS/ PFTBT:PCBM/ZnO/pH-neural PEDOT:PSS/PBBTDPP2:PCBM/LiF/Al (Figure 2.1). The corresponding single junction cells had the active layers sandwiched between glass/ITO/PEDOT:PSS and LiF/Al electrodes. The cells were fabricated as described by Gilot *et al*.[15] Briefly, a 50 nm PEDOT:PSS layer (Clevios P VP AI 4083) was spin coated from water on ITO patterned glass substrates. PFTBT:PCBM (1:4 wt.%) layers were spin cast from chlorobenzene solution and PBBTDPP2:PCBM (1:2 wt.%) layers were deposited from a 4:1 chloroform:*o*-dichlorobenzene solution. The intermediate contact consists of a 30 nm ZnO layer spin-cast from a solution ZnO nanoparticles in acetone and a 15 nm pH-neutral PEDOT:PSS layer (Orgacon, batch 5541073, pH = 7, 1.2 wt%, Agfa Gevaert NV). As back contact 1 nm of LiF and 100 nm of Al were thermally evaporated at a pressure of 10^{-7} mbar.

The setup that was constructed to measure EA is shown schematically in Figure 2.2. A tungsten-halogen lamp is used as illumination source and focused by a converging mirror (M1) on the slit of a monochromator to select a wavelength. Light from the monochromator is focused on the sample by mirror M2 and the light reflected from the sample is focused on a silicon photodiode using mirror M3. The incident angle and reflected angle of the light on the solar cell are approximately 45°. The sample is kept under dynamical vacuum to avoid degradation at room temperature in an Oxford cryostat. The sample is connected to a function generator (Agilent 33250A) which applies a constant dc voltage bias and a square wave modulated ac bias (V_{ac} = 0.5 – 1.0 V) at f = 30 kHz. For these conditions the EA signal scales linearly with V_{ac}. Because of the internal impedance of the function generator, V_{dc} and V_{ac} applied on the solar cell were measured with a voltmeter (Keithley 6512) and an oscilloscope (Hameg HM705). To avoid detection of spurious signals emitted from cables that apply the ac bias, the solar cell was connected to the function generator *via* coax cables of which the shields were connected to the ground. The signal was detected by the silicon diode and amplified by a home-built voltage preamplifier. A lock-in detector (Stanford research Systems SR830) was used to record the phase (θ) and amplitude (A) of the modulated signal. The in-phase signal, $A \cdot \cos\theta$, is taken as being proportional to ΔR. The reflectance (R) was measured in a separate experiment, mechanically modulating the monochromatic light, and recording modulated signal at the modulation frequency. Dividing ΔR by R gives the EA signal. Apart from the monochromatic light of the EA probe beam, no other light source was present and ambient light was excluded.

Photoinduced absorption (PIA) spectra were recorded by exciting with a mechanically modulated pump beam (λ = 830 nm, Newport- Spectra Physics

LNQ830-150C) and monitoring the resulting change in transmission of a tungsten-halogen probe light through the sample (ΔT) with a phase-sensitive lock-in amplifier after dispersion by a grating monochromator and detection, using Si, InGaAs, and cooled InSb detectors for photon energies in the range of 0.36 to 2.10 eV. The PIA ($\Delta T/T$) was corrected for the photoluminescence, which was recorded in a separate experiment. Photoinduced absorption spectra were recorded with the pump beam in a direction almost parallel to the direction of the probe beam. Samples for PIA were prepared by spin coating the PBBTDPP2:PCBM mixture from chloroform/*o*-dichlorobenzene solution on quartz substrates.

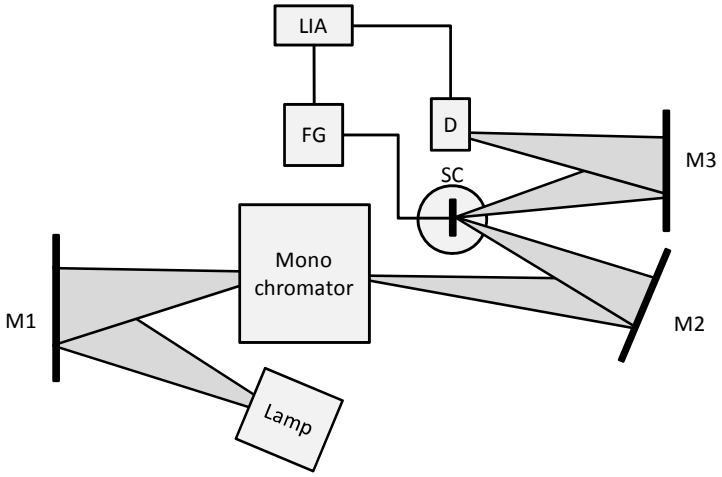

Figure 2.2: Simplified schematic of the EA setup. M1, M2, and M3 are convex mirrors used to focus the light. SC is the solar cell which is kept in dynamic vacuum with a cryostat. FG is the function generator to apply V_{dc} and V_{ac} on the solar cell. D denotes the photodiode which detects the reflected light from the solar cell and LIA denotes the lock-in amplifier.

The work function of Clevios P (−5.05 eV) and pH neutral PEDOT (−4.65 eV) was determined with scanning Kelvin probe microscopy (SKPM) using a commercial AFM system (Veeco instruments MultiMode AFM with Nanoscope IIIa controller and extender module) in a glove box under nitrogen atmosphere employing a sharp silicon tip with Pt coating and calibrated with freshly cleaved highly oriented pyrolitic graphite (HOPG), which has a stable work function of 4.48 eV.[42]

2.4 Results and discussion

2.4.1 Polymer tandem cell

The normalized absorption spectra of a PFTBT:PCBM and PBBTDPP2:PCBM films are shown in Figure 2.3(a).[15] The two materials have different optical band gaps and the spectra are complementary in the visible region. Figure 2.3(b) shows the current

voltage ($J-V$) curves under illumination of a typical tandem cell and of the individual PFTBT:PCBM front subcell and PBBTDPP2:PCBM back subcell in the tandem.[43] The device performance of the tandem cell and the individual subcells in the tandem have been determined previously[43] and are summarized in Table 2.1.

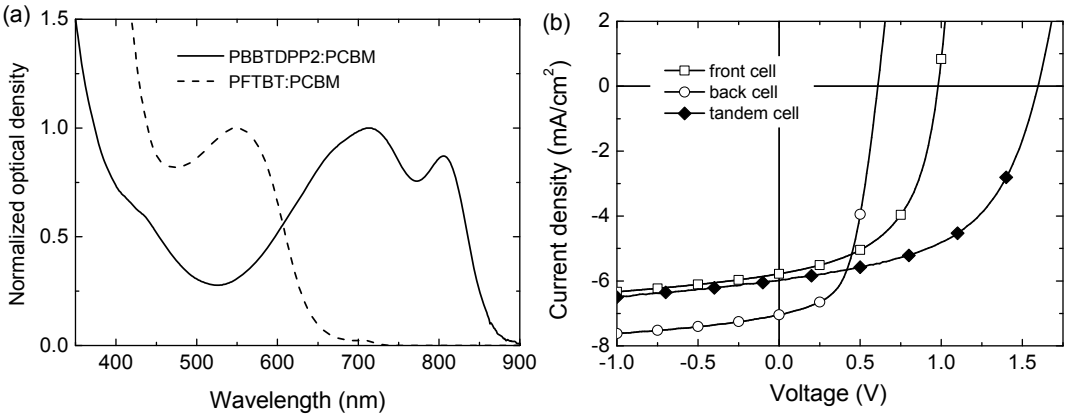

Figure 2.3: (a) Normalized absorption spectra of a PFTBT:PCBM and PBBTDPP2:PCBM films. (b) *J-V* characteristics of a tandem cell with a 180 nm thick front cell and 125 nm thick back cell. *J-V* characteristics of a single junction of a 180 nm thick PFTBT:PCBM cell and of a 125 nm thick PBBTDPP2:PCBM cell, measured at representative light intensity and of the constructed tandem cell. Reproduced from Ref. [43].

Table 2.1 Performance parameters of the tandem cell and subcells.[43]

Device	J_{SC} (mA/cm^2)	V_{OC} (V)	FF	η (%)
Tandem	5.98	1.60	0.52	5.0
Front cell	5.79	0.98	0.53	-
Back cell	7.05	0.61	0.55	-

2.4.2 EA of the tandem cell

Figure 2.4(a) shows the normalized EA spectra, measured at the first harmonic and at an applied reverse dc bias of the tandem solar cell, and of both the wide and small band gap single junction cells. Clearly, the EA spectrum of the tandem cell is the weighted sum of the EA spectra from the wide band gap front cell and of the small band gap back cell. Because no significant EA response is observed for the wide band gap single junction solar cell between 700 nm to 900 nm, the EA signal in this wavelength range of the tandem cell originates from the small band gap back cell. Between 600 and 700 nm the EA signal of the tandem is a superposition of EA spectra of both subcells. However, the EA peak at 625 nm of the tandem cell is dominated by the EA signal from the wide band gap front cell since the EA

contribution of the small band gap sub cell is small at this wavelength. Consequently, in the spectral range of 700 to 900 nm of the EA spectrum of the tandem can be used to monitor the electric field in the back cell as function of applied voltage, while the EA peak at 625 nm of the tandem cell can be used to monitor the electric field in the wide band gap front cell after correction for the contribution of the wide band gap cell.

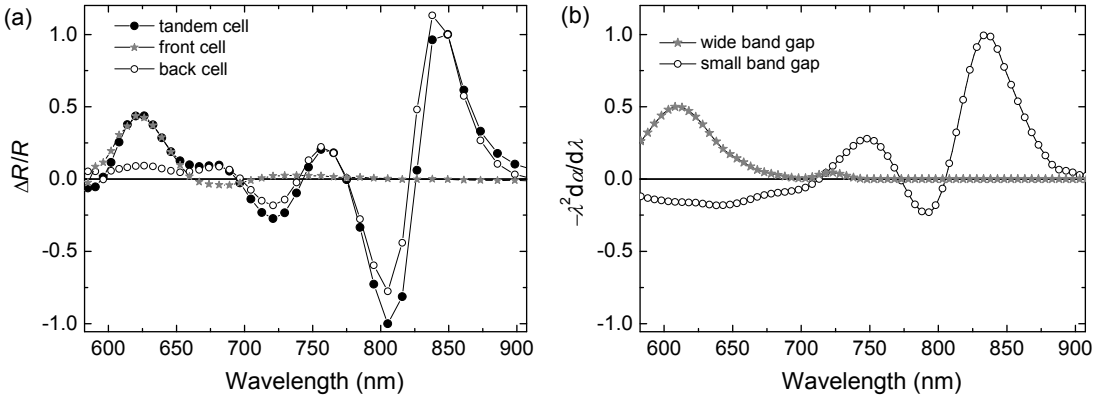

Figure 2.4: (a) EA spectrum at the first harmonic of the tandem cell (black circles) measured at $V_{dc} = -4$ V with $V_{ac} = 1$ V, $f = 30$ kHz, and normalized at 850 nm. The remaining two curves show the EA spectra of the single junction front cell (wide band gap PFTBT:PCBM, grey stars) measured at $V_{dc} = -2$ V and scaled at 625 nm to the normalized EA spectrum of the tandem cell, and of the single junction back cell (small band gap PBBTDPP2:PCBM, open circles) measured at $V_{dc} = -2$ V and normalized at 850 nm. (b) First derivative with respect to photon energy of the absorption spectra of the wide band gap (PFTBT:PCBM) and small band gap (PBBTDPP2:PCBM) thin films.

Figure 2.4(b) shows the first derivative with respect to photon energy of the linear absorption spectra of the wide band gap (PFTBT:PCBM) and small band gap (PBBTDPP2:PCBM) thin films. By comparing panels (a) and (b) in Figure 2.4 it can be seen that the first derivate spectra resemble the EA spectra. For the small band gap PBBTDPP2:PCBM film the EA shows peaks at 756, 805, and 837 nm, with corresponding peaks at 748, 791, and 835 nm in the first derivative of the absorption spectrum. For the small band gap PFTBT:PCBM film the EA spectrum shows two signals at 623 and 734 nm. The latter is weak and likely due to the EA of PCBM. In the first derivative of this film, these signals are at 610 and 721 nm, respectively. From the comparison it is clear that the EA spectra appear somewhat red shifted and are generally better resolved than in the absorption spectra. This effect has also been observed by Liess *et al.* for conjugated polymers and has been rationalized in terms of the disorder in conjugation lengths.[44] Since the absorption spectrum probes all conjugation lengths, with shorter chain fragments appearing blue shifted from longer

chain fragments, a rather featureless spectrum appears when there is disorder in conjugation lengths. EA, on the other hand, is a χ^3 process and preferentially probes the longer chain lengths, giving rise to sharper and more red-shifted spectral features.[44]

The EA spectra of the tandem cell are shown in Figure 2.5(a) as function of V_{dc}, for $-4 \leq V_{dc} \leq +2$ V. The intensity of the EA peak at 625 nm, which is attributed to mainly stemming from the wide band gap front cell, decreases when V_{dc} is increased and cancels near +2 V. The EA signal scales with the electric field in the front cell, and hence the reduction of the EA intensity can be attributed to a decrease of the internal electric field in the front cell when V_{dc} over the tandem increases to 2 V. Such a decrease of the internal electric field across the subcells is expected when V_{dc} approaches the open-circuit voltage, but here the signal cancels at $V_{dc} > V_{OC}$. As can be seen the decrease of the EA signal with V_{dc} is not linear above 0 V. Linear regression of the data for $V_{dc} \leq -1$ V, results in an extrapolated $V_{dc} \approx +3.3$ V for the extinction of the EA signal (Figure 2.5(b)).

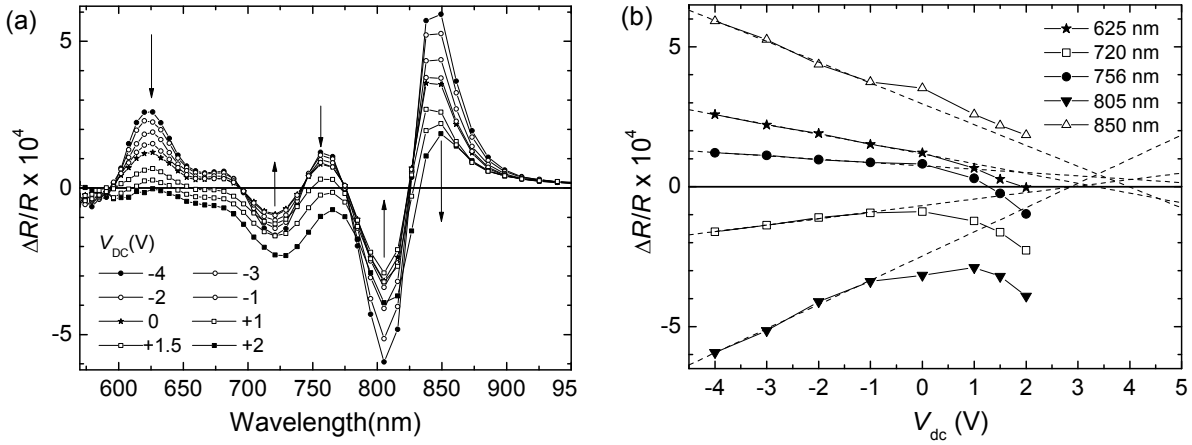

Figure 2.5: (a) EA spectra (first harmonic) of the tandem cell for $-4 \leq V_{dc} \leq +2$ V, measured at $V_{ac} = 1$ V and $f = 30$ kHz. The arrows indicate the wavelengths that have been used to construct panel (b). (b) EA signals of the tandem as a function of V_{dc} at 625 (front cell) and at 720, 756, 805, and 850 nm (back cell). The dashed lines are linear fits and extrapolations to the data points in the range $-4 \leq V_{dc} \leq -1$ V.

In the spectral range from 700 to 900 nm the EA response does not vary in a consistent fashion with the applied V_{dc}. To better illustrate the change in the EA spectrum of the small band gap back cell of the tandem cell, the EA signal intensities at the peak position 720, 756, 800, and 850 nm are plotted in Figure 2.5(b) as a function of V_{dc} over the tandem. It is clear that at each of the selected wavelengths the EA signal varies linearly with V_{dc} only for $-4 \leq V_{dc} \leq -1$ V. From $V_{dc} > -1$ V onwards, the behavior is non-linear and the changes of the EA intensity with V_{dc}

differ for different wavelengths. The EA peaks at 720 and 805 nm do not change sign but increase again after reaching a minimum value between V_{dc} = 0 and +1 V. In contrast, the EA peak at 756 nm continues to decrease, changes sign around +1 V, and then increases again in magnitude. The EA peak at 850 nm decreases in the entire range studied, but does not extinguish.

The linear dependence of the EA signals with V_{dc} for $-4 \leq V_{dc} \leq -1$ V is in accordance with Equation (2.5), which predicts such behavior for a single junction solar cell. In a tandem device, the EA signal of the back and (front) cell is expected to vary linearly with the applied dc bias on the back (front) cell and is expected to depend on Equation (2.5):

$$\left.\frac{\Delta R(\lambda)}{R(\lambda)}\right|_{1f}^{BC} \propto \mathrm{Im}\,\chi^3(\lambda)\cdot(V_{dc}^{BC} - V_{BI}^{BC})\cdot V_{ac}^{BC} \tag{2.7}$$

With V_{dc}^{BC} the dc bias applied on the back cell, V_{ac}^{BC} the ac modulation amplitude applied to the back cell and V_{BI}^{BC} the built-in voltage of the back cell.

The applied dc (ac) bias on the back cell will be a fraction of the applied dc (ac) bias on the tandem cell and can be written as:

$$V_{dc(ac)}^{BC} = c\cdot V_{dc(ac)}^{tandem} \tag{2.8}$$

Where *c* is a coefficient between 0 and 1 and denotes the fraction. The voltage on the front cell can then be expressed as:

$$V_{dc(ac)}^{FC} = (1-c)\cdot V_{dc(ac)}^{tandem} \tag{2.9}$$

The EA signal from the back cell can be written as a function of the tandem bias:

$$\left.\frac{\Delta R(\lambda)}{R(\lambda)}\right|_{1f}^{BC} \propto \mathrm{Im}\,\chi^3(\lambda)\cdot(c\cdot V_{dc}^{tandem} - V_{BI}^{BC})\cdot c\cdot V_{ac}^{tandem} \tag{2.10}$$

If *c* is constant with the applied dc bias, then the EA signal from the back (front) subcell should vary linearly with the applied dc bias on the tandem cell (V_{dc}^{tandem}). Furthermore, the EA signals are expected to cancel at the applied bias on the tandem cell when $V_{dc}^{tandem} = c^{-1}\cdot V_{BI}^{BC}$ for the back cell according Equation (2.10) and when $V_{dc}^{tandem} = (1-c)^{-1}\cdot V_{BI}^{FC}$ for the front cell.

Figure 2.5(b) shows that for $V_{dc}^{tandem} < -1$ V, the EA signals vary linearly with applied V_{dc}^{tandem} and, hence, c can be considered independent of applied bias in this range. For the front cell, Figure 2.5(b) gives an extrapolated $V_{dc}^{tandem} = (1-c)^{-1} \cdot V_{BI}^{FC} =$ +3.3 V for the EA signal at 625 nm. For the back cell, the situation is more complicated. Based on a linear extrapolation of the EA signals for $-4 \leq V_{dc}^{tandem} \leq -1$ V, the EA signals would cancel at V_{dc}^{tandem} equal to +2.9 V for the EA at 720 nm, +6.3 V at 756 nm, +2.9 V at 805 nm, and +4.0 V for the 850 nm. It is clear that this is a too large variation to be useful. A somewhat more consistent picture is obtained from analyzing the crossing point of the extrapolated EA signals of the back cell which occurs for $V_{dc}^{tandem} = +3.4 \pm 0.6$ V (Figure 2.5(b)). This is close to the value of $V_{dc}^{tandem} =$ +3.3 V where the EA signal cancels for the front cell.

As shown in Figure 2.5(b), the EA signals of the back cell stop to vary linearly with V_{dc}^{tandem} above −1 V. According to Equation (2.10), this implies that c is not constant with the applied bias and is a function of the applied bias, $c = c(V_{dc})$. However, even when $c = c(V_{dc})$ the EA signals should vary in a similar fashion with V_{dc}^{tandem} for different wavelengths. Figure 2.4(b) shows that this is not the case for the EA signals at 720, 756, 805, and 850 nm. This either implies that c is not constant with wavelength and then the EA signal at different wavelengths can be canceled at different applied biases on the tandem cell ($V_{dc}^{tandem} = c(\lambda)^{-1} \cdot V_{BI}^{BC}$). Or it implies that the EA spectrum of the small band gap single junction solar cell the EA signal varies differently with DC bias at different wavelength and Equation (2.5) is not valid for all wavelengths.

To study the electric field distribution on the different sub cell of the tandem it is crucial to better understand how the EA signals of the individual single junction cells vary at different wavelength with applied bias. In the following sections we address these questions.

2.4.3 EA of the wide band gap cell

The EA spectra of a PFTBT:PCBM wide band gap solar cell recorded as a function of V_{dc} are shown in Figure 2.6(a). The EA spectra were recorded over the narrow wavelength range of the main EA peak at the onset of absorption to reduce measurement time. The EA signal recorded in the range from 620 to 640 nm varies linearly V_{dc} as shown in Figure 2.6(b). A linear fit of the EA signal to Equation (2.5) yields a built-in voltage close to $V_{BI} = 1.49 \pm 0.05$ V for the plotted wavelengths. We note that the variation of the determined built-in voltage would increase when

considering wavelengths where the EA signal is low, as can be clearly seen for 596 and 652 nm in Figure 2.6(a).

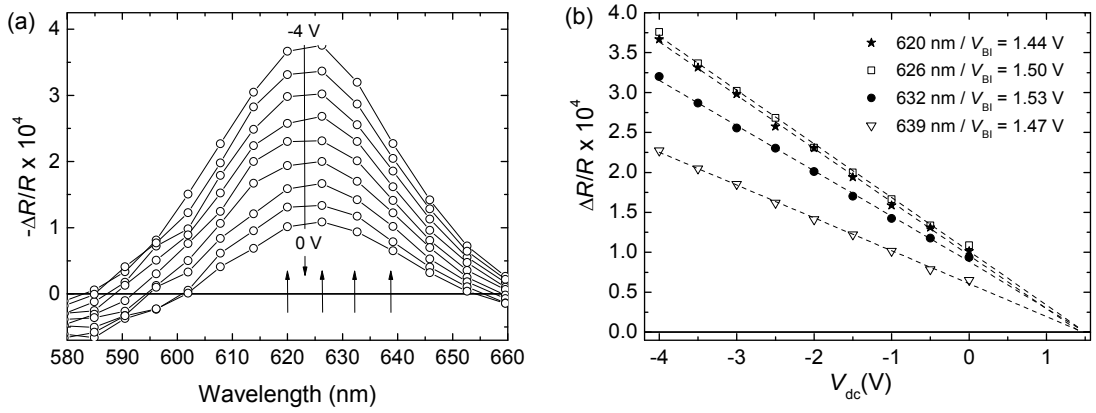

Figure 2.6: (a) EA spectra (first harmonic) of the single junction PFTBT:PCBM cell for $-4 \leq V_{dc} \leq 0$ V, measured at $V_{ac} = 1$ V and $f = 30$ kHz. The arrows indicate the wavelengths used to construct panel (b). (b) EA signals of the PFTBT:PCBM cell a function of V_{dc} at different wavelengths. The dashed lines are linear fits and extrapolations to the data in the range $-4 \leq V_{dc} \leq 0$ V.

A V_{BI} of 1.49 ± 0.05 V, is larger than expected based on the difference in the work functions of PEDOT:PSS (−5.05 eV, determined from SKPM) and Al (−4.1 eV).[30] Several mechanisms and processes can rationalize the difference. First, Brown *et al.* have established that for polymer light-emitting diodes with a LiF/Al electrode V_{BI} increases with the thickness of the LiF interlayer ($0 \leq d \leq 11$ nm).[45] For a ~0.9 nm layer, as used here, the increase of V_{BI} equals 0.6 V. This change would bring $V_{BI} \approx$ 1.6 V, close to the value found from the EA experiments. An alternative explanation can be found in the work of Lane *et al.*[30] and Brewer *et al.*[32] By comparing polyfluorene diodes using ITO or PEDOT:PSS anodes with Al cathodes, they found an average increase in V_{BI} of 0.7 V with the PEDOT:PSS electrode compared to ITO, much larger than the difference in work function. They attribute this effect to the presence of electrons trapped at the PEDOT:PSS/polyfluorene interface that pin the Fermi level to the low lying HOMO of the polyfluorene. This pinning is different from conventional pinning which would occur if the work function of the anode is higher than the ionization potential of the layer, or the work function of the cathode is less than the electron affinity. The electron trapping at the PEDOT:PSS/polymer interface and the consequence for V_{BI} is explained in more detail in Ref. [28]. A similar result was obtained by Van Woudenberg *et al.* who established a strongly enhanced hole injection into a polyfluorene with a low energy HOMO for PEDOT:PSS, compared to Ag or ITO.[46]

Considering these effects, we note that the experimental built-in voltage of V_{BI} of 1.49 ± 0.05 V is consistent with Ohmic contacts forming between PFTBT and the PEDOT:PSS electrode and between PCBM and the LiF/Al electrode. In that case the energy levels of the highest occupied molecular orbital (HOMO) of the PFTBT at −5.6 eV[47] and of the lowest occupied molecular orbital (LUMO) level of PCBM at −4.2 eV, determine the built-in voltage at 1.4 V. We also note that the built-in voltage of V_{BI} = 1.49 ± 0.05 V is close to the energy of charge transfer state of the PFTBT:PCBM 1:4 wt.-% blend which is at 1.48 eV.[48]

With V_{BI} = 1.49 ± 0.05 V for the wide band gap single junction cell determined at 625 nm, can be compared to the dc bias (V_{dc}^{tandem} = +3.3 V) at which the EA signal cancels in the front subcell of the tandem cell. *Via* Equation (2.9) it is then possible to determine c = 0.55, which is slightly smaller than the ratio of 0.61 of the V_{OC}'s of the front cell and the tandem cell (Table 2.1).

2.4.4 EA of the small band gap cell

Figures 2.7(a) shows the EA spectra measured on a small band gap PBBTDPP2:PCBM single junction cell for $-4 \leq V_{dc} \leq 0$ V. Figure 2.7(b) depicts the EA signal intensities for selected wavelengths and reveals that decays are not precisely linear with V_{dc}. The dashed lines in Figure 2.7(b) represent linear extrapolations of a fit to the data in the limited range of $-4 \leq V_{dc} \leq -3$ V. The deviation of the experimental data from the extrapolations for $V_{dc} > -3$ V emphasize the non-linear dependence of the EA on V_{dc}. This is especially true for the signals at 805 and 837 nm. Similar to the EA of the small band gap subcell of the tandem (Figure 2.5(b)) the lines do not cross in a single point at the horizontal axis and hence V_{BI} cannot be determined. Figure 2.7(a) shows furthermore that the EA spectrum shifts with V_{dc}, especially in the region between 800 and 900 nm. Figure 2.7(c) shows an EA experiment on a PBBTDPP2:PCBM single junction cell for $-4 \leq V_{dc} \leq 0$ V in a narrow wavelength range, which substantiates the spectral changes of the EA signal with V_{dc}. The spectral changes point out that the EA spectra consist of at least two different components exhibiting a different electric field dependence. One component, is undoubtedly the EA signal that originates from the Stark effect of the PBBTDPP2:PCBM blend and is proportional to both V_{dc} and the imaginary part of the third order susceptibility (Im $\chi^3(\lambda)$) as described by Equation (2.5). We have identified the second component as being due to the spectral characteristics of charge carriers present in the blend.

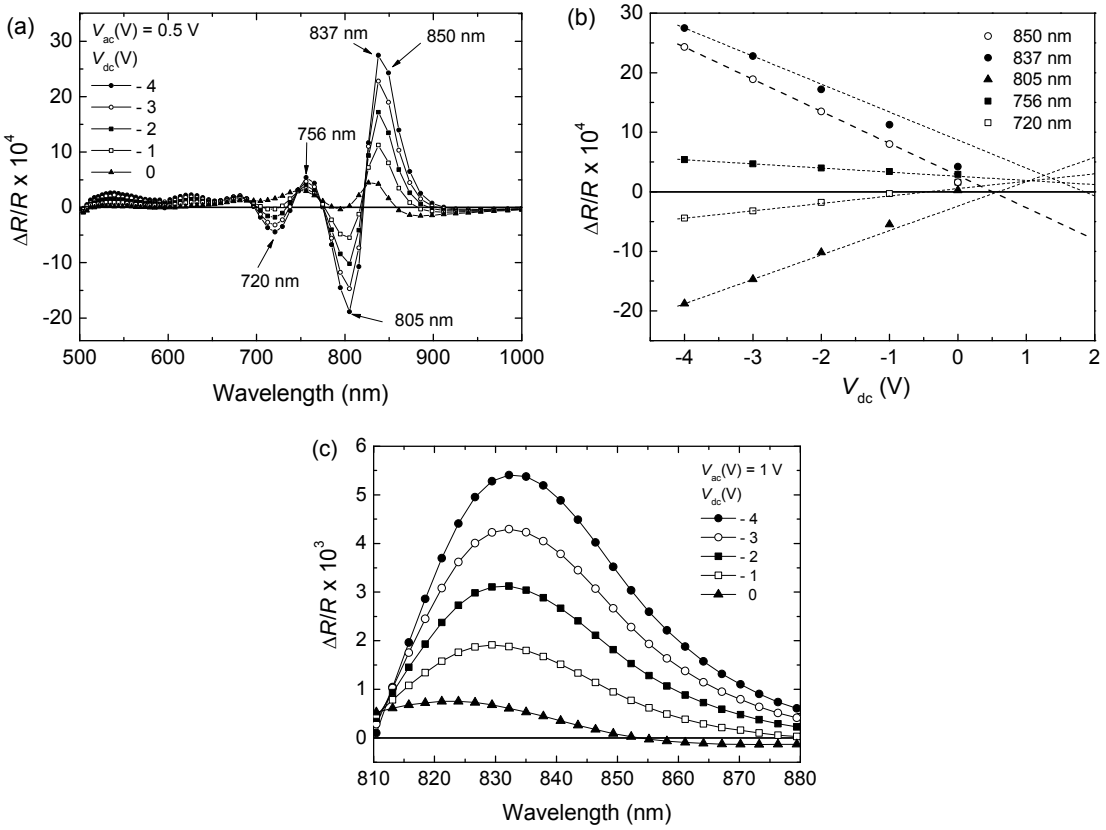

Figure 2.7: (a) EA spectra (first harmonic) of a single junction PBBTDPP2:PCBM cell for $-4 \leq V_{dc} \leq 0$ V, measured at V_{ac} = 0.5 V and f = 30 kHz. The arrows indicate the wavelengths that have been used to construct panel (b). (b) EA signals of the PBBTDPP2:PCBM cell a function of V_{dc} at 720, 756, 805, 837, and 850 nm. The dashed lines are linear fits and extrapolations to the data points in the range $-4 \leq V_{dc} \leq -3$ V. (c) EA spectra (first harmonic) of single junction PBBTDPP2:PCBM cells for $-4 \leq V_{dc} \leq 0$ V, measured at V_{ac} = 1 V and f = 30 kHz.

Evidence for this assignment can be found in comparing the EA spectrum recorded at V_{dc} = +0.5 V, *i.e.* close to V_{OC} with the near-steady state photoinduced absorption (PIA) of a thin PBBTDPP2:PCBM blend film on quartz recorded at room temperature. Figure 2.8(a) compares the two spectra, after normalizing the EA spectrum to the PIA signal. The similarity is evident. The PIA spectrum of the PBBTDPP2:PCBM blend is shown in the full wavelength range in Figure 2.8(b). Upon illumination $PBBTDPP2^+$ radical cations and $PCBM^-$ radical anions are formed in the blend *via* a photoinduced electron transfer reaction. This results in a bleaching of the ground state where $\Delta T/T$ is positive in the range λ = 650−850 nm and an induced absorption of the charges in the range for λ > 850 nm where $\Delta T/T$ is negative (Figure 2.8(b)). The signals at 1455 and >3450 nm in Figure 2.8(b) are assigned to the $D_2 \leftarrow D_0$ and $D_1 \leftarrow D_0$ transitions of $PBBTDPP2^+$ and are characteristic for doublet-state radical cations (polarons) of conjugated polymers.[49] Based on this

assignment and the correspondence between the EA signal at V_{dc} = +0.5 V and the PIA spectrum (Figure 2.8(a)), there is little doubt that the spectral characteristics of charge carriers appear as a component in the EA spectrum.

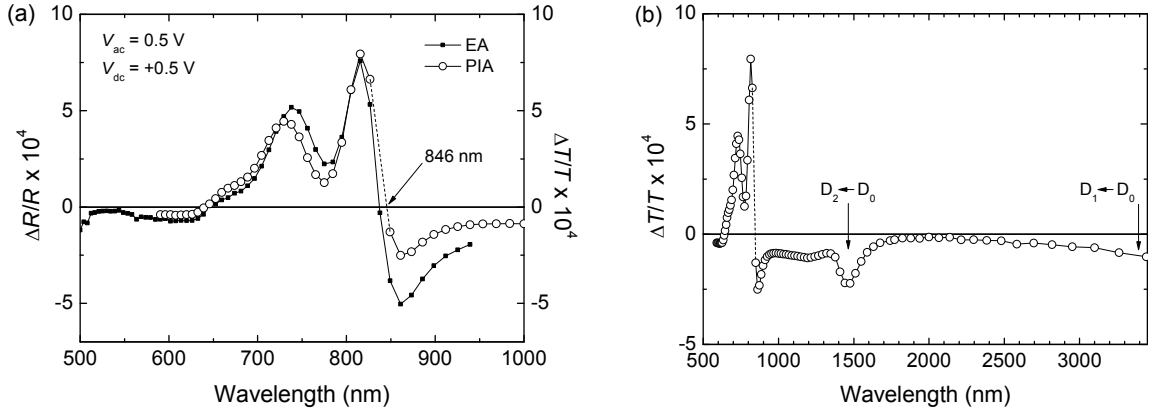

Figure 2.8: (a) Comparison of EA spectra (first harmonic) of the single junction PBBTDPP2:PCBM cell for V_{dc} = +0.5 V (V_{ac} = 0.5 V and f = 30 kHz) and the PIA spectrum recorded for a PBBTDPP2:PCBM layer at room temperature with excitation at λ = 830 nm. (b) PIA spectrum recorded for a PBBTDPP2:PCBM layer at room temperature with excitation at λ = 830 nm. The dashed lines in the spectral region around λ = 830 nm are a linear interpolation. In this region the PIA spectrum could not be determined because it coincides with the excitation wavelength.

To emerge as a $\Delta R/R$ signal in the EA spectra, the concentration of charge carriers must be modulated by the applied ac field (V_{ac} = 0.5 V and f = 30 kHz). The origin of the charges that appear in the EA signal can be twofold. First, we consider that the charges are created by the EA probe light and collected at the electrodes at the applied reverse V_{dc} bias. The J–V curve (Figure 2.3(b)) shows that the current collected varies with V_{dc} and that when V_{dc} approaches V_{OC}, a constant ac bias V_{ac} results in a larger modulation of the current. Under constant illumination a variation in collected current implies a variation in the number of charges that remain in the film. Hence, when V_{dc} approaches V_{OC} the signal of the charges in EA spectrum is expected to increase. Indeed, this is what can be observed in Figure 2.7(a) although it is not really possible to quantify the increase because of the simultaneous decrease of the EA signal. The second explanation is that charges are injected from the PEDOT:PSS and LiF/Al contacts into the active layer when V_{dc} approaches V_{OC}, especially when $V_{dc} + 0.5 \times V_{ac} > V_{OC}$. We consider both mechanisms probable and possibly both contribute to the $\Delta R/R$ signal.

We note that for the PFTBT:PCBM solar cell no clear contribution of charges has been observed in the EA spectra. One reason may be that less charges are created or injected in this blend, but we also note that the PIA spectrum of PFTBT:PCBM shows a broad bleaching signal in the wavelength range between 480 and 660 nm, and maximizes at 580 nm.[48] This is much broader than the EA signal and hence a small contribution of charges may go unnoticed.

The PIA spectra for PBBTDPP2:PCBM blends were recorded with excitation at 830 nm and close to this wavelength the PIA signal is obscured by scattering of pump light. In Figure 2.8(a) and (b) we have interpolated the PIA signal to determine that $\Delta T/T = 0$ at $\lambda \approx 846$ nm. This isosbestic point, where charge formation or injection does not contribute to the EA spectrum because the induced absorption and bleaching signals cancel, can possibly be used to determine V_{BI}. Figure 2.7(b) shows that at $\lambda \approx 850$ nm the data points in the range $-4 \leq V_{dc} \leq -1$ V fit well to the dashed line, but that at $V_{dc} = 0$ there is still some deviation. Taking these data and extrapolating we find $V_{BI} = 0.52$ V. This is less than the difference in the work functions of the PEDOT:PSS (−5.05 eV) and Al (−4.1 eV).[30] In section 2.4.3 we established that for PFTBT:PCBM the V_{BI} (1.49 ± 0.05 V) was close to the donor-HOMO – acceptor LUMO energy difference and to the CT state energy. The lower V_{OC} of the PBBTDPP2:PCBM single junction cell compared to the PFTBT:PCBM cell, indicates that the donor-HOMO – acceptor LUMO difference is about 0.4 eV less in the small band gap cell than in the wide band gap cell, and likewise for the CT energy. Hence if Ohmic contacts are formed and determine the built-in potential, the expected value would be $V_{BI} \approx 1.2$ V.

In conclusion, V_{BI} can only be determined with very limited accuracy with EA for these films. This precludes an accurate determination of the internal electric field in the small band gap subcell of the tandem device.

2.5 Conclusions

We have explored the use of electroabsorption (EA) spectroscopy as a technique to determine the internal electric fields in the individual subcells of polymer tandem solar cells. While the contributions of the wide and small band gap materials can readily be identified in the EA spectra of the tandem cell and can also be monitored as function of an externally applied bias, an accurate quantification of the internal electric field is hampered by a non-linear dependence of the EA signal intensity as function of the applied bias. In the present example the non-linear dependence was identified as being due to a change in the ratio of two different components contributing to the EA spectrum of the small band gap subcell. The two spectral components have been identified as the Stark effect and the absorption of charge

carriers electrically or optically induced into the active layer in the EA experiment. Both spectral contributions depend on the applied external bias, but it has not been possible to disentangle their separate bias dependencies. We note in this respect, that other sources of a non-linear dependence of the EA signal can occur. For OLEDs this has been addressed in detail by De Vries *et al*., who showed that Equation (2.5), which is based on a uniform electric field across the active layer, is no longer valid when band bending at the injecting contacts occurs in combination with non-uniform absorption profile of the probe light.[35]

Based on these results and considerations, we consider that EA spectroscopy is not a viable technique to routinely determine the internal electric fields in the subcells of tandem polymer solar cells. Secondary effects prevent extracting accurate data. Especially the contribution of the spectral signatures of charges to the EA spectra, will increase when tandem cells are studied under white bias light to simulate operating conditions.

2.6 References

[1] Y. Liang, Z. Xu, J. Xia, S.-T. Tsai, Y. Wu, G. Li, C. Ray, L. Yu, *Adv. Mater.* **2010**, *22*, E135.

[2] Z. He, C. Zhong, X. Huang, W.-Y. Wong, H. Wu, L. Chen, S. Su, Y. Cao, *Adv. Mater.* **2011**, *23*, 4636.

[3] Z. He, C. Zhong, S. Su, M. Xu, H. Wu, Y. Cao, *Nat. Photon*, **2012**, *6*, 593

[4] M. C. Scharber, D. Mühlbacher, M. Koppe, P. Denk, C. Waldauf, A. J. Heeger, C. L. Brabec, *Adv. Mater.* **2006**, *18*, 789.

[5] L. J. A. Koster, V. D. Mihailetchi, P. W. M. Blom, *Appl. Phys. Lett.* **2006**, *88*, 093511.

[6] D. Veldman, S. C. J. Meskers, R. A. J. Janssen, *Adv. Funct. Mater*. **2009**, *19*, 1939.

[7] T. Kirchartz, K. Taretto, U. Rau, *J. Phys. Chem. C* **2009**, *113*, 17958.

[8] N. C. Giebink, G. P. Wiederrecht, M. R. Wasielewski, S. R. Forrest, *Phys. Rev. B* **2011**, *83*, 195326.

[9] L. J. A. Koster, S. E. Shaheen, J. C. Hummelen, *Adv. Energy Mater.* **2012**, *2*, 1246.

[10] M. Gruber, J. Wagner, K. Klein, U. Hörmann, A. Opitz, M. Stutzmann, W. Brütting, *Adv. Energy Mater.* **2012**, *2*, 1100.

[11] G. Dennler, M. C. Scharber, T. Ameri, P. Denk, K. Forberich, C. Waldauf, C. J. Brabec, *Adv. Mater.* **2008**, *20*, 579.

[12] J. Gilot, M. M. Wienk, R. A.J. Janssen, *Appl. Phys. Lett.* **2007**, *90*, 143512.

[13] J. Y. Kim, K. Lee, N. E. Coates, D. Moses, T.-Q. Nguyen, M. Dante, A. J. Heeger, *Science* **2007**, *317*, 222.

[14] S. Sista, M.-H. Park, Z. Hong,Y. Wu, J. Hou, W. L. Kwan, G. Li, Y. Yang, *Adv. Mater.* **2009**, *22*, 380.

[15] J. Gilot, M. M. Wienk, R. A.J. Janssen *Adv. Mater.* **2010**, *22*, E67–E71.

[16] C. H. Chou, W. L. Kwan, Z. R. Hong, L. M. Chen, Y. Yang, *Adv. Mater.* **2011**, *23*, 1282.

[17] L. T. Dou, J. B. You, J. Yang, C.-C. Chen, Y. J. He, S. Murase, T. Moriarty, K. Emery, G. Li, Y. Yang, *Nat. Photonics* **2012**, *6*, 180.

[18] L. Dou, J. You, J. Yang, C.-C. Chen, Y. He, S. Murase, T. Moriarty, K. Emery, G. Li, Y. Yang, *Nat. Photon.* **2012**, *6*, 180.

[19] V. S. Gevaerts, A. Furlan, M. M. Wienk, M. Turbiez, R. A. J. Janssen, *Adv. Mater.* **2012,** *24*, 2130.

[20] S. Kouijzer, S. Esiner, C. H. Frijters, M. Turbiez, M. M. Wienk, and R. A. J. Janssen, *Adv. Energy Mater.* **2012**, *2*, 945.

[21] L. Dou, J. Gao, E. Richard, J. You, C.-C. Chen, K, C. Cha, Y. He, H. Li, Y. Yang, *J. Am. Chem. Soc.* **2012**, *134*, 10071.

[22] J. Gilot, M. M. Wienk, and R. A. J. Janssen, *Org. Electron.* **2011**, *12*, 660.

[23] I. H. Campbell, M. D. Joswick, I. D. Parker, *Appl. Phys. Lett.* **1995**, *67*, 3171.

[24] I. H. Campbell, T. W. Hagler, D. L. Smith, J. P. Ferraris, *Phys. Rev. Lett.* **1996**, *76*, 1900.

[25] C. M. Heller, I. H. Campbell, D. L. Smith, N. N. Barashkov, J. P. Ferraris, *J. Appl. Phys.* **1997,** *81*, 3227.

[26] T. M. Brown, J. S. Kim, R. H. Friend, F. Cacialli, R. Daik, W. J. Feast, *Appl. Phys. Lett.* **1999**, *75*, 1679.

[27] S. J. Martin, G. L. B. Verschoor, M. A. Webster, A. B. Walker, *Org. Electron.* **2002,** *3*, 129.
[28] P. J. Brewer, P. A. Lane, J. deMello, D. D. C. Bradley, J. C. deMello, *Adv. Funct. Mater.* **2004**, *14*, 562.
[29] P. J. Brewer, P. A. Lane, J. Huang, A. J. deMello, D. D. C. Bradley, J. C. deMello, *Phys. Rev. B* **2005**, *71*, 205209.
[30] P. A. Lane, P. J. Brewer, J. Huang, D. D. C. Bradley, J. C. deMello, *Phys. Rev. B* **2006**, *74*, 125320.
[31] P. J. Brewer, A. J. deMello, J. C. deMello, P. A. Lane, D. D. C. Bradley, R. Fletcher, J. O'Brien, *J. Appl. Phys*. **2006**, *99*, 114502.
[32] P. J. Brewer, J. Huang, P. A. Lane, A. J. deMello, D. D. C. Bradley, J. C. deMello, *Phys. Rev. B* **2006**, *74*, 115202.
[33] V. Bodrozic, M. Roberts, N. Philips, J. H. Burroughes, S. Mian, F. Cacialli, *J. Appl. Phys.* **2007**, *101*, 084507.
[34] C. V. Hoven, J. Peet, A. Mikhailovsky, T. Nguyen, *Appl. Phys. Lett.* **2009,** *94*, 033301.
[35] R. J. de Vries, S. L. M. van Mensfoort, R. A. J. Janssen, R. Coehoorn, *Phys. Rev. B.* **2010**, *81*, 125203.
[36] P. A. Lane, J. Rostalski, C. Giebeler, S. J. Martin, D. D. C. Bradley, D. Meissner. *Sol. Energy Mater. Sol. Cells* **2000**, *63,* 3−13
[37] I. Hiromitsu, Y. Murakami, T. Ito, Synth. Met. **2003**, *137*, 1385−1386
[38] B. Zimmermann, M. Glathaar, M. Niggeman, M. Riede, A. Hinsch, *Thin Solid Films* **2005**, *493*, 170.
[39] C. Lungenschmied, G. Dennler, H. Neugebauer, N. S. Sariciftci, E. Ehrenfreund, *Appl. Phys. Lett.* **2006**, *89*, 223519.
[40] D. E. Aspnes, J. E. Rowe, *Phys. Rev. B* **1972**, *5*, 4022.
[41] L. Sebastian, G. Weiser, H. Bässler, *Chem. Phys.* **1981**, *61*, 125.
[42] W. N. Hansen, G. J. Hansen, *Surf. Sci.* **2001**, *481*, 172.
[43] J. Gilot, M. M. Wienk, R. A. J. Janssen, *Adv. Funct. Mater.* **2010**, *20*, 3904.
[44] M. Liess, S. Jeglinski, Z. V. Vardeny, M. Ozaki, K. Yoshino, Y. Ding, T. Barton, *Phys. Rev. B.* **1997**, *56*, 15712.
[45] T. M. Brown, R. H. Friend, I. S. Millard, D. J. Lacey, J. H. Burroughes, F. Cacialli, *Appl. Phys. Lett.* **2000**, *77*, 3096.
[46] T. J. Woudenberg, J. Wildeman, P. W. M. Blom, J. J. A. M. Bastiaansen, B. M. W. Langeveld-Voss*, Adv. Funct. Mater*. **2004**, *14*, 679.
[47] D. Veldman, S. C. J. Meskers, R. A. J. Janssen, *Adv. Funct. Mater.* **2009**, *19*, 1939.
[48] D. Veldman, Ö. İpek, S. C. J. Meskers, J. Sweelssen, M. M. Koetse, S. C. Veenstra, J. M. Kroon, S. S. van Bavel, J. Loos, R. A. J. Janssen, *J. Am. Chem. Soc.* **2008**, *130*, 7721.
[49] J. C. Bijleveld, V. S. Gevaerts, D. Di Nuzzo, M. Turbiez, S. G. J. Mathijssen, D. M. de Leeuw, M. M. Wienk, and R. A. J. Janssen, *Adv. Mater.* **2010**, *22*, E242.

3 Photocurrents in polymer solar cells

Abstract

In this chapter, we determine and analyze the photocurrent (J_{ph}) in polymer solar cells under conditions where, no, one, or two different charge carriers can be injected by choosing appropriate electrodes and compare the experimental results to simulations based on a drift-diffusion device model that accounts for photogeneration and Langevin recombination of electrons and holes. We demonstrate that accounting for the series resistance of the device is essential to determine J_{ph}. Without such correction, the results are, even qualitatively, incorrect. We show that in solar cells with forward bias applied J_{ph} is reduced by recombination of photogenerated charge carriers with injected charge carriers. Self-selective contacts or band bending are not necessary to explain the effects. Without injecting contacts J_{ph} is symmetric around the compensation voltage. A simple analytical model shows that under high forward bias J_{ph} scales inversely with $1 + \xi\gamma_{pre}$, in which γ_{pre} represents the extent of Langevin recombination and ξ is a positive constant.

3.1 Introduction

Polymer solar cells generally consist of two complementary organic semiconductors with energy levels offset.[1] Absorption of light in either of the two materials produces an exciton which dissociates into electrons and holes when it diffuses to the interface of the two semiconductors. Because the exciton diffusion length in organic semiconductors is limited to about 10 nm, polymer solar cells often use a bulk heterojunction architecture in which the two materials are mixed into an interpenetrating nanoscopic network to ensure efficient exciton dissociation. Polymer solar cells further use two electrodes with different work functions to create a built-in electrical field that causes the photogenerated electrons and holes to be separated spatially and be collected. Hence, the work function difference of the two electrodes determines the polarity of the device and limits its open circuit voltage (V_{oc}), provided the difference is less than the energy of the interfacial charge separated state.[2,3] To maximize V_{oc}, the electrode materials are chosen such that their work functions are able to create Ohmic contacts with the photoactive layer.[4] This is achieved when the work function of the hole collecting contact aligns with the highest occupied molecular orbital (HOMO) level of the electron donor, *p*-type material, and that of the electron collecting contact with the lowest unoccupied molecular orbital (LUMO) of the electron acceptor, *n*-type material.

In this particular alignment of energy levels the device acts as a diode in the dark because only for voltages higher than the built-in voltage (forward bias), carriers can be injected and transported through the device. Under illumination and in reverse bias, where injection is largely inhibited, the current is determined by the amount of photogenerated free charge carriers, their transport through the active layer, the recombination between carriers, and their collection at the electrode. In forward bias, the situation is more complex because injected and photogenerated carriers are present simultaneously. In optimizing the performance of polymer solar cells the electric field dependence of the photocurrent density (J_{ph}), defined as the difference between the illumination (J_{light}) and dark current densities (J_{dark}), $J_{ph} = J_{light} - J_{dark}$, is an important parameter. Ideally J_{ph} would be weakly dependent on the electric field because this would maximize the fill factor (*FF*) of the solar cell and thereby the power conversion efficiency.

One way to probe the electric field dependence of photogenerated carriers is to measure the photocurrent. In reverse bias, where the dark current is virtually zero the photocurrent is equal to the illumination current ($J_{ph} = J_{light}$). However, in forward bias where also the injected charges contribute, the photocurrent cannot be determined reliably from standard current density − voltage ($J-V$) measurements. Ooi *et al.* demonstrated that the photocurrent is easily overestimated under

illumination since the sample heats up such that the dark and illumination currents are measured at different temperatures.[5] An elegant solution to suppress the effect of heating the substrate under illumination is to use a pulsed white LED.[5] By keeping the on-off cycles of the LED shorter than the cooling and heating time of the sample, the dark and illumination current are measured at the same temperature.

With this technique Ooi *et al.* studied photocurrent generation in poly(3-hexylthiophene):[6,6]phenyl-C_{61}-butyric acid methyl ester (P3HT:PCBM) solar cells sandwiched between a transparent indium tin oxide electrode covered with poly(3,4-ethylenedioxythiophene):polystyrenesulfonate (PEDOT:PSS) and an aluminum back electrode. They observed that the $J_{ph}-V$ curve is nearly symmetric around a well-defined point called the point of optimal symmetry (POS).[5] The POS is observed to occur at a nonzero photocurrent such that the photocurrent is asymmetric around $J_{ph} = 0$ and, hence, different under forward bias as compared to reverse bias. According to Ooi *et al.* the POS is located at the build-in voltage ($V_{pos} = V_{bi}$) and corresponds to the flat band condition of the solar cell. The $J_{ph}-V$ curve can be decomposed into a voltage (field) dependent $J_{ph}(V)$ component and a constant voltage independent $J_{ph}(V_{pos})$ component. Ooi *et al.* explained that the voltage independent $J_{ph}(V_{pos})$ component results from a net diffusive photocurrent due to self-selective electrodes. A self-selective electrode is an electrode which collects only one type of charge carrier and blocks the other type of carriers. The field dependent photocurrent $J_{ph}(V)$, which results from an improved extraction of carriers with increasing electric field, is shifted by the constant diffusive photocurrent $J_{ph}(V_{pos})$.

Limpinsel *et al.* also studied the photocurrent in P3HT:PCBM solar cells and made very similar observations, but presented an alternative explanation.[6] Limpinsel *et al.* agree that the $J_{ph}-V$ curve consists of a voltage independent $J_{ph}(V_{pos})$ and a voltage dependent $J_{ph}(V)$ component. However, Limpinsel *et al.* do not agree on the origin of the POS and of the voltage independent photocurrent component of the $J_{ph}-V$ curves. They consider that at the POS (V_{pos}) the solar cell is not at flat band condition but rather at a quasi-flat-band condition, well below V_{bi}.[6] At the POS the bands are flat in the bulk, but close to the electrodes the valence and conduction bands in the organic layer bend due to the Ohmic nature of the contacts. Hence, in the region close to the contact, where the bands bend, a net electric field exists, which according to Limpinsel *et al.*, drives the extraction of photogenerated carriers and therefore contributes to a net voltage independent photocurrent $J_{ph}(V_{pos})$.[6] Hence, band bending close to the electrodes would contribute to voltage independent photocurrent that shifts the field dependent photocurrent contribution to negative values.

Dibb *et al.* have analyzed the relationship between the linearity of the light-intensity dependence of J_{ph} and the recombination mechanism in organic solar cells.[7]

They demonstrated that it is possible for a cell to exhibit a J_{ph} linear with illumination intensity even if the underlying recombination process that shapes the $J(V)$ curve is nonlinear.[7] Very recently, Petersen *et al.* studied the charge extraction and photocurrent in organic bulk heterojunction solar cells using a numerical drift-diffusion model to investigate the effects of injection barriers, selective contacts, different recombination mechanisms, and series resistance on $J_{ph}(V)$.[8] The modeling results of Petersen *et al.*[8] are qualitatively consistent with experimental observations of Ooi *et al.*[5] and Limpinsel *et al.*[6] and explain the effects by position dependent equilibrium concentrations and lifetimes of the charge carriers.

Importantly, however, Street *et al.* showed analytically and experimentally that the series resistance in the solar cell's circuit reduces the photocurrent in forward bias.[9] This has significant implications for the interpretation of the $J_{ph}-V$ of data presented by Ooi *et al.*[5] and Limpinsel *et al* [6] because these authors did not correct the measured photocurrent for the series resistance of the electrodes. Consequently, the externally applied voltage deviates from the effective bias, especially in forward bias. Because the photocurrent as a function of effective voltage on the active layer is of physical relevance in understanding the field dependence of the collection of photogenerated charges, the relevance of the results described so far is ambiguous. Furthermore, in interpreting the voltage dependence of J_{ph} the possible effect of injected charge carriers has largely been neglected.[5,6] These two considerations warrant a more detailed study of photocurrents in polymer solar cells.

Therefore, in the present chapter, we study experimentally and numerically the photocurrent as a function of effective voltage in polymer:fullerene bulk heterojunction devices. We name this the internal photocurrent. The experimental $J_{ph}-V$ curves are measured with a pulsed light source setup to minimize the heating effect of the substrate. We take care to correct the experimental $J_{ph}-V$ curve for the effect of the electrodes' series resistances and determine the internal $J_{ph}-V$ curve as a function of the effective applied voltage (V_{eff}). We study the internal photocurrent for solar cells based on PDPPTPT (poly[{2,5-bis(2-hexyldecyl)-2,3,5,6-tetrahydro-3,6-dioxopyrrolo[3,4-c]pyrrole-1,4-diyl}-*alt*-{[2,2'-(1,4-phenylene)bithiophene]-5,5'-diyl}]) with PCBM. PDPPTPT is a small band gap polymer that provides a power conversion efficiency of 4.6% in solar cells with PCBM.[10] We show that the internal photocurrent determined on PDPPTPT:PCBM devices is much larger in forward bias than the external photocurrent. For devices with low injection current, a rather symmetric $J_{ph}-V$ curve around $J_{ph} = 0$ is observed. No voltage independent negative photocurrent offset is observed in the internal $J_{ph}-V$ curve for any of the devices.

We further employ numerical simulations in a drift-diffusion model,[11] similar to Petersen *et al.*,[8] to study the internal photocurrent in forward and reverse bias. In the numerical simulations, the effects of bimolecular recombination, injecting contact, and band bending on the $J_{ph}-V$ curve are considered. The simulations show that the $J_{ph}-V$ curves strongly dependent on the bimolecular recombination rate. In forward bias, the photocurrent is reduced for Langevin type recombination. When the recombination rate is increased (reduced) the photocurrent reduces (increases) in forward bias. This reduction of the photocurrent in forward bias can be related to an increased recombination between photogenerated carries and injected carriers. The simulations shows that neither self-selective nor band bending is needed to observe $J_{ph}-V$ curves which are asymmetric around $J_{ph} = 0$.

3.2 Experiment

PDPPTPT:PCBM (1:2 by weight) devices were prepared by first spin casting a 50 nm thick PEDOT:PSS (Clevios P, VP Al4083, Heraeus) onto pre-cleaned glass substrate covered with patterned indium tin oxide (ITO, 14 Ω/sq), followed by spin casting a 100 nm thick PDPPTPT:PCBM layer from chloroform containing 25 mg/mL 1,8-diiodooctane.[10] As back electrodes PEDOT:PSS/Ag, Ag, and LiF/Al were used. For the PEDOT:PSS/Ag device, PEDOT:PSS (Clevios F CPP105D, Heraeus) diluted with 30% v/v of isopropanol was spin coated on the PDPPTPT:PCBM layer. The PEDOT:PSS top contact device was masked to avoid spurious photocurrent from areas outside the device area defined by the overlap of the two electrodes, caused by the high lateral conductivity of the Clevios F CPP105D PEDOT:PSS. Ag (100 nm), LiF (1 nm), and Al (100 nm) were thermally evaporated in a vacuum of 10^{-7} mbar. The active layer thicknesses of all the devices are determined with a Veeco Dektak 150 Surface Profiler and are ~100 nm. $J-V$ characteristics are measured with a Keithley 2400 source meter under illumination with a tungsten-halogen lamp with a Schott GG385 UV filter and a Hoya LB120 daylight filter at 100 mW/cm^2 light intensity. To measure photocurrents and minimize the heating of the sample under illumination we use a solid state laser (B&W Tek Inc. 532 nm, 30 mW) and a mechanical chopper (Stanford Research SR 540 chopper, f = 175 Hz) to produce a square wave modulated illumination source. The device is connected in series to a 2.5 Ohm probe resistor and voltage source. The probe resistor is connected in parallel to the input of a lock-in amplifier (Stanford Research Systems SR830) and the amplitude of the recorded signal is proportional to the photocurrent.

3.3 Results and discussion

3.3.1 Photocurrent in PDPPTPT:PCBM devices

To investigate $J_{ph}-V$ curves experimentally and study the effect of injected carriers on the J_{ph}, PDPPTPT:PCBM blends were used as active layer in three glass/ITO/PEDOT:PSS/PDPTPT:PCBM devices with three different top contacts: LiF/Al, Ag, and PEDOT:PSS/Ag. The $J-V$ characteristics of these three devices, recorded under 100 mW/cm^2 while light illumination, are shown in Figure 3.1(a). The device with the LiF/Al top contact shows the typical performance of a PDPTPT:PCBM solar cell with a short circuit current J_{sc} = 10.56 mA/cm^2, an open circuit voltage V_{oc} = 0.79 V, and a fill factor FF = 0.58, providing a power conversion efficiency of η = 4.8%. For the Ag and PEDOT:PSS/Ag different top electrodes, the devices show lower performances due to the reduced V_{oc}'s of 0.74 V and 0.27 V, respectively. The reduction of V_{oc} for the Ag and PEDOT:PSS/Ag top contact devices with respect to the solar cell is due to the different effective work function of Ag and PEDOT:PSS. As can be seen from the $J-V$ characteristics measured under illumination the current quickly saturates in reverse bias at similar values indicating identical transport and generation of free charge carriers in the bulk for the three devices in reverse bias. The slight changes in magnitudes of illumination current in reverse bias can be related to optical processes. Different top electrodes can result in different optical interference in the stack and consequently in a difference in absorption across the layer. The illumination current of the PEDOT:PSS/Ag device is symmetric around J_{ph} = 0 and saturates in reverse and forward bias at similar values.

The dark $J-V$ curves clearly show the effect of the top electrodes on the dark currents J_{dark} (Figure 3.1(b)). For the LiF/Al top electrode the dark current is large in forward bias at +2 V bias, for the Ag electrode the dark current is about five times lower, while for the PEDOT:PSS/Ag device the injection current is strongly suppressed. The magnitude is related to the injecting properties of the top electrodes. The LiF/Al top electrode forms an Ohmic contact with the PCBM acceptor, which has a LUMO energy at −4.2 eV. Ag has a higher work function than LiF/Al and creates an electron injection barrier that reduces the dark current. PEDOT:PSS/Ag has the highest work function and electrons cannot be injected such that the dark current is strongly suppressed. The low dark current for the ITO/PEDOT:PSS/PDPPTPT:PCBM/PEDOT:PSS/Ag device demonstrates that at both PEDOT:PSS contacts large hole and electron injection barriers are present. It also implies that for the LiF/Al and Ag devices the dark current is electron dominated. The energy difference between the HOMO of PDPPTPT (−5.5 eV)[10]

and the work function of PEDOT:PSS (−5.1 eV) indeed suggests a barrier of ~0.4 eV for hole injection.

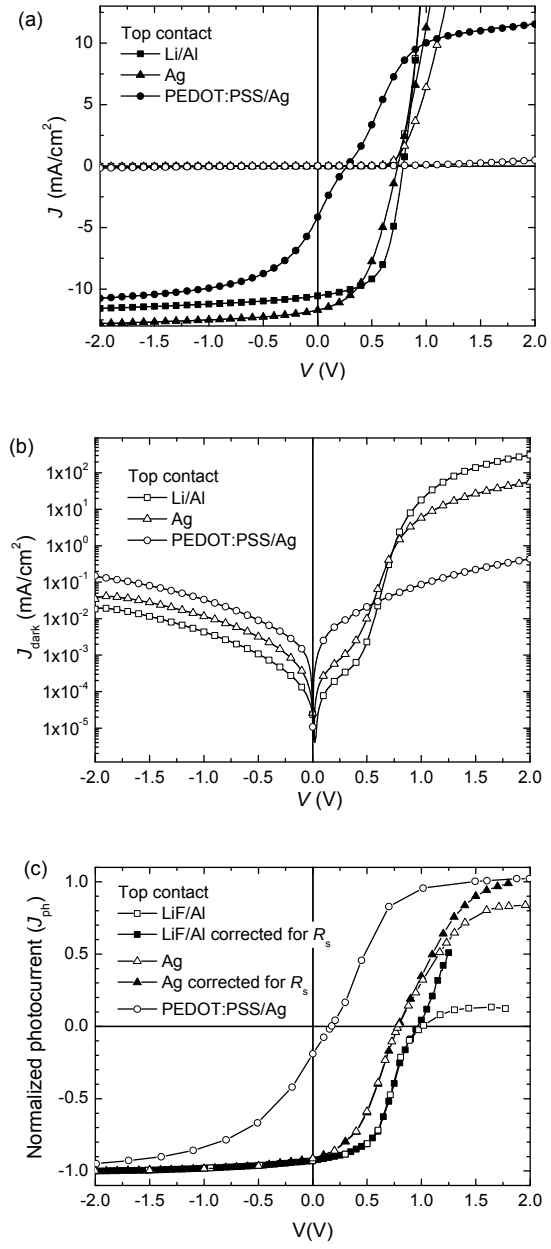

Figure 3.1: $J-V$ characteristics of ITO/PEDOT:PSS/PDPPTPT:PCBM devices with LiF/Al, Ag, and PEDOT:PSS/Ag top contacts. (a) In the dark (open symbols) and under 100 mW cm^{-2} continuous white light illumination (solid symbols). (b) Semi-logarithmic plot of the dark currents. (c) $J_{ph}-V$ characteristics measured with modulated light before (open symbols) and after series resistance correction (closed symbols) normalized to the maximum photocurrent at reverse bias (*i.e.* −2 V for LiF/Al and Ag; −4 V for PEDOT:PSS/Ag).

From the V_{oc} (0.27 V) of the PEDOT:PSS/Ag device, we infer that at that electrode the injection barrier for holes will be larger by the same amount and is about 0.7 V. The large illumination currents in reverse and forward bias for the PEDOT:PSS/Ag device demonstrate that photogenerated carriers can be effectively collected at the PEDOT:PSS electrodes. From the efficient collection of photogenerated carriers in forward and reverse bias and from the estimated injection barriers, electrodes blocking the collection of carriers from the active layer can be excluded. The suppressed dark currents are solely due to injection barriers from the electrode to the active layer.

Since the dark current is very low in the PEDOT:PSS/Ag top contact device, the illumination current (J_{light}) is equal to the photocurrent (J_{ph}). The shape of the $J_{ph} - V$ curve for the PEDOT:PSS/Ag top contact device corresponds to the idealized photocurrent that follows from the drift-diffusion model of Sokel and Hughes.[12] In reverse and forward bias all the photogenerated carriers are collected because the electric field is large enough and the photocurrent is only limited by the generation rate of free carriers (G).

Closer to V_{oc}, the electric field decreases and diffusion of carriers starts to compete with the drift of carriers. Because photogenerated carriers diffuse isotropically out of the device, the diffusion current will not contribute to the net photocurrent close to V_{oc} and the photocurrent J_{ph} is reduced. At the compensation voltage (V_0) the photocurrent cancels ($J_{ph} = 0$), because the electric field in the device is minimal and consequently carriers either diffuse out of the device or recombine between each other.

For the LiF/Al and the Ag top contact devices the illumination current consist mainly of photocurrent below V_{oc} and close to V_{oc} the photocurrent is low for the same reason as for the PEDOT:PSS/Ag device (diffusion and recombination). At high reverse bias the illumination current saturates since all the photogenerated carriers are collected ($J_{ph} = qGL$, with q the elementary charge and L the thickness). In forward bias above V_{oc} the illumination current consists of photogenerated and injected carriers. With increasing bias, the illumination current becomes quickly dominated by the injected carriers. As already mentioned by Ooi *et al.*,[5] the photocurrent cannot be reliably determined with a standard setup because the substrate and photoactive layers heat up under illumination. In such case the photocurrent would be overestimated because under illumination and higher temperature the injected carriers have an increased mobility compared to the dark. To determine the photocurrent in forward bias accurately and minimize heating effects, we measured the PDPPTPT:PCBM devices with the pulsed setup described in the experimental.

Figure 3.1(c) shows $J_{ph}-V$ curves normalized to the maximum reverse photocurrent of the three PDPPTPT:PCBM devices measured with the pulsed light source. The photocurrent of the PEDOT:PSS/Ag device is nearly symmetric around J_{ph} = 0 and saturates in forward bias and reverse bias at the same maximum photocurrent that was measured with the continuous illumination setup. For the LiF/Al and Ag devices, the photocurrent is reduced in forward bias. This reduction is more pronounced for the LiF/Al electrode where the dark current is larger.

Similar to Ooi *et al.*[5] and Limpinsel *et al.*,[2] we can identify the hypothesized "point of optimal symmetry" (POS) in the $J_{ph}-V$ curves and then decompose the curves into a bias-symmetric voltage dependent photocurrent and a constant a voltage independent photocurrent offset. An alternative view, recently proposed by Petersen *et al.*,[8] is that the photocurrent in forward bias is reduced by the injected carriers, *e.g.* when these recombine with photogenerated carriers, This view is supported by the correlation between a high dark current and a high reduction of J_{ph} (Figure 3.1(b) and Figure 3.1(c)).

However, it is important to note that for the measured $J_{ph}-V$ curves the resistance of the electrode (mainly the ITO electrode) and the resulting voltage drop over the electrodes when current flows through the device has been neglected so far. According to Street *et al.*,[9] the series resistance of the solar cell circuit can lead to a reduced photocurrent in forward bias. To correctly interpret the photocurrent curves it is important to determine the photocurrent versus the effective applied voltage (V_{eff}) on the active layer. This is justified since the transport, collection, and recombination of generated carriers is governed by the electric field across the active layer and the electric field scales with the effective (internal) voltage. To correct for the voltage drops over the electrodes and determine the J_{ph} as a function of the effective voltage we first calculate the illumination current (I_{light}) by adding the photocurrent and the dark current ($I_{light} = I_{dark}+I_{ph}$). Then, using $V = R_s I$, the effective voltage is determined for the dark and illumination currents knowing the series resistance of the device (R_s = 24 Ω): $V_{eff} = V_{appl} - R_s I_{light/dark}$. The $I-V$ curves in dark and under illumination versus effective voltage are then given by:

$$\begin{aligned} I_{dark}(V_{eff}) &= I_{dark}(V_{appl} - I_{dark}(V_{appl})R_s) \\ I_{light}(V_{eff}) &= I_{light}(V_{appl} - I_{light}(V_{appl})R_s) \end{aligned} \tag{3.1}$$

The photocurrent density is then calculated by:

$$J_{ph}(V_{eff}) = \left(I_{light}(V_{eff}) - I_{dark}(V_{eff})\right) / A \tag{3.2}$$

with A the area of the illumination spot. The corrected $J_{ph}-V$ curves are shown in Figure 3.1(c) for the LiF/Al and Ag devices. For the PEDOT:PSS/Ag device, no correction is needed since the dark current is very low and the $J_{ph}-V$ curve does not change after corrections. The corrected $J_{ph}-V$ curve and the measured $J_{ph}-V$ curve superimpose in the voltage range from −2 V to V_{oc} for the LiF/Al and Ag devices. In the voltage range above V_{oc} the corrected J_{ph} is somewhat larger than the non corrected J_{ph} for the Ag device and significant larger for the LiF/Al device.

The increase of the corrected photocurrent with respect to the non-corrected photocurrent in forward bias (Figure 3.1(c)) is due to the difference in voltage drop in dark and under illumination over the electrodes. Under illumination, the current is larger at the same applied voltage than in the dark and therefore causes a larger voltage drop over the electrodes than in the dark. Consequently, the external illumination current measured at the same applied voltage as the dark current has a lower effective (internal) voltage V_{eff} than the dark current. This will yield a larger reconstructed internal photocurrent.

After correction the $J_{ph}-V$ curve of the Ag top contact device is symmetric around V_{eff} = 0.75 V and seems to saturate in forward bias. We cannot fully exclude an increase of the photocurrent beyond the saturation current above V_{eff} = 1.8 V because it was difficult to measure the Ag top contact device in a larger effective voltage range because at higher current the device degrades due to switching effects.

For the LiF/Al top contact device, the internal photocurrent is much larger than the externally measured photocurrent. At V_{eff} = 1.25 V, J_{ph} has reached half of the reverse saturation current. Because the LiF/Al device does not remain stable at high current densities it was not possible to measure the internal J_{ph} beyond V_{eff} = 1.25 V. Hence, it was not possible to determine where the photocurrent saturates. From the shape of the corrected $J_{ph}-V$ curve of the LiF/Al device, three scenarios are possible: *i*) the photocurrent saturates at maximum photocurrent and is symmetric around the compensation voltage V_0 (close to V_{oc}), similar to the PEDOT:PSS/Ag and Ag devices; *ii*) the photocurrent saturates in forward bias, with J_{ph} reaching a value of 0.5 – 1 times the saturation current in reverse; or *iii*) the photocurrent does not saturate and is larger in forward bias than the reverse bias due to a photomultiplication effect.

From these results it is clear that the strong reduction of the forward photocurrent and the significant offset of the field dependent photocurrent due to a constant photocurrent contribution as described by Ooi *et al.*[5] and Limpinsel *et al.*[6] are not observed for any of the PDPPTPT:PCBM devices, after correcting for the effect of the series resistance R_s.

Furthermore, because the magnitude of the dark current of the PDPPTPT:PCBM LiF/Al device is typical for polymer:fullerene solar cells and since the internal photocurrent in forward bias strongly increases with respect to the external photocurrent after correction for the series resistance, it is essential to include this correction when measuring photocurrents in organic solar cell above the V_{oc}.

Concluding, after making appropriate corrections, we do not observe a strong influence of injected carriers on current on the photocurrent $J_{ph}-V$ curves of PDPPTPT:PCBM devices. We also did not observe a POS below $J_{ph} = 0$. The measurements indicate rather symmetric $J_{ph}-V$ curves around V_0. To better understand how the $J_{ph}-V$ curves can be affected by the injected charges, we performed numerical simulations, which are described in the section below.

3.3.2 Photocurrent simulations

To study the internal photocurrent and investigate how the shape of the internal photocurrent $J_{ph}-V$ curve is affected by bimolecular recombination, injecting electrodes, and band bending, we use numerical drift-diffusion simulation. The numerical method is described in detail elsewhere.[11] The numerical program considers diffusion and drift of free carriers in one dimension. Also, space charge effects are included. The active layer of the solar cell is considered under the effective medium approach meaning that electrons and holes are transported in the same phase. For sake of simplicity, we do not investigate the influence of disorder and field dependent geminate recombination. Therefore, we use in the simulations constant carrier mobilities independent of electric field and carrier density and the generation rate (G) of free carriers under illumination is considered constant, independent on the electric field and position in the device.

In the simulations a layer thickness of 100 nm is assumed. The relevant energy difference between the HOMO level of the donor and of the LUMO level of the acceptor is the effective band gap, assumed to be $E_g = 1$ eV in the simulations. In the simulations we consider electrodes without and with (0.5 eV) barriers for carrier injection from the electrodes (Figure 3.2(a)). Specifically we consider three different configurations (two non-injecting contacts, two Ohmic contacts, and one non-injecting and one Ohmic contact).

Recombination between free carriers is considered by a Langevin type recombination rate equation[13]:

$$R = \gamma_{pre} \frac{q(\mu_n + \mu_p)}{\varepsilon_0 \varepsilon_r} \left(np - n_i^2 \right) \tag{3.3}$$

where γ_{pre} is a Langevin pre-factor, q elementary charge, μ_n and μ_p the electron and hole mobility, ε_0 the dielectric permittivity of vacuum, ε_r the relative permittivity, n and p the electron and hole density, and n_i the intrinsic carrier density. The photocurrent density J_{ph} is obtained by taking the difference between the simulated $J-V$ curve in the dark and under illumination. The calculated $J_{ph}-V$ curves are normalized by the maximum photocurrent given by the generation rate of charge carriers qGL. First we describe the effect of different injecting contacts and bimolecular Langevin recombination (γ_{pre} = 1), following an approach similar to Petersen *et al.*[8] Three device configurations are compared: *i*) with two non-injecting contacts, *ii*) with one Ohmic hole injecting contact, and *iii*) with Ohmic electron and hole injecting contact (Figure 3.2(a)). The simulated $J_{ph}-V$ curves for these devices for γ_{pre} = 1, $\mu_n = \mu_p = 10^{-8}$ m^2/Vs, E_g = 1 eV, $G = 2.7 \times 10^{27}$ m^{-3}s^{-1} are shown in Figure 3.2(b).

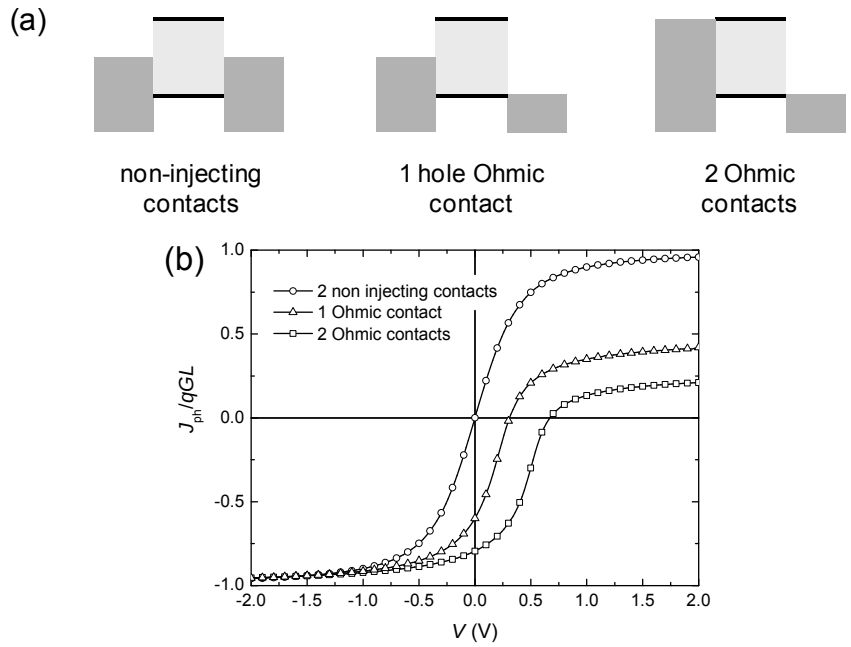

Figure 3.2: (a) Schematic band diagram of the simulated devices: non-injecting contacts, a device with one Ohmic contact for holes, and a device with Ohmic electron and hole contacts. Effective band gap is E_g = 1 eV; injection barriers are either 0 or 0.5 eV. (b) Simulated $J_{ph}-V$ characteristics normalized to the maximum photocurrent qGL of the three devices shown in panel a. Layer thickness L = 100 nm, equal hole and $\mu_n = \mu_p = 10^{-8}$ m^2/Vs, effective band gap E_g = 1 eV, $G = 2.7 \times 10^{27}$ m^{-3}s^{-1} and Langevin pre-factor γ_{pre} = 1 are used in the simulations.

For the device with non-injecting contacts, a symmetric $J_{ph}-V$ curve around V = 0 V is obtained which saturates in forward and reverse bias.[12] The symmetric $J_{ph}-V$ curve is expected because of the symmetric contacts and a similar result has recently been described in Ref. [8]. The exact shape of the $J_{ph}-V$ curve will depend

on the transport, extraction, and bimolecular recombination of photogenerated carriers.[12] At high reverse or forward bias, all the photogenerated carriers are collected by the electrodes and the photocurrent is limited only by the generation rate and reaches the maximum photocurrent *qGL*. When the voltage is decreased from negative or positive bias to 0 V, the photocurrent decreases in magnitude. This is related to a decrease of the electric field across the device which reduces field assisted collection of carriers (drift) and to diffusion starting to compete with drift. At 0 V, the photocurrent is canceled because electric field is extremely low and generated carriers either diffuse isotropically out of the device or recombine bimolecularly.

When one injecting hole contact is introduced the $J_{ph}-V$ curves shifts to the right and J_{ph} cancels at 0.31 V. This is because the built-in voltage increases when the work function of the electrodes are different. In forward bias above 0.31 V, the photocurrent is strongly reduced with respect to the generation rate *qGL* and saturates at 2 V around $0.4\times qGL$. When two Ohmic contacts are used, the J_{ph} cancels at 0.65 V and in forward bias J_{ph} is further reduced with respect to *qGL*, saturating at about $0.2\times qGL$.

The dark current in the simulations of the device with two injecting Ohmic contacts is larger than the dark current of the device with only one hole injecting contact (not shown here). This is because the device becomes bipolar and the presence of both injected electrons and holes reduces the net space at the injection contact. Consequently more electrons and holes can be injected into the device.[14,15] The higher concentration of injected charge carriers apparently reduces the photocurrent due to bimolecular recombination with photogenerated carriers (also see Ref. [8]). Note that *R* scales with *np* (Equation (3.3)).

For devices with Ohmic contacts, we observe an asymmetric $J_{ph}-V$ curve in which one can identify a POS at negative J_{ph}. In calculating this curve, Ohmic contacts have been used and, consequently, self-selective contacts are not needed to observe a POS as proposed by Ooi *et al.*[5] This conclusion was also obtained by Petersen *et al.*[8] Comparing the simulated photocurrent curves (Figure 3.2(b)) for devices with injecting contacts with the experimental $J_{ph}-V$ curves of the PDPPTPT:PCBM devices with Ag and LiF/Al top contacts (Figure 3.1(c)), the photocurrent in the experiment is much larger in forward bias compared with the simulated curves. This could be related to a reduced recombination rate in the PDPPTPT:PCBM blend.

To further investigate the influence of the bimolecular recombination rate on the photocurrent, we perform simulations on the device with two Ohmic contacts and vary the recombination rate via the Langevin pre-factor. Figure 3.3(a) depicts the normalized $J_{ph}-V$ curves for different Langevin pre-factors γ_{pre}. In reverse bias below

V_0, the photocurrent decreases with increasing γ_{pre}. This is related to bimolecular recombination between photogenerated carriers (no carriers are injected in reverse bias). Increasing the recombination rate by increasing γ_{pre} decreases the fill factor (Figure 3.3(a), below V_0). In forward bias above V_0, the trend of the reduction of the photocurrent with Langevin pre-factor is more pronounced. At $\gamma_{pre} = 10$ the photocurrent almost cancels, but when γ_{pre} decreases the photocurrent increases in forward bias and the $J_{ph}-V$ curve becomes more symmetric. The effect of lowering the bimolecular recombination, by setting $\gamma_{pre} < 0.1$ will be discussed in Chapter 4.

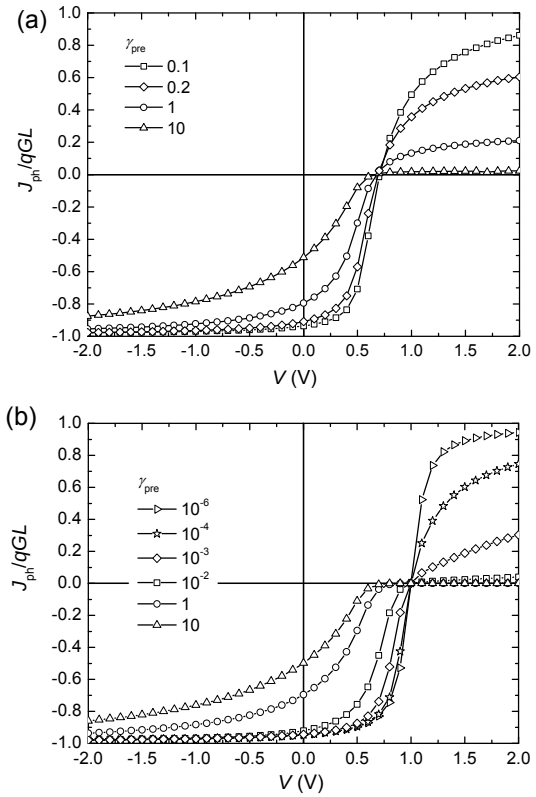

Figure 3.3: (a) Simulated $J_{ph}-V$ curves normalized to the maximum photocurrent qGL for various Langevin pre-factors γ_{pre}. L = 100 nm, $\mu_n = \mu_p = 10^{-8}$ m^2/Vs, E_g = 1 eV, $G = 2.7 \times 10^{27}$ m^{-3}s^{-1}, and two Ohmic contacts were used in the simulations. (b) Same as (a) but without band bending.

The stronger response of the photocurrent to the Langevin pre-factor γ_{pre} in forward bias clearly evidences that the photocurrent is reduced by bimolecular reduction between photogenerated carriers and injected carriers. In forward bias, the carrier density in the dark and under illumination is a few orders of magnitudes larger than in reverse bias due to injection of carriers. Hence, many photogenerated carriers will recombine with injected carriers and the recombination rate (of photogenerated carriers) is limited by the injected carriers. Consequently, a modification of the recombination rate via the Langevin pre-factor has a strong effect in forward bias.

In reverse bias, photogenerated carriers only recombine amongst each other and the recombination rate is lower because it is limited by the density of photogenerated carriers, and the effect of a change in γ_{pre} is smaller.

Limpinsel *et al.*[6] proposed that band banding has a strong influence on the $J_{ph}-V$ curve and is the reason for the POS. Simulated $J_{ph}-V$ curves, in absence of band bending (obtained by keeping $\varphi(x) = xV/L$ via switching off the routine that solves the Poisson equation, $\nabla^2\varphi(x) = q\big(n(x) - p(x)\big)/\varepsilon_0\varepsilon_r$, in the simulations) are shown in Figure 3.3(b). Comparison with Figure 3.3(a), shows that the photocurrent is much more reduced in forward bias for a given γ_{pre} when there is no band bending (Figure 3.3(b)) than with band bending (Figure 3.3(a)). Clearly, Figures 3.3(a) and 3.3(b) show that the photocurrent curves are reduced due to bimolecular recombination and band bending is not needed to explain this reduction. We note that band bending is necessary to explain that the voltage at the POS is smaller than the build-in potential (compare Figure 3.3(a) and Figure 3.3(b)), as discussed in detail by Petersen et al.[8]

Summarizing, the photocurrent simulations show that the bimolecular recombination of photogenerated charge carriers with injected charge carriers can cause a significant decrease of the photocurrent in forward bias. The same conclusion was recently obtained by Petersen *et al.*.[8] The decrease is strongly modulated by the extent to which bimolecular recombination occurs. In the simulations we assumed Langevin recombination of electrons and holes and adjusted the rate, using a variable pre-factor γ_{pre} (Equation (3.3)). The simulations clearly show that to explain a reduction in forward bias it is not necessary to assume charge-selective contacts as suggested by Ooi *et al.*.[5] Likewise, the explanation offered by Limpinsel et al.[6] that the reduction of the forward photocurrent is due to band bending effects near the electrode, seems not correct because under conditions were band bending was excluded, the reduction of photocurrent in forward is even higher that when incorporating band bending.

3.3.3 Forward photocurrent model

The effects of reduced photocurrent under forward bias as a result of recombination with injected charge carriers that emerge from the simulations (Figure 3.3) can be rationalized with a simple analytical model. For that we first consider the situation of a device with a single Ohmic contact that injects holes under forward bias and assume that the charge carrier mobilities for electron and holes are equal ($\mu = \mu_n = \mu_p$). Under continuous illumination the rate equation for photogenerated electrons (n_{ph}) reaches steady state, *i.e.*:

$$\frac{dn_{\mathrm{ph}}}{dt} = G - R - \frac{n_{\mathrm{ph}}}{\tau} = 0 \tag{3.4}$$

with τ the lifetime of the photogenerated electrons. In high forward bias the density of injected holes (p_{inj}) will largely exceed the density of photogenerated holes (p_{ph}) such that the Langevin recombination rate can be expressed as:

$$R = \gamma_{\mathrm{pre}} \frac{2q\mu}{\varepsilon_0 \varepsilon_{\mathrm{r}}} n_{\mathrm{ph}} p_{\mathrm{inj}} \tag{3.5}$$

In high forward bias we further consider that drift dominates diffusion of charges such that the lifetime of the photogenerated electrons is determined by their average drift time τ_{drift}. Neglecting space charge effects, the electric field equals V/L and since, on average, photogenerated electrons need to traverse only half of the active layer in order to reach an electrode, the lifetime is given by:[16]

$$\frac{1}{\tau} = \frac{1}{\tau_{\mathrm{drift}}} = 2\frac{\mu V}{L^2} \tag{3.6}$$

such that the photocurrent density, which is the extraction rate of photogenerated charges equals:

$$J_{\mathrm{ph}} = \frac{q n_{\mathrm{ph}} L}{\tau_{\mathrm{drift}}} \tag{3.7}$$

To determine the density of injected holes (p_{inj}) in high forward bias, we consider the injected current to be space charge limited, such that the average density of injected holes can be expressed as:[17]

$$\bar{p}_{\mathrm{inj}} = \frac{3}{2}\frac{\varepsilon_0 \varepsilon_{\mathrm{r}}}{q}\frac{V}{L^2} \quad . \tag{3.8}$$

Combining (4) − (8) results in a remarkably simple expression for the photocurrent under high forward bias:

$$J_{\mathrm{ph}} = \frac{qGL}{1 + \frac{3}{2}\gamma_{pre}} \tag{3.9}$$

Figure 3.4(a) shows the simulated photocurrent for the device under consideration, *i.e.* having one injecting contact. For a device with unmodified Langevin recombination ($\gamma_{pre} = 1$), J_{ph}/qGL equals 0.46 at $V = +5$ V, close to the value of 0.40 expected from Equation (3.9). Also for other values of γ_{pre} the Equation (3.9) yields results in good agreement with obtained in the simulations (Figure 3.4(b)).

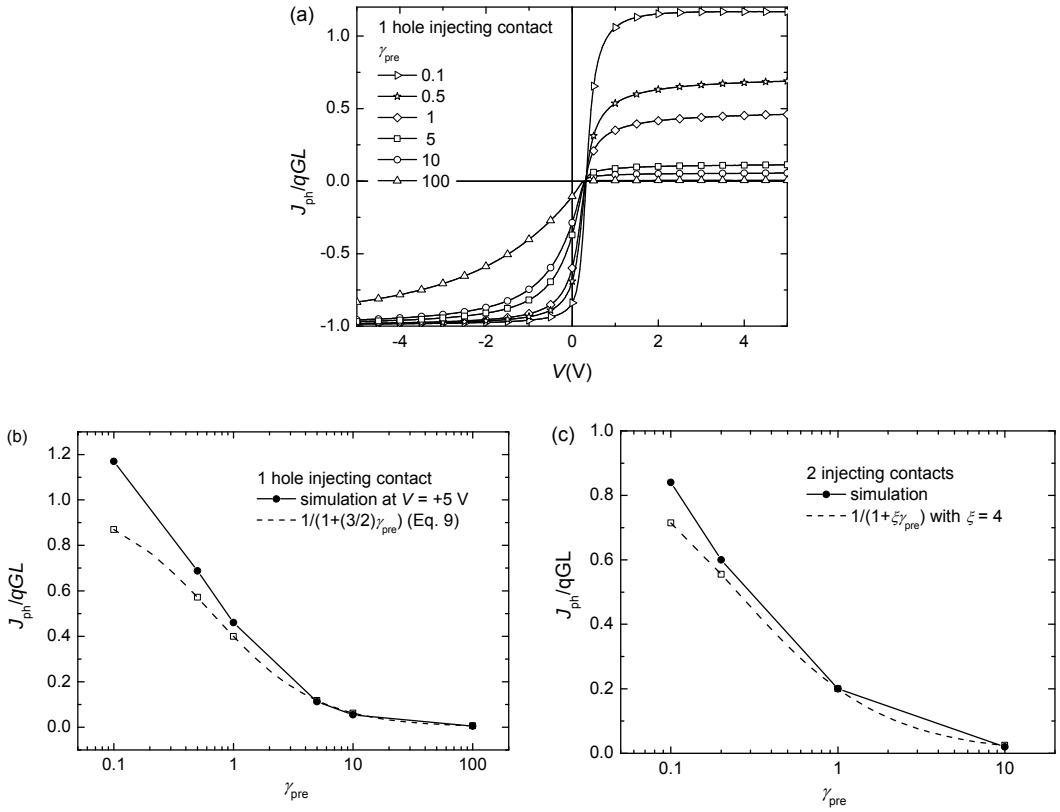

Figure 3.4: (a) Simulated J_{ph}–V characteristics normalized to the maximum photocurrent qGL of a device with one hole injecting contact, L = 100 nm, $\mu_n = \mu_p = 10^{-8}$ m^2 /Vs, E_g = 1 eV, and $G = 2.7 \times 10^{27}$ m^{-3}s^{-1} for different Langevin pre-factors γ_{pre}. (b) Comparison of J_{ph}/qGL at +5 V as obtained from the simulations as shown in panel (a) and the value predicted from. Equation 3.9 (c) Comparison of J_{ph}/qGL at +5 V obtained from the simulations for two injecting contacts and the value predicted from. Equation (3.10) using $\xi = 4$.

For a device that has two instead of one injecting contact, *i.e.* injection of both electrons and holes, the situation changes. As a result of space charge neutralization, more carriers will be injected than expected on basis of Equation (3.8).[15] This increased carrier concentration leads to an enhanced Langevin recombination rate, which reduces J_{ph}. By including an adjustable pre-factor ξ to account for this effect, the photocurrent under high forward bias can be expressed as:

$$J_{\mathrm{ph}} = \frac{qGL}{1+\xi\gamma_{pre}} \tag{3.10}$$

Figure 3.4(c) shows the simulated J_{ph}/qGL at V = +2 V for a device with electron and hole injecting contacts and the result of Equation (3.10) for ξ = 4. Given the crudeness of the approach, the correspondence is rather good and shows that the analysis captures the essential physics correctly.

3.4 Conclusions

We have studied the photocurrent in polymer solar cells devices under forward and reverse bias experimentally and by performing device simulations using a drift-diffusion model. In the literature examples of reduced photocurrents in forward bias have been reported.[5,6] We show that these observations are likely significantly, and at least in part, obscured by the fact that in forward bias the effective voltage over the solar cells is much less than the applied voltage, because of a non-negligible series resistance in the electrodes. After correcting for this effect we were not able to find experimental confirmation for reduced photocurrents in forward bias for efficient PDPPTPT:PCBM and, pristine and thermally annealed P3HT:PCBM solar cells.

Drift-diffusion simulations have been used to identify the conditions under which reduced photocurrents in forward bias may occur. In accordance with recent results by Petersen *et al,*[8] we find that prime cause for a reduced photocurrent in forward bias is bimolecular, Langevin type, recombination of photogenerated and injected electron and holes carriers. Under conditions where Langevin recombination is effective, the forward photocurrent is small. Neither charge-selective contacts[5] nor band bending[6] are needed to explain a reduced forward photocurrent. The latter actually, works in the opposite direction because it reduces charge injection. A simple analytical model shows that under high forward bias the photocurrent (J_{ph}) relative to the generation rate (qGL) can be expressed as $J_{\mathrm{ph}}/\mathrm{q}GL = (1+\xi\gamma_{\mathrm{pre}})^{-1}$, with γ_{pre} the Langevin pre-factor and ξ a positive constant.

Summarizing, forward photocurrents in polymer solar cell devices are largely affected by injected charge carriers. A reduced forward photocurrent is expected when photogenerated carriers can effectively recombine with injected charges, see also Ref. [8]. When the contacts to the device are non-injecting, the photocurrent is symmetric around the compensation voltage and maximized by the generation rate.

3.5 References

[1] C. Brabec, U. Scherf, V. Dyakonov, Vladimir (eds.), Organic Photovoltaics: Materials, Device Physics, and Manufacturing Technologies, Wiley-VCH, Weinheim (2008).

[2] D. Veldman, S. C. J. Meskers, R. A. J. Janssen, *Adv. Funct. Mater.* **2009**, *19*, 1939.

[3] K. Vandewal, K. Tvingstedt, A. Gadisa, O. Inganäs, J. V. Manca, *Nat. Mater.* **2009**, *8*, 904.

[4] V. D. Mihailetchi, P. W. M. Blom, J. C. Hummelen, M. T. Rispens, *J. Appl. Phys*. **2003**, *94*, 6849.

[5] Z. E. Ooi, R. Jin, J. Huang, Y. F. Loo, A. Sellinger, J. C. deMello, *J. Mater. Chem.* **2008**, *18*, 1644.

[6] M. Limpinsel, A. Wagenpfahl, M. Mingebach, C. Deibel, V. Dyakonov, *Phys. Rev. B* **2010**, *81*, 085203.

[7] G. F. A. Dibb, T. Kirchartz, D. Credgington, J. R. Durrant, J. Nelson, J. Phys. *Chem. Lett.* **2011**, *2*, 2407.

[8] A. Petersen, T. Kirchartz, T. A. Wagner, *Phys. Rev. B.* **2012**, *85*, 045208.

[9] R. A. Street, K. W. Song, S. Cowan, *Org. Electron.* **2011**, *12*, 244.

[10] J. C. Bijleveld, V. S. Gevaerts, D. Di Nuzzo, M. Turbiez, S. G. J. Mathijssen, D. M. de Leeuw, M. M. Wienk, R. A. J. Janssen, *Adv. Mater.* **2010**, *22*, E242.

[11] L. J. A. Koster, E. C. P. Smits, V. D. Mihailetchi, P. W. M. Blom, *Phys. Rev. B* **2005**, *72*, 085205.

[12] R. Sokel, R. C. Hughes, *J. Appl. Phys.* **1982**, *53*, 7414.

[13] P. Langevin, *Ann. Chim. Phys.* VII **1903**, *28*, 433.

[14] R. H. Parmenter, W. Ruppel, *J. Appl. Phys.* **1959**, *30*, 1548.

[15] L. M. Rosenberg, M. A. Lampert, *J. Appl. Phys.* **1970**, *41*, 508.

[16] L. J. A. Koster, M. Kemerink, M. M. Wienk, K. Maturová, R. A. J. Janssen, *Adv. Mater.* **2011**, *23*, 1670.

[17] M. A. Lampert, P. Mark, Current Injection in Solids, Academic Press, New York and London (1970).

4 Photocurrent multiplication in polymer solar cells

Abstract

For very low Langevin recombination, or when electron and hole mobility are a very different, photogenerated charge carriers can affect the space charge field and modify the injection of charge carriers. We show by simulations and experimentally that under such conditions the photocurrent under forward bias can exceed the current from charge generation by light such that, effectively, photocurrent multiplication occurs.

4.1 Introduction

In Chapter 3 we showed that in polymer solar cells the photocurrent J_{ph} under forward bias is reduced because photogenerated charge carriers recombine with injected charge carriers. Under reverse bias, no carieres are injected and the effect is absent. As a consequence, J_{ph} is symmetric around the compensation voltage without injecting contacts. Further a simple analytical model has been presented that shows that under high forward bias J_{ph} scales inversely with $1 + \xi\gamma_{pre}$, in which γ_{pre} represents the extent of Langevin recombination and ξ is a positive constant:

$$J_{ph} = \frac{qGL}{1+\xi\gamma_{pre}} \tag{4.1}$$

The consequence of Equation (4.1) is that $J_{ph} \leq qGL$, or in words the photocurrent cannot be higher than the photon flux. On first sight this is straightforward consequence of the fact that solar cells convert photons into charges and that, excluding effects like multicarrier generation or singlet fission, the number of charges extracted cannot exceed the number of photons absorbed. Photocurrent, however, refers to the amount of additional current that passes when a cell is illuminated compared to the same cell in the dark. It does not necessarily imply that all charges passing the cell, where generated in the cell by a photon.

In this chapter we explore solar cells under forward bias in which the recombination rate is strongly reduced compared to Langevin recombination, *i.e.* $\gamma_{pre} < 0.1$ and under conditions where electron and hole mobilities are not balanced. We study numerically and experimentally the photocurrent in systems with $\gamma_{pre} < 0.1$. The simulations show that at very low recombination rates or with low recombination rates and unbalanced electron and hole mobilities the injection current is enhanced under illumination. This leads to photocurrent multiplication. The enhanced injection current under illumination is related to a modification of the net space charge and of the injection properties of the contacts under illumination.

Experimentally, we observe enhanced photocurrent in un-annealed and annealed P3HT:PCBM solar cells for which it has been established that bimolecular recombination is reduced compared to the Langevin rate that would be expected based on charge carrier mobility of the two components.

4.2 Experiment

P3HT:PCBM (1:1 by weight) devices were prepared on onto pre-cleaned glass substrate covered with patterned indium tin oxide (ITO, 14 Ω/sq). First a 50 nm thick

PEDOT:PSS (Clevios P, VP Al4083, Heraeus) was applied by spin coating, followed by spin casting a 500 nm thick P3HT:PCBM layer from chloroform. As back electrode LiF (1 nm), and Al (100 nm) were thermally evaporated in a vacuum of 10^{-7} mbar. Samples were studied before annealing (pristine), and after annealing at 80 °C for 10 min. and at 130 °C for 30 min. Layer thicknesses was determined with a Veeco Dektak 150 Surface Profiler. $J-V$ characteristics were measured with a Keithley 2400 source meter under illumination with a tungsten-halogen lamp with a Schott GG385 UV filter and a Hoya LB120 daylight filter at 100 mW/cm light intensity.

A solid state laser (B&W Tek Inc. 532 nm, 30 mW) and a mechanical chopper (Stanford Research SR 540 chopper, f = 175 Hz) to produce a square wave modulated illumination source were used to measure photocurrents and minimize the heating of the sample under illumination. The current was measured over a 2.5 Ohm probe resistor connected in parallel to the input of a lock-in amplifier (Stanford Research Systems SR830). The amplitude of the recorded signal is proportional to the photocurrent.

4.3 Results and discussion

4.3.1 Photocurrent multiplication

In Chapter 3 we showed that Langevin recombination with injected charge carriers can result in a reduction of the forward photocurrent. The extent of Langevin recombination, parameterized via γ_{pre}, determines the reduction of J_{ph} in forward bias via Equation (4.1). The simulations in Chapter 3 were restricted to $\gamma_{pre} > 0.1$. When γ_{pre} is significantly reduced compared to 0.1, an interesting observation can be made as seen in Figure 4.1, where the $J_{ph}-V$ curves are shown for a device with two injecting contacts when band bending is taken in to account. For $\gamma_{pre} < 0.1$ the photocurrent becomes much larger in forward bias than the maximum current expected from the generation rate (qGL). This is striking since the current due to photogenerated charges is principally limited by the generation rate. Moreover, Equation (4.1) does not predict this behavior. The fact that in the calculated $J_{ph}-V$ characteristics with $\gamma_{pre} < 0.1$ the photocurrent is much larger than qGL can only be explained by a larger injection under illumination than in the dark. Conceptually the calculated photocurrent can be expressed as:

$$J_{ph}^{calc} = J_{light}^{photogenrated} + J_{light}^{injected} - J_{dark}^{injected} \tag{4.2}$$

If $J_{\text{light}}^{\text{injected}} > J_{\text{dark}}^{\text{injected}}$ the photocurrent exceeds $J_{\text{light}}^{\text{photogenerated}}$ and hence qGL. Such a photo-enhanced injection was observed in some organic devices[1–4] and is known as photomultiplication.

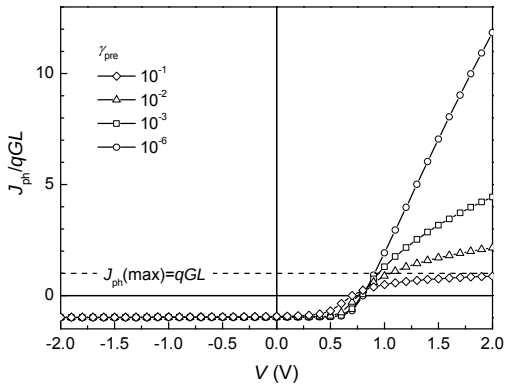

Figure 4.1: $J_{\text{ph}}-V$ curves normalized to the maximum photocurrent qGL for different low Langevin pre-factors (γ_{pre}). L = 100 nm, $\mu_{\text{n}} = \mu_{\text{p}} = 10^{-8}$ m^2/Vs, E_{g} = 1 eV, $G = 2.7 \times 10^{27}$ m^{-3}s^{-1}. Two Ohmic contacts were used in the simulations and band bending is considered.

To better understand what causes photomultiplication and illumination enhanced injection we look at the carrier density profile across the layer. Figure 4.2(a) shows the difference in electron density in the device under illumination and in dark, $\Delta n(x) = n_{\text{light}}(x) - n_{\text{dark}}(x)$, as a function of position x in the device for $\gamma_{\text{pre}} = 10^{-1}$ and $\gamma_{\text{pre}} = 10^{-3}$ at an applied voltage of 1.5 V. The Δn can be considered as the additional electron density that is created under illumination. The additional hole density under illumination $\Delta p(x) = p_{\text{light}}(x) - p_{\text{dark}}(x)$ versus x is the mirror symmetric to $\Delta n(x)$ at x = 50 nm because equal hole and electron mobilities and two Ohmic contacts are used.

Figure 4.2(a) shows that upon reducing the γ_{pre} from 10^{-1} to 10^{-3} $\Delta n(x)$ increases because of the reduced recombination of photogenerated electrons with holes. Close to the hole injecting contact a bump is observed at x = 92 nm for $\gamma_{\text{pre}} = 10^{-1}$ and at x = 97 nm for $\gamma_{\text{pre}} = 10^{-3}$ in the profile of $\Delta n(x)$. Beyond this bump $\Delta n(x)$ decreases abruptly which is due to a significant increase of bimolecular recombination between electrons and holes because the hole concentration increases several orders of magnitudes close to the hole injecting contact. Accumulation of photogenerated electrons (holes) close to the hole (electron) injecting contact modifies the space charge at the contact and promotes hole (electron) injection, leading to an enhanced injection under illumination.[5]

To verify how the space charge is modified under illumination we plot in Figure 4.2(b) $\Delta p(x) - \Delta n(x)$, which is the difference between the additional hole and electron densities and corresponds to the net space charge change under illumination. If $\Delta p - \Delta n = 0$, the net space is not modified under illumination, but for $\Delta p - \Delta n \neq 0$

the net space charge has changed by the illumination. Figure 4.2(b) shows the $\Delta p - \Delta n$ profile for $\gamma_{pre} = 10^{-1}$ and $\gamma_{pre} = 10^{-3}$ at a voltage of 1.5 V. Clearly, the net space charge is modified under illumination. The most noticeable changes in net space charge ($\Delta p - \Delta n$) occur in the region x = 85–100 nm, *i.e.* close to the hole injecting contact. For $\gamma_{pre} = 10^{-1}$ a negative peak in $\Delta p - \Delta n$ is observed at x = 91 nm and $\Delta p - \Delta n$ changes sign at x = 95 nm. Decreasing the γ_{pre} to 10^{-3} the negative peak in $\Delta p - \Delta n$ shifts to x = 97 nm and increases in magnitude; $\Delta p - \Delta n$ changes sign around x = 98 nm. The shift of the negative peak of $\Delta p - \Delta n$ (*i.e.* an enhanced electron density) closer to the hole injecting contact when γ_{pre} is decreased from 10^{-1} to 10^{-3} will enhance hole injection under illumination. Likewise, electron injection is enhanced at the electron injecting contact under illumination, because the device is symmetric. The enhanced injection for a decreasing bimolecular recombination rate for $\gamma_{pre} < 10^{-1}$ results from a modification of the net space charge under illumination by the photogenerated carriers. This effect is the most pronounced for very low Langevin pre-factors from γ_{pre} =10^{-3} − 10^{-6}. We note that for P3HT:PCBM solar cells, Langevin pre-factors between in the range $10^{-4} < \gamma_{pre} < 1$ have been reported in different experimental studies.[6–11]

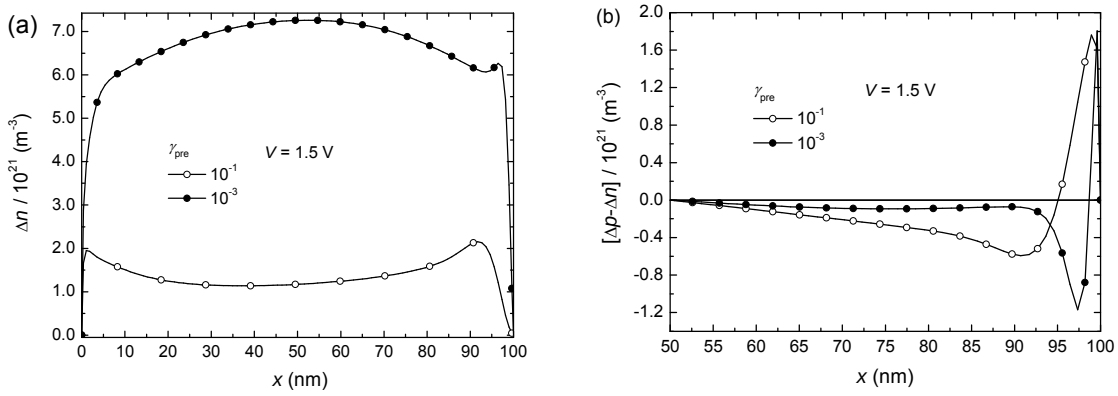

Figure 4.2: (a) Additional electron density $\Delta n(x) = n_{light}(x) - n_{dark}(x)$ under illumination for Langevin pre-factors $\gamma_{pre} = 10^{-1}$ and 10^{-3}. (b) Difference between the additional hole density $\Delta p(x)$ and electron $\Delta n(x)$ densities across the solar cell under illumination for Langevin pre-factors 10^{-1} and 10^{-3}. L = 100 nm, $\mu_n = \mu_p = 10^{-8}$ m^2 /Vs, E_g = 1 eV, $G = 2.7 \times 10^{27}$ m^{-3}s^{-1}. Two Ohmic contacts were used in the simulations. The electron injecting contact is at x = 0 nm, the hole injecting contact at x = 100 nm.

The simulations have shown that bimolecular recombination processes are crucial in determining the photocurrent, by causing photogenerated and injected carriers to recombine and by changing the space charge distribution under illumination. Both the bimolecular Langevin recombination rate and the space charge distribution are also influenced by the mobilities of the charge carriers. Until now we assumed

$\mu_n = \mu_p = 10^{-8}$ m^2/Vs. To investigate the effect of unbalanced mobilities ($\mu_n \neq \mu_p$) we simulated J_{ph}–V curves for $\gamma_{pre} = 0.1$ using a constant hole mobility $\mu_p = 10^{-8}$ m^2/Vs but an electron mobility that changes from $\mu_n = 10^{-8}$ to 10^{-11} m^2/Vs (Figure 4.3). Figure 4.3(a) shows that if the electron mobility is reduced with respect to the hole mobility the normalized photocurrent in forward bias becomes larger than unity. This evidences that at moderately low Langevin pre-factors and unequal hole and electron mobilities photo-enhanced injection occurs.

We verified that for $\gamma_{pre} = 1$ the photocurrent remains below saturation current for highly dissimilar mobilities, although J_{ph}/qGL is higher in forward bias compared to equal mobilities. The latter result can be related to the fact that the injected carriers with the highest mobility dominate the recombination with the photogenerated carriers because the density of the injected carriers with lowest mobility will decrease close to its injecting contact quickly due to recombination with the other injected carrier.

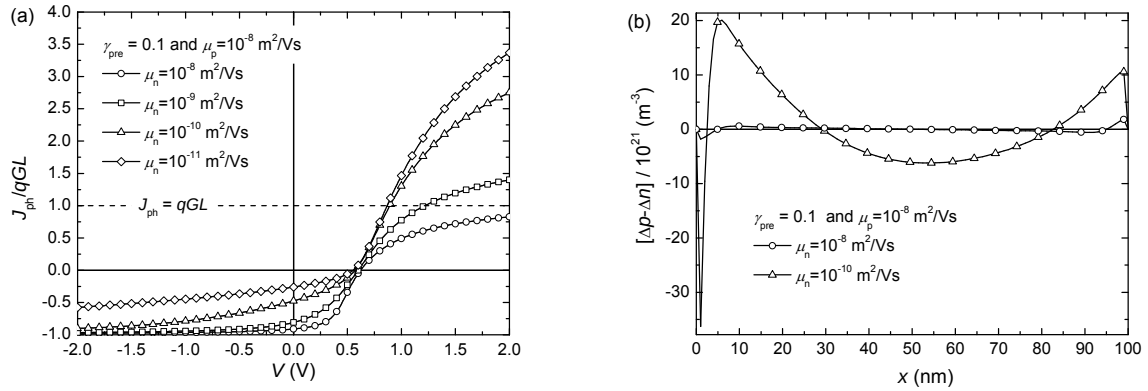

Figure 4.3: (a) Simulated J_{ph}–V curves normalized to the maximum photocurrent qGL. Two Ohmic contacts were used in the simulations and L = 100 nm, E_g = 1 eV, $G = 2.7 \times 10^{27}$ m^{-3}s^{-1}, $\gamma_{pre} = 0.1$, $\mu_p = 10^{-8}$ m^2/Vs, and $\mu_n = 10^{-8} - 10^{-11}$ m^2/Vs. (b) Difference between the additional hole (Δp) and electron Δn densities under illumination for different $\mu_n = 10^{-8}$ and 10^{-10} m^2/Vs.

The change of the net positive space charge under illumination with respect to dark ($\Delta p - \Delta n$) is plotted in Figure 4.3(b) as a function of position in the devices. A clear change and an absolute increase across the $\Delta p - \Delta n$ profile is observed when the electron mobility is decreased from $\mu_n = 10^{-8}$ to 10^{-11} m^2/Vs. This shows that for unequal electron and hole mobilities and $\gamma_{pre} = 0.1$, the net space charge is significantly different under illumination compared to the dark, explaining the chances in photocurrent Figure 4.3(a).

The enhanced injection under illumination for unequal mobilities and $\gamma_{pre} = 0.1$ can, tentatively, be rationalized by considering *i*) that recombination is low enough to allow accumulation of photogenerated carriers, and *ii*) that the slower photogenerated

electron resides longer than the faster extracted photogenerated hole. Therefore photogenerated electrons accumulate more than the photogenerated holes in the device creating a charge imbalance which has to be compensated by additional injection of holes.

In conclusion, the simulations show that photocurrent multiplication can result from a modification of the space charge under illumination either when the recombination rates are extremely low or when the recombination rate is reduced and charge transport is unbalanced.

4.3.2 Photocurrent multiplication in P3HT:PCBM devices

The experimentally measured and corrected $J_{ph}-V$ curves of the PDPPTPT:PCBM devices in Chapter 3 provided no clear evidence for a photo-enhanced injection in forward bias. However, in thick (L = 500 nm) P3HT:PCBM solar cells the signatures of photo-enhanced injection of carriers in forward bias can be observed.

Figure 4.4(a) shows the dark and illumination $J-V$ characteristics measured under continuous 100 mW/cm white light illumination of a ITO/PEDOT:PSS/ P3HT:PCBM/LiF/Al solar cell before annealing (pristine), and after annealing at 80 °C for 10 min. and at 130 °C for 30 min. The performance of the P3HT:PCBM solar cells increases with the annealing steps. This is well known and is related to a better crystallization of P3HT and PCBM, improved phase separation, and enhanced charge carrier mobilities.[12,13] The dark $J-V$ characteristics show low leakage currents in reverse bias for all the annealing steps (Figure 4.4(b)). Without annealing the device has a very low dark current in forward bias due to a low hole mobility of the un-annealed P3HT (3×10^{-12} m^2/Vs) in the blend.[13] When the device is annealed the dark current increases which due to an improved hole mobility upon P3HT crystallization. A striking observation in Figure 4.4(a) is the significant increase of the forward current upon illumination compared to the dark for the pristine device and the device annealed at 80 °C. This significant difference between the illumination current and dark current cannot be attributed to the photocurrent, because it is much larger than the reverse saturation photocurrent and also not to heating of the solar cell under illumination. The large increase of the current in forward bias under illumination strongly indicates a photo-enhanced injection of carriers. After the solar cell is annealed at 130 °C no significant difference in the current density in dark and under illumination can be seen in the $J-V$ characteristics.

To exclude heating effects and measure the photocurrent accurately, the $J_{ph}-V$ curves were measured with pulsed illumination for the different annealing steps of the solar cell. The corresponding $J_{ph}-V$ curves are shown in Figure 4.4(c), before and after correcting for the series resistance (R_s = 24 Ω). The uncorrected and corrected

$J_{ph}-V$ curves before and after annealing at 80 °C superimpose in reverse bias and do not show a significant difference in forward bias because the dark currents are low for these measurements. After annealing the solar cell at 130 °C, the corrected $J_{ph}-V$ curve shows a much larger photocurrent in forward bias than the uncorrected $J_{ph}-V$ curve. This increase of the photocurrent after correction is due to the large injection current of the solar cell in forward bias and due to the voltage drop at electrodes after annealing at 130 °C, similar to the results obtained for the ITO/PEDOT:PSS/ PDPPTPT:PCBM/LiF/Al devices (Chapter 3, Figure 3.1(c)).

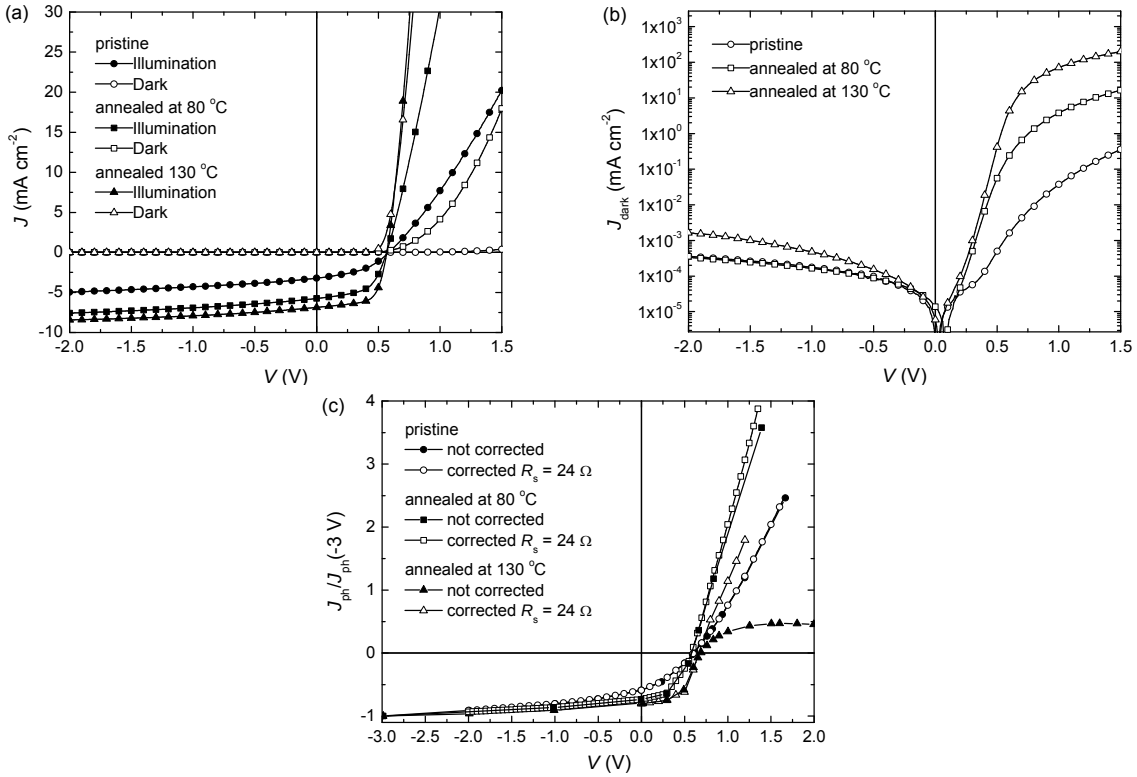

Figure 4.4: (a) $J-V$ characteristics of a 500 nm thick P3HT:PCBM solar cell for various annealing steps. (b) Semi-logarithmic plot of the dark currents. (c) $J_{ph}-V$ curves measured with modulated light source before (solid symbols) and after correction for the effect of the series resistance (open symbols) for the same P3HT:PCBM solar cells shown in panel (a).

For each of the three P3HT:PCBM cells, the corrected J_{ph} normalized to the reverse saturation photocurrent (Figure 4.4(c)) is larger than unity in forward bias. Thus for all the annealing steps photo-enhanced injection of charge carriers is observed in forward bias. Comparing the normalized photocurrent at 1.2 V for the different annealing steps the effect of photo-enhanced carrier injection is larger after annealing at 80 °C than at 130 °C, and lowest before annealing. This trend can qualitatively be explained by considering simultaneously the effect of the reduced

Langevin pre-factor and the effect of unbalanced charge transport on the injection current under illumination as shown in the simulation in Figures 4.3(a) and 4.3(b), respectively. When P3HT:PCBM is annealed the hole mobility is improved by about three orders of magnitude while the electron mobility does not vary significantly.[13] For instance, in pristine P3HT:PCBM devices hole mobilities are $\mu_p = 10^{-12}$ m^2/Vs but after annealing at 130 °C the hole mobility increases to 10^{-8} m^2/Vs. The electron mobility increases from $\mu_n = 10^{-8}$ m^2/Vs to 10^{-7} m^2/Vs in the same range.[13] By studying the bimolecular recombination we recently showed that the Langevin pre-factor depends on and decreases with annealing temperature.[14] The estimated γ_{pre} is 0.3, after annealing at 100 °C and 0.09 after annealing at 130 °C.[14] The reduction of γ_{pre} with annealing temperature is likely due to a more extended phase separation in the P3HT:PCBM blend with annealing temperature,[12] reducing the probability of recombination.

The photo-enhanced injection of charge carriers is lowest for the pristine device. For this device the electron and hole mobilities are most unbalanced, but the Langevin pre-factor is likely close to unity as a consequence of the intimate mixing, the photo-enhanced injection of carriers is small. By annealing to 130 °C, the Langevin pre-factor is reduced (γ_{pre} = 0.09),[14] but the electron and hole mobilities become much more balanced. These two opposing effects cause that the photo-enhanced injection of charge carriers and photocurrent multiplication are not strongly increased. Figure 4.4(c) shows that at 80 °C, the photo-enhanced current is largest after annealing at 80 °C. This can attributed to a low Langevin pre-factor and a more unbalanced hole and electron mobilities than after annealing at 130 °C.

4.4 Conclusions

We have studied numerically and experimentally photocurrent in solar cells for which Langevin recombination is suppressed. We found that under conditions were Langevin recombination is very low, or when electron and hole mobilities are unbalanced combined with a reduced bimolecular recombination, it is possible that the forward photocurrent is enhanced above the generation rate of charge carriers, such that photocurrent multiplication occurs. This effect is caused by a change in the space charge in the device under illumination, such that more carriers are injected in light than in dark. As the space charge change by illumination is largest when bimolecular recombination rate constant is low or when mobilities are unbalanced, these parameters contribute to conditions for finding photocurrent multiplication in polymer solar cells. Experimentally these effects were, quantitatively, demonstrated in P3HT:PCBM solar cells.

4.5 References

[1] M. Hiramoto, T. Imahigashi, M. Yokoyama, *Appl. Phys. Lett.* **1994**, *64*, 187.

[2] R. N. Marks, J. J. M. Halls, D. D. C. Bradley, R. H. Friend, A. B. Holmes, *J. Phys. Condens. Matter* **1994**, *6*, 1379.

[3] K. Nakayama, M. Hiramoto, M. Yokoyama, *Appl. Phys. Lett.* **2000**, *76*, 1194.

[4] J. R. Reynaert, V. I. Arhipov, P. Heremans, J. Poortmans, *Adv. Funct. Mater.* **2006**, *16*, 784.

[5] R. H. Parmenter, W. Ruppel, *J. Appl. Phys.* **1959**, *30*, 1548.

[6] A. Pivrikas, G. Juška, A. J. Mozer, M. Scharber, K. Arlauskas, N. S. Sariciftci, H. Stubb, R. Österbacka, *Phys. Rev. Lett.* **2005**, *94*, 176806.

[7] G. Sliaužys, G. Juška, K. Arlauskas, A. Pivrikas, R. Österbacka, M. Scharber, A. Mozer, N. S. Sariciftci, *Thin Solid Films* **2006**, *511-512*, 224.

[8] G. Juška, G. Sliaužys, K. Genevičius, K. Arlauskas, A. Pivrikas, M. Scharber, G. Dennler, N. S. Sariciftci, R. Österbacka, *Phys. Rev. B* **2006**, *74*, 115314 ().

[9] C. G. Shuttle, B. O'Regan, A. M. Ballantyne, J. Nelson, D. D. C. Bradley, J. R. Durrant, *Phys. Rev. B* **2008**, *78*, 113201.

[10] C. Deibel, A. Baumann, A. Wagenpfahl, V. Dyakonov, *Synth. Met.* **2009**, *159*, 2345.

[11] G. Juška, K. Genevičius, N. Nekrašas, G. Sliaužys, R. Österbacka, *Appl. Phys. Lett.* **2009**, *95*, 013303.

[12] X. Yang, S. C. Veenstra, W. J. H. Verhees, M. M. Wienk, R. A. J. Janssen, J. M. Kroon, M. A. J. Michels, J. Loos, *Nano Lett.* **2005**, *5*, 579.

[13] V. D. Mihailetchi, H. X. Xie, B. de Boer, L. J. A. Koster, P. W. M. Blom, *Adv. Funct. Mater.* **2006**, *16*, 699.

[14] L. J. A. Koster, M. Kemerink, M. M. Wienk, K. Maturová, R. A. J. Janssen, *Adv. Mater.* **2011**, *23*, 1670.

5 The effect of bias light on the spectral responsivity of organic solar cells

Abstract

The spectral responsivity, *S,* and the related spectrally resolved photon-to-electron external quantum efficiency, *EQE*, are standard device characteristics of organic solar cells and can be used to determine the short-circuit current density and power conversion efficiency under standardized test conditions by integrating over the spectral irradiance of the solar emission. However, in organic solar cells *S* and *EQE* can change profoundly with light intensity as a result of processes that vary non-linearly with light intensity such as bimolecular recombination of electrons and holes or space charge effects. To determine the *S* under representative solar light conditions, it is common to use modulated monochromatic light and lock-in detection in combination with simulated solar bias light to bring the cell close to 1 sun equivalent operating conditions. In this chapter we demonstrate analytically and experimentally that the *S* obtained with this method is in fact the differential spectral responsivity, *DS*, and that the real *S* and the experimental *DS* can differ significantly when the solar cells exhibit loss processes that vary non-linearly with light intensity. In these cases the experimental *DS* will be less than the real *S*. We propose a new, simple, experimental method to more accurately determine *S* and *EQE* under bias illumination. With the new method it is possible to accurately estimate the power conversion efficiency of organic solar cells.

5.1 Introduction

Compared to solar cells based on crystalline inorganic semiconductors, organic photovoltaic devices suffer from the moderate hole and electron mobilities associated with amorphous organic semiconductors and higher charge recombination rates due to a lower dielectric permittivity. As a result, non-linear light-intensity-dependent loss processes are generally more significant in organic solar cells than in inorganic solar cells. Well-established examples are bimolecular recombination[1-5] or space charge effects[6,7] that depend in a non-linear fashion on the concentration of photogenerated charge carriers. As a consequence the short-circuit current density (J_{SC}) of organic solar cells often varies sub-linearly with light intensity and the spectral responsivity (S) is not constant.

The spectral responsivity is related to the external quantum efficiency (EQE), which is the fraction of collected charges to incoming photons, and given by:

$$S(\lambda) = EQE(\lambda) \cdot \frac{q\lambda}{hc} \tag{5.1}$$

with q the elementary charge, h the Planck constant, and c and λ the speed and wavelength of light, respectively. Both S and EQE can provide important information about optical and electrical processes involved in the generation and collection of charges and are standard device characteristics. Under conditions where S and EQE are dependent on light intensity it is important to determine them under relevant test conditions. To compare the performance of photovoltaic cells, standard test conditions (STC) have been defined. Under STC, the test cell has a temperature of 25 °C and is irradiated by the AM 1.5 G (AM: air mass) global reference spectrum at an intensity (irradiance) of I = 100 mW/cm^2.[8,9]

To avoid overestimation of S or EQE, the intensity-dependent losses are taken into account by illuminating the test cell at 1 sun equivalent bias light intensity during the measurement of S or EQE. In practice, the $S(\lambda)$ under illumination is determined by applying a continuous simulated solar light bias at 1 sun equivalent intensity and measuring the additional short-circuit current density generated by calibrated modulated monochromatic light with a low intensity amplitude $dI(\lambda)$. By using lock-in detection (LID), the modulation of the short-circuit current density (dJ_{SC}) generated by the modulated monochromatic illumination $dI(\lambda)$ in the test cell is determined. The measured spectral responsivity $S(\lambda)$ at given wavelength λ of monochromatic illumination is then obtained by the fraction: $dJ_{SC}/dI(\lambda)$.

At this point it is important to point out that the spectral responsivity ($dJ_{SC}/dI(\lambda)$) measured with lock-in detection is not precisely the spectral responsivity

($S(\lambda) = J_{SC}/I(\lambda)$) but rather the differential spectral responsivity $DS(\lambda) = dJ_{SC}/dI(\lambda)$,[10] *i.e.* the first derivative of the short-circuit current density with intensity. In fact, the differential spectral responsivity equals the slope of the short-circuit current density − light intensity (J_{SC}−I) curve. When J_{SC} is non-linear with I, the spectral responsivity S is different from the differential spectral responsivity DS as discussed by Metzdorf.[10] To our knowledge, this difference has not been explicitly noticed by the organic solar cell community. As we will show below, the difference between the commonly measured $DS(\lambda)$ and the actual $S(\lambda)$ can lead to an underestimation of $S(\lambda)$, $EQE(\lambda)$, and J_{SC} at STC.

In this chapter we first summarize the measurement protocols for an accurate estimate of the power conversion efficiency, η, of a solar cell and then illustrate theoretically how the differential spectral responsivity DS measured with lock-in detection leads to an underestimation of S and EQE when J_{SC} is sub-linear with light intensity. Subsequently, we present experimental results on an efficient small band gap organic solar cell in which J_{SC} is sub-linear with light intensity to illustrate the problem. Finally, we suggest a simple procedure to determine the correct S, EQE, J_{SC}, and η under AM 1.5 G illumination.

5.2 Experimental

5.2.1 Device fabrication and materials

Solar cells were prepared by spin coating a layer of poly(3,4-ethylenedioxythiophene) :poly(styrenesulfonate) (PEDOT:PSS) (Clevios P, VP Al4083) on a pre-cleaned, patterned indium tin oxide (ITO) glass substrate. After annealing the PEDOT:PSS layer for 10 min. at 140 °C in an inert atmosphere, the active layer was spin coated from a chloroform:*o*-DCB (9:1 v/v) solution of 7 mg/mL poly[(2,5-bis(2'-hexyldecyl)-3,6-bis(4'-decyloxy-[2,2'-bithiophen]-5,5′-diyl) pyrrolo[3,4-c]pyrrole-1,4(2H,5H)-dione)-*alt*-(1,4-phenylene)] (PDPP4TOP)[11] as electron donor and 14 mg/mL [6,6]phenyl-C_{61}-butyric acid methyl ester (PCBM), also in an inert atmosphere. As top electrode 1 nm LiF and 100 nm Al were evaporated under 10^{-7} mbar vacuum. The PEDOT:PSS and the active layer thicknesses of the solar cell were ~35 and ~220 nm, respectively as determined with a Veeco Dektak 150 Surface Profiler.

5.2.2 Experimental setup and method

Current density − voltage (J−V) characteristics were measured with a Keithley 2400 source meter under ~100 mW/cm^2 simulated solar light illumination from a tungsten-halogen lamp (Philips Brillantline, 50 W) filtered by a Schott GG385 UV

filter and a Hoya LB120 daylight filter. Spectral responsivity measurements were conducted at different illumination intensities by biasing the solar cell with simulated solar light illumination from the tungsten-halogen lamp through the daylight filter. A lens was used to focus the illumination spot on the active area of the solar cell and a set of neutral density filters (New Focus, OD range 0.04-1.0) was used to vary the illumination intensity. We checked that (combinations of) these neutral density filters did not significantly distort the illumination spectrum. The device was kept in a nitrogen filled box behind a quartz window and irradiated with modulated monochromatic light, generated from a 50 W tungsten-halogen lamp (Philips focusline) and monochromator (Oriel, Cornerstone 130) with the use of a mechanical chopper. The spectral responsivity was recorded as a voltage over a 50 Ohm resistor using a lock-in amplifier (Stanford research Systems SR830) relative to a calibrated silicon solar cell as reference. The steady state short-circuit current density as a function of simulated solar light bias intensity of the solar cell was recorded with a Keithley 2400 source meter and using the simulated solar light bias source of the spectral responsivity setup. The average standard deviation in measuring the wavelength dependent *EQE* measurement in this setup is less than 0.005 in electrons/photons for wavelengths in the range of 350-800 nm where the $EQE > 0.1$. Only below 400 nm, the standard deviation reaches more than 0.01 occasionally.

5.2.3 Mismatch factor

The short-circuit current density (J_{SC}) under AM 1.5 G illumination is determined from the J_{SC} measured under simulated solar light illumination by mismatch correction following the procedure outlined in Subsection 5.3.1. First the intensity correction and then the spectral mismatch correction are performed. The intensity correction factor is given by the ratio between the short-circuit current of the silicon reference cell measured under simulated solar light illumination (7.62 mA) and the short-circuit current at AM 1.5 G illumination (7.13 mA). The intensity correction factor is then: 7.62 mA/7.13 mA = 1.069. To account for the spectral mismatch between the simulated solar light illumination and AM 1.5 G illumination and the spectral mismatch between the spectral responsivity of the reference cell and the solar cell, the mismatch correction factor (M) was calculated. The lamp spectrum was recorded with an Avantes NIR/vis spectrometer. The spectral mismatch factor was determined to $M = 1.084$. The J_{SC} under AM 1.5 G illumination is given by $J_{SC} = J_{SC}(E_S)/(1.069 \cdot 1.084)$, with $J_{SC}(E_S)$ the short-circuit current density measured under simulated solar light illumination of the solar simulator.

5.3 Theory

5.3.1 Power conversion efficiency

The power conversion efficiency of an organic solar can be determined from the current-density − voltage characteristics ($J-V$) of the solar cell recorded under AM 1.5 G illumination:

$$\eta = \frac{J_{SC} V_{OC} FF}{I_{AM1.5G}} \tag{5.2}$$

with J_{SC} the short-circuit current density, V_{OC} the open-circuit voltage, FF the fill factor, and $I_{AM1.5\,G} = 100$ mW/cm^2 the intensity of the AM 1.5 G spectral irradiance.

To measure a solar cell under AM 1.5 G irradiance outdoor or indoor is difficult. Outdoor, the AM 1.5 G spectrum is only obtained when the sky is free of clouds and when the solar light passes through the earth atmosphere at a zenith angle of 48.2°. Indoor, a solar simulator has to be used that simulates the AM 1.5 G spectrum. In practice, the shape of the spectral irradiance of the solar simulator $E_S(\lambda)$ always deviates from the shape of the spectral irradiance of the reference AM 1.5 G emission $E_R(\lambda)$. The standard technique to measure η under AM 1.5 G illumination with a solar simulator involves two steps. First, because V_{OC} and FF are not significantly influenced by a spectral mismatch between the simulator and the AM 1.5 G illumination they can be determined from the $J-V$ characteristics under simulated solar light. The J_{SC}, however, scales directly to the light intensity and is strongly dependent on the exact shape of the illumination spectrum because the solar cell has a specific absorption spectrum. Consequently, the measured J_{SC} with simulated illumination $E_S(\lambda)$ will be off from the J_{SC} under the reference AM 1.5 G illumination $E_R(\lambda)$. This offset will be larger when the solar cell absorbs in a region where the solar simulator and the AM 1.5 G spectra do not match exactly. Therefore, in a second step, J_{SC} must be determined more precisely. Two main methods exist to evaluate the J_{SC} at AM 1.5 G illumination.

The first method is based on a spectral mismatch correction which takes into account the difference between the simulator spectrum and the AM 1.5 G reference spectrum as well as the difference between the spectral responsivity of the test cell and the reference cell that is used to set the light intensity.[12-15] Basically, the solar simulator has to be adjusted to an equivalent intensity such that the solar cell under test delivers the same short-circuit current density as it would under AM 1.5 G illumination. The intensity of the solar simulator is calibrated with a stable reference cell by adjusting the intensity to a target J_{SC} of the reference cell. The target J_{SC} of the

reference cell is determined by the mismatch correction which takes into account the spectral mismatch between the spectral irradiance of solar simulator (E_S) and the AM 1.5 G reference (E_R) spectrum and the mismatch between the spectral responsivity of the reference cell (S_R) and solar cell under test (S_T).

$$M = \frac{\int S_R(\lambda)E_R(\lambda)d\lambda}{\int S_R(\lambda)E_S d\lambda} \cdot \frac{\int S_T(\lambda)E_S(\lambda)d\lambda}{\int S_T(\lambda)E_R(\lambda)d\lambda} \tag{5.3}$$

To determine the mismatch correction factor M and consequently the target $J_{SC,}$ the spectral responsivity of the solar cell and the irradiance spectrum of the solar simulator have to be measured.[13-15] We note that for calculating M using Equation (5.3), normalized values for $S_R(\lambda)$, $S_T(\lambda)$ and $E_R(\lambda)$ suffice and absolute values need not be used. Equation (5.3) further shows that to minimize deviation of M from unity, $S_R(\lambda)$ and $S_T(\lambda)$ preferably have the same shape as well as $E_S(\lambda)$ and $E_R(\lambda)$.

The second method to obtain J_{SC} under standard solar illumination is to measure the absolute spectral responsivity $S_T(\lambda)$ of the test cell and then integrate $S_T(\lambda)$ over the AM 1.5 G reference spectrum ($E_R(\lambda)$ at 100 mW/cm^2):

$$J_{SC} = \int S_T(\lambda, E_R)E_R(\lambda)d\lambda \tag{5.4}$$

Here $S_T(\lambda, E_R)$ signifies that the absolute spectral responsivity depends on λ and should be measured under a bias illumination that preferably matches the reference AM 1.5 G spectrum (E_R) and intensity (100 mW/cm^2).

5.3.2 Spectral responsivity

In this section we analyze under which conditions the differential spectral responsivity (*DS*) as it is commonly measured by lock-in detection (LID) deviates from the spectral responsivity (*S*). Typically, the *DS*(λ) is measured to determine the wavelength dependent *S*(λ) of a solar cell when biased with continuous simulated solar light bias illumination. By using modulated monochromatic light in combination with LID, it is possible to distinguish the contribution to the photocurrent of the low-intensity monochromatic illumination from the contribution of the high-intensity simulated solar light illumination. The amplitude measured with the lock-in amplifier is proportional to the amplitude of the short-circuit current density (dJ_{SC}) generated by the modulated monochromatic illumination ($dI(\lambda)$). The differential spectral responsivity (*DS*) is obtained by dividing the amplitude of the modulated photocurrent (dJ_{SC}) by the amplitude of the light intensity ($dI(\lambda)$) of the

modulated monochromatic illumination: $DS(\lambda) = dJ_{SC}/dI(\lambda)$.[10] To relate the spectral responsivity S to the differential spectral responsivity DS, we differentiate the photocurrent with respect to the light intensity. The photocurrent density is given by the product of the intensity (I) and spectral responsivity (S):

$$J = S \cdot I \tag{5.5}$$

Differentiating the photocurrent with respect to the intensity we obtain:

$$DS = \frac{dJ}{dI} = S + I\frac{dS}{dI} \tag{5.6}$$

The important consequence of Equation (5.6) is that DS is only equal to the S when S is independent of the light intensity I. Equation (5.5) shows that this condition only holds when the photocurrent varies linearly with light intensity. When the photocurrent is sub-linear with light intensity, *e.g.* due to light-intensity-dependent losses,[5] the differential spectral responsivity DS measured with the LID technique is not equal to the spectral responsivity S, but off by the second term on the right in Equation (5.6).

To illustrate the difference between DS measured with LID and S, we calculated both S and DS from the J_{SC}–I curve obtained from a simple analytical photocurrent model.[5] In this photocurrent model, drift, diffusion, and bimolecular recombination of charge carriers are considered but space charge effects are neglected. The derivation of the photocurrent model and the exact expression of the photocurrent as a function of voltage, generation rate and other device parameters can be found in the paper of Koster *et al.*[5] In the model we consider equal hole and electron mobility of 10^{-8} m^2/Vs an active layer thickness of 100 nm, a reduced Langevin recombination (pre-factor of 0.1), and an intensity of 1 sun corresponding to a generation rate of 10^{27} $m^{-3}s^{-1}$. Since bimolecular recombination is considered in the analytical photocurrent model, the photocurrent varies sub-linearly with light intensity as shown in Figure 5.1(a).

The spectral responsivity is calculated by taking the ratio of the photocurrent and the light intensity $S = J_{SC}/I$ while the differential responsivity is obtained by differentiating the photocurrent with respect to the light intensity $DS = dJ_{SC}/dI$. Figure 5.1(b) shows the normalized spectral responsivity and the differential spectral responsivity as a function of light intensity. As expected from Equation (5.6), the normalized S and DS both deviate from 1 as soon as the photocurrent becomes non-linear with light intensity. Since the photocurrent is sub-linear with light intensity, DS is less than S in the sub-linear intensity regime.

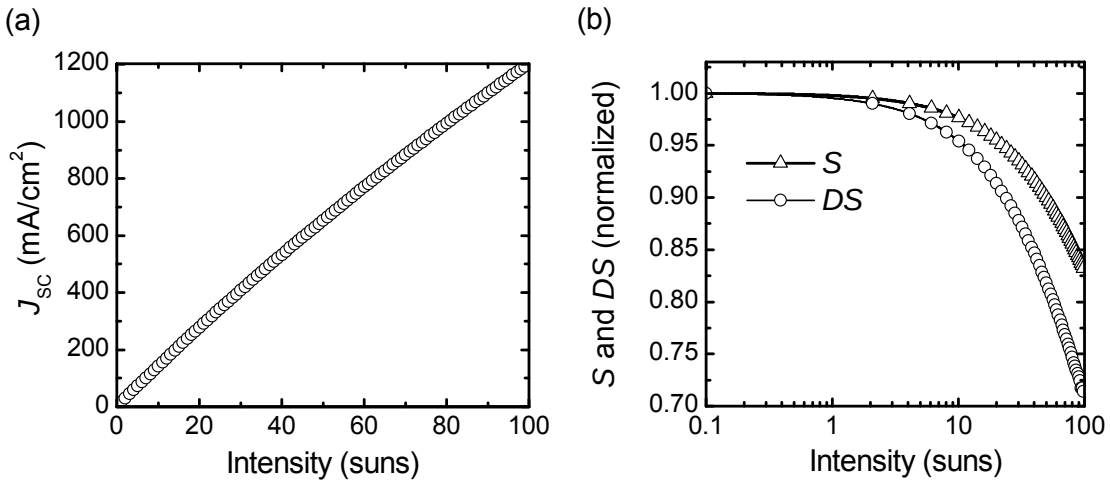

Figure 5.1: (a) Calculated photocurrent (J_{SC}, open markers) from a simple analytical model as a function of light intensity (I). (b) Spectral responsivity (S) and differential spectral responsivity (DS) as a function of light intensity, normalized at low light intensities.

This analysis and model calculations show that when the spectral responsivity (S) is measured with LID under bias light illumination and the organic solar cell possesses non-linear light-intensity-dependent losses, the measured data represent the differential spectral responsivity (DS) rather than the spectral responsivity S, and DS is expected to be lower than S.

5.4 Results and discussion

To experimentally illustrate the effect of a sub-linear J_{SC}–I regime on the measured S and EQE measured with LID we use a polymer:fullerene bulk-heterojunction solar cell with a thick active layer (~220 nm) consisting of a blend of PDPP4TOP:PCBM. PDPP4TOP is a small band gap donor polymer based on diketopyrrolopyrrole unit alternating with conjugated segment consisting of four thiophene and one benzene ring that provides a power conversion efficiency of ~4.7% in combination with PCBM as acceptor for 100 nm films.[11] For ~220 nm layers the device presents a clear sub-linear light intensity dependence of J_{SC} at 1 sun and is therefore well suited to demonstrate experimentally the difference between S and DS.

The J–V characteristics of the PDPP4TOP:PCBM solar cell with a 220 nm thick active layer are shown in Figure 5.2 (a) under illumination with a solar simulator and in the dark. For this cell V_{OC} = 0.50 V, FF = 0.47, J_{SC} = 16.30 mA/cm^2, and η = 3.9% are obtained. The spectral irradiance of the solar simulator does not exactly match the AM 1.5 G spectrum and therefore the measured J_{SC} is off from the real J_{SC} at AM 1.5 G illumination. To obtain the J_{SC} under AM 1.5 G illumination, the $S(\lambda)$ can

be measured, followed by integrating $S(\lambda)$ with the AM 1.5 G spectral irradiance using Equation (5.4).

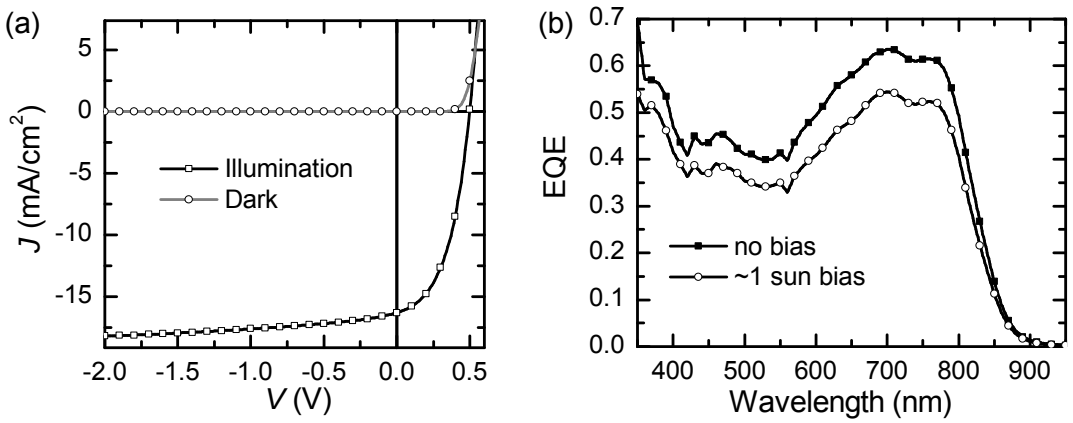

Figure 5.2: (a) J–V characteristics of a PDPP4TOP:PCBM solar cell with J_{SC} = 16.63 mA/cm^2, V_{OC} = 0.50 V, FF = 0.47, and η = 3.9%. (b) EQE measured with ~1 sun equivalent simulated solar light bias illumination and without light bias. The AM 1.5 G spectrally integrated short-circuit currents obtained from Equation (5.3) are J_{SC} = 15.15 mA/cm^2 without light bias and J_{SC} = 12.81 mA/cm^2 at ~ 1 sun bias.

Figure 5.2(b) depicts the measured EQE spectra when the solar cell is biased with simulated solar light at ~1 sun intensity and when the solar cell is not biased with simulated solar light. A significant reduction of the EQE by 15% is observed under simulated solar light bias. Integrating the EQE spectra with the AM 1.5 G solar spectrum using Equations (5.1) and (5.4), J_{SC} = 15.15 mA/cm^2 without bias and J_{SC} = 12.81 mA/cm^2 with bias are obtained.

The reduction of the measured EQE with light bias has often been interpreted as a reduction of the real EQE due to non-linear light-intensity-dependent losses. However, this interpretation is partly incorrect because the experimental EQE measured with LID represents $DS(\lambda)$ rather than $S(\lambda)$ ($EQE_{LID}(\lambda) = (hc/e\lambda) \cdot DS(\lambda)$). In Subsection 5.3.2 we have shown that for a sub-linear dependence of J_{SC} with light intensity, DS is less than S and hence EQE_{LID} is lower than the real EQE.

Figure 5.3(a) shows the J_{SC} of the PDPP4TOP:PCBM solar cell for different simulated solar light illumination intensities I. The relation between J_{SC} and I is sub-linear. At I = 70 mW/cm^2, *i.e.* below ~1 sun intensity (100 mW/cm^2), the deviation of the short-circuit current density from a linear dependence is clearly noticeable. At much lower light intensities J_{SC} essentially varies linearly with light intensity. Hence, at low light intensity the experimental EQE_{LID} corresponds to the real EQE but at somewhat higher light intensities, where J_{SC} varies non-linearly with light intensity, the measured EQE_{LID} will deviate from the real EQE. To compare the measured

EQE_{LID} to the real *EQE* we measured the *EQE* spectra (Figure 5.3(b)) over the same simulated solar light bias intensity range as J_{SC}.

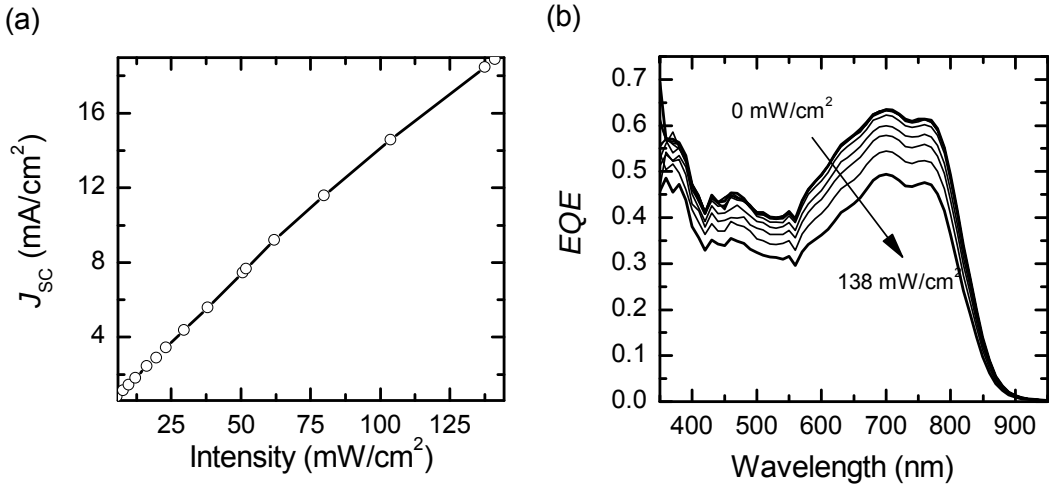

Figure 5.3: (a) Short-circuit current density (J_{SC}, open markers) as a function of simulated solar light illumination intensity of a 220 nm active layer PDPP4TOP:PCBM solar cell. (b) Measured *EQE* spectra at varying simulated solar light bias illumination intensities (0, 5, 9, 12, 16, 37, 60, 78, 101, 138 mW/cm^2). The curve recorded at 37 mW/cm^2 is the first that deviates visibly from the one without light bias.

From the J_{SC}–I curve we obtain the spectrally averaged external quantum efficiency <*EQE*> via:

$$\langle EQE \rangle = \frac{J_{SC}}{q\Phi} = \frac{1}{A} \cdot \frac{J_{SC}}{I} \tag{5.7}$$

where Φ is the total photon flux of the illumination source, and A is a constant that depends on the shape of the spectral irradiance of the lamp $E_S(\lambda)$, but is independent of I. It is important to note that <*EQE*> in Equation (5.7) corresponds to the definition of the real <*EQE*>.

The measured *EQE* spectra at different simulated solar light intensities from Figure 5.3(b) can be integrated with the AM 1.5 G reference spectrum $E_R(\lambda)$ according to Equations (5.1) and (5.4) to obtain an estimated short-circuit current density, via:

$$J'_{SC} = \int EQE_{LID}(\lambda) E_R(\lambda) \frac{\lambda}{hc} d\lambda \tag{5.8}$$

where we use the prime in J'_{SC} to indicate that the short-circuit current density has been determined by spectral integration of the *EQE* determined with LID.

In analogy with Equation (5.7) we define the corresponding spectrally averaged external quantum efficiency determined with lock-in detection as $\langle EQE_{LID} \rangle$:

$$\langle EQE_{LID} \rangle = \frac{1}{A'} \cdot \frac{J'_{SC}}{I} \tag{5.9}$$

where I is the intensity of the simulated solar bias illumination and A' is a constant that depends on the shape of the AM 1.5 G spectrum and on the shape of the simulated solar light used.

Without knowing A and A' in Equations (5.7) and (5.9), it is still possible to compare $\langle EQE \rangle$ with $\langle EQE_{LID} \rangle$, by normalizing them at the lowest measured bias intensity to unity and using the two normalization factors to scale the data. These normalized $\langle EQE \rangle_n$ and $\langle EQE_{LID} \rangle_n$ are plotted in Figure 5.4(a) as function of simulated solar light bias intensity. At low bias illumination intensity, $\langle EQE \rangle_n$ and $\langle EQE_{LID} \rangle_n$ are equal and remain very close to unity because of the absence of non-linear light-intensity-dependent losses. At higher bias illumination, $\langle EQE \rangle_n$ becomes less than unity with increasing bias light intensity. The normalized measured $\langle EQE_{LID} \rangle_n$ also decreases with increasing bias intensity from unity, but at a higher rate than $\langle EQE \rangle_n$. This is in agreement with the fact that the measured $\langle EQE_{LID} \rangle_n$ scales with *DS* as explained in Subsection 5.3.2 of this chapter while $\langle EQE \rangle_n$ scales with *S* (compare Figure 5.1(b)).

To confirm that the measured $\langle EQE_{LID} \rangle$ scales with the differential short-circuit current density rather than with the short-circuit current density itself, the normalized $\langle EQE_{LID} \rangle_n$ is integrated over the intensity and then divided by the light intensity to give:

$$\langle EQE \rangle_n^* = \frac{\int \langle EQE_{LID} \rangle_n \, dI}{I} \tag{5.10}$$

Figure 5.4(a) shows that $\langle EQE \rangle_n$ and $\langle EQE \rangle_n^*$ are virtually identical. This confirms that the measured $\langle EQE_{LID} \rangle$ scales with the differential short-circuit current density, and $\langle EQE \rangle_n^*$ with the real short-circuit current density.

To determine the correct $EQE(\lambda)$ spectrum at 1 sun simulated solar light intensity the normalized $\langle EQE \rangle_n$ or the integrated $\langle EQE \rangle_n^*$ at 1 sun intensity (100 mW/cm^2, see arrow in Figure 5.4(a)) can be used to scale the *EQE* spectrum. For the specific

PDPP4TOP:PCBM solar cells used here, a scaling factor of f = 0.94 at 1 sun intensity is obtained from $\langle EQE \rangle_n^*$. Multiplying the $EQE(\lambda)$ measured without bias illumination with the scaling factor f = 0.94, provides the correct $EQE(\lambda)$ spectrum at 1 sun intensity. Figure 5.4(b) compares the $EQE(\lambda)$ spectra measured with LID without bias illumination and with 1 sun bias illumination, with the corrected $EQE(\lambda)$ spectrum. Integration of the corrected $EQE(\lambda)$ spectrum at 1 sun intensity analogous to Equation (5.8), provides an estimate of the short-circuit current density under AM 1.5 G conditions of J'_{SC} = 14.24 mA/cm^2.

As mentioned in Subsection 5.3.1, the short-circuit current density at AM 1.5 G irradiance can also be determined from the short-circuit current density measured with the solar simulator setup (Figure 5.2(a)) by performing a mismatch correction. For our setup and this particular solar cell a correction factor of 1.1588 is calculated (see Section 5.2.3). Dividing the J_{SC} measured with the solar simulator (16.30 mA/cm^2) with 1.1588, provides the corrected J_{SC} = 14.07 mA/cm^2 for AM 1.5 G illumination. This matches very closely to J'_{SC} = 14.24 mA/cm^2 obtained from the corrected $EQE(\lambda)$ spectrum and confirms independently that scaling the EQE_{LID} spectrum with f can be used to obtain an accurate EQE (and S) and the correct short-circuit current density at AM 1.5 G illumination. The resulting estimates for the AM 1.5 G power conversion efficiency are η = 3.31% and η' = 3.35%.

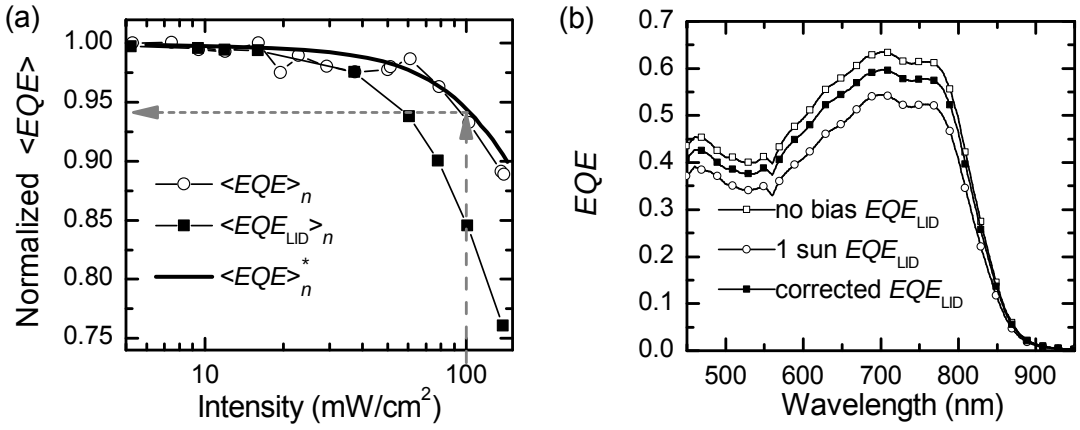

Figure 5.4: (a) Normalized spectrally averaged <EQE>'s of a ~220 nm active layer PDPP4TOP:PCBM solar cell as a function of bias intensity obtained from measuring the short-circuit current density (<EQE>$_n$), from integrating the measured EQE_{LID} spectra with the AM 1.5 G spectral irradiance (<EQE_{LID}>$_n$), and from $\langle EQE \rangle_n^*$ as defined in Equation (5.10). Arrows indicates the scaling factor f at 1 sun illumination that can be used to obtain the correct EQE spectrum at 1 sun illumination. (b) EQE spectra measured with LID without and with 1 sun bias illumination and the corrected EQE spectrum at 1 sun illumination.

5.5 Synopsis

Based on these results we propose a simple method to determine the correct $EQE(\lambda)$ spectrum under 1 sun simulated solar light intensity. In the simplest approximation it suffices to measure $EQE_{LID}(\lambda)$ without bias illumination and to measure J_{SC} versus light intensity I (maintaining a constant spectral shape of the light). J_{SC}/I is proportional to the spectrally averaged $<EQE>$ and by normalizing J_{SC}/I at the lowest light intensity, as is done in Figure 5.4(a), it is possible to find the scaling factor f at I = 100 mW/cm^2 that is needed to scale the measured $EQE_{LID}(\lambda)$ and obtain the correct $EQE(\lambda)$ under 1 sun illumination conditions. In this method it important to check that at low I, the normalized J_{SC}/I is virtually constant and shows a plateau region as shown in Figure 5.4(a).

A more sensitive technique to measure J_{SC}/I as function of light intensity involves measuring the $EQE_{LID}(\lambda)$ under different bias light intensities (as shown in Figure 5.3(b)), followed by determining the spectrally integrated $<EQE_{LID}>$ by Equation (5.8), and the intensity integrated $\langle EQE \rangle^*$ by Equation (5.10) as function of I. By normalizing $\langle EQE \rangle^*$ to unity at the lowest I, the scaling factor f can found as the value of $\langle EQE \rangle_n^*$ at I = 100 mW/cm^2.

Using spectral integration over the AM 1.5 G irradiance, the corrected $EQE(\lambda)$ can be used to obtain an accurate estimate of the short-circuit current density (J_{SC}) under AM 1.5 G conditions.

5.6 Conclusion

We have shown theoretically and experimentally that the spectral responsivity $S_{LID}(\lambda)$ and external quantum efficiency $EQE_{LID}(\lambda)$, measured with lock-in detection deviate from the real $S(\lambda)$ and $EQE(\lambda)$ when the short-circuit current density is non-linear with light intensity. The prime reason for the deviation is that S_{LID} actually represents the differential spectral responsivity DS, rather than S. We further developed a simple method to determine the correct $S(\lambda)$ and $EQE(\lambda)$ spectra under 1 sun illumination conditions from the $EQE_{LID}(\lambda)$ measured without illumination and the simulated solar-light intensity-dependence of short-circuit current density. By integrating the corrected $S(\lambda)$ with the AM 1.5 G spectral irradiance it is possible to accurately estimate the short-circuit current density of the solar cell under standard test conditions.

5.7 References

[1] I. Riedel, N. Martin, F. Giacalone, J.L. Segura, D. Chivase, J. Parisi, V. Dyakonov, *Thin Solid Films* **2004,** *451*,43.

[2] M.M. Mandoc, F.B. Kooistra, J.C. Hummelen, B. de Boer, P.W.M. Blom, *Appl. Phys. Lett.* **2007***, 91*, 263505.

[3] H. Azimi, A. Senes, M.C. Scharber, K. Hingerl, C.J. Brabec Adv. Energy Mater **2011**, *1*, 1162.

[4] G.F.A. Dibb, T. Kirchartz, D. Credgington, J.R. Durrant, J. Nelson, *J. Phys. Chem. Lett.* **2011**, *2*, 2407.

[5] L.J.A. Koster, M. Kemerink, M.M. Wienk, K. Maturová, R.A.J. Janssen, Adv. Mater. **2011**, *23*, 1670.

[6] V. D. Mihailetchi, L.J.A. Koster, P.W.M. Blom, *Phys. Rev. Lett.***2005**, *94*, 126602.

[7] J. Szmytkowski, *J. Phys. D-Appl. Phys.* **2007**, *40*, 3352.

[8] ASTM Standard G173, Standard Tables for Reference Solar Spectral Irradiances: Direct Normal and Hemispherical on 37° Tilted Surface, American Society for Testing and Materials, West Conshocken, PA, USA.

[9] NREL, http://rredc.nrel.gov/solar/spectra/am1.5/, Accessed August 23rd, 2012.

[10] J. Metzdorf, *Appl. Opt.* **1987**,*26*, 1701.

[11] K.H. Hendriks, manuscript in preparation.

[12] C.H. Seaman, *Sol. Energy* **1982**, *29*, 291.

[13] J.M. Kroon, M.M. Wienk, W.J.H Verhees, J.C. Hummelen, *Thin Solid Films* **2002**, *403*, 223.

[14] V. Shrotriya, G. Li, Y. Yao, T. Moriarty, K. Emery, Y. Yang, *Adv. Funct. Mater.* **2006**, *16*, 2016.

[15] H.J. Snaith, *Energy Environ. Sci.* **2012**, *5*, 6513.

6 Effect of illumination wavelength and intensity profile on the performance of organic solar cells

Abstract

In this chapter, we investigate the use of lasers for monochromatic bias illumination of organic solar cells. Compared to traditional white light bias sources such as halogen or xenon lamps, laser illumination is much easier to handle due to the extremely low beam divergence. Furthermore, monochromatic (or at least spectrally shifted) bias illumination is required to measure the spectral response of the individual subcells of an organic tandem solar cell. On the other hand, the optical electric field in the photoactive layer will be different for each wavelength and this motivates investigating laser illumination as suitable a source of bias light. In this chapter the current density voltage characteristics are measured for an organic solar cell with 532 and 633 nm laser illumination and results are compared to measurements under simulated solar light. To explain and elucidate the observed differences, an analytical two-dimensional model and combined optical and electrical drift-diffusion simulations are used. We show that a non homogenous light intensity profile over the active area of the cell associated with laser light can reduce the performance of the solar cell through a loss in fill factor. This effect can easily be minimized by increasing the beam width. We further show that the wavelength of monochromatic light does influence the generation profile and, hence, the collection of charges via complex combination of effects.

6.1 Introduction

In the previous chapter we proposed a new method to measure the spectral response of single junction organic solar cells under bias illumination. As bias illumination we used filtered light from a tungsten-halogen lamp to create an illumination source with a spectrum and intensity resembling the AM 1.5 G irradiance. In the experimental setup we used a mirror and two lenses to focus sufficient light from solar simulator on the solar cell to reach a high enough intensity. A neutral density filter wheel was used to adjust the intensity.

The use of simulated solar light as illumination bias in a spectral response setup is, however, rather unpractical and the alignment can be time consuming. Lasers are more practical than lamps as illumination source mainly because their beams have a very small divergence and are easier to handle, which simplifies the optical setup. In addition, lasers can reach high monochromatic light intensities, which is advantageous when measuring the spectral response of a tandem. For determining the spectral response of the individual subcells of an organic tandem solar cell it is necessary to bias one subcell with monochromatic light while probing the spectral response of other subcell.[1] The bias light ensures that the subcell that is probed remains current limiting in the entire wavelength range. To measure the spectral response of both subcells, two lasers with complementary wavelengths are used. Each laser is used to bias one of the two subcells. The question, however, if laser light represents as a valid alternative to white light bias illumination, remains to be answered.

In this chapter we investigate the appropriateness of laser illumination as a light source to measure the performance of an organic solar cell. We compare the current density voltage ($J-V$) characteristics of an organic solar cell illuminated by lasers at 532 and 633 nm to the $J-V$ recorded for simulated solar illumination, under conditions where the same amount of charges are generated. We find that the width of the laser intensity profile has a considerable effect on the $J-V$ curve and explain this using a two-dimensional (2D) analytical model. We explore the effect of monochromatic illumination on the $J-V$ characteristics by combined optical and electrical simulations.

6.2 Experiment

6.2.1 Device fabrication and characterization

Solar cells were prepared by spin coating a layer of poly(3,4-ethylenedioxythiophene) :poly(styrenesulfonate) (PEDOT:PSS) (Clevios P, VP Al4083) on a pre-cleaned

patterned indium tin oxide (ITO) glass substrate. After annealing the PEDOT:PSS layer for 10 min. at 140 °C in an inert atmosphere, the active layer was spin coated from a chloroform:*o*-DCB (9:1 v/v) solution of 7 mg/mL poly[(2,5-bis(2'-hexyldecyl)-3,6-bis(4'-decyloxy-[2,2'-bithiophen]-5,5′-diyl)pyrrolo[3,4-c]pyrrole-1,4 (2H,5H)-dione)-*alt*-(1,4-phenylene)] (PDPP4TOP),[2] as electron donor, and 14 mg/mL [6,6]phenyl-C_{61}-butyric acid methyl ester (PCBM), as electron acceptor, also in an inert atmosphere. As top electrode 1 nm LiF and 100 nm Al were evaporated under 10^{-7} mbar vacuum. The active area of the cell defined by the overlap of the ITO and LiF/Al electrodes is 0.092 cm^2. The PEDOT:PSS and the active layer thicknesses of the solar cell were ~35 and ~220 nm, respectively as determined with a Veeco Dektak 150 Surface Profiler.

J−*V* characteristics were measured with a Keithley 2400 source meter. Simulated solar light of 100 mW/cm^2 from a tungsten-halogen lamp (Philips Brillantline, 50 W) filtered by a Schott GG385 UV filter and a Hoya LB120 daylight filter was used for white light illumination. For monochromatic illumination 532 nm (B&W, Tek Inc., 30 mW) and 633 nm (JDS Uniphase, 1144P, 35 mW) cw lasers were used. The laser beam was diverged by a lens and then centered on a mask that covers the solar cell with a circular aperture of 1 mm radius. The solar cell was positioned 13 cm behind the lens. A circular variable neutral density filter was used to adjust the illumination intensity of the laser. The solar cell was kept in a nitrogen filled box behind a quartz window during the *J*−*V* measurements done under laser illumination.

6.2.2 Measuring the intensity profile of a laser beam

Intensity profiles of the laser beam were measured with the blade method. A razor blade (Gillette) positioned perpendicular to the laser beam was moved by a translation stage to gradually cover the laser beam. The uncovered part of the laser beam was focused by a lens positioned behind the blade on a Si photodiode to record the intensity. The intensity profile of the laser beam was determined from the first derivative of the intensity *vs.* blade position.

6.2.3 Optical and drift diffusion simulation

The charge generation profile as a function of wavelength was determined with Setfos 3 (Fluxim AG, Switzerland), which is based on the transfer matrix formalism and allows to calculate the optical electric field in a multilayer stack of thin films such as an organic solar cell. The required optical constants (*n*, *k*) as function of wavelength were determined from reflectance and transmission measurements performed on a PDPP4TOP:PCBM thin film spin cast on a quartz substrate. For all other layers *n* and *k* values were available.[1] The charge generation rate, which scales

to the absorption profile, across the active layer was coupled to a drift-diffusion program to generate *J*−*V* curves for a given set of electrical input parameters. We use the drift-diffusion program developed by Koster *et al*.[3] For the simulation we used Ohmic contacts and equal hole electron mobilities, which were assumed to be constant with electric field and carrier density.

6.3 Results and discussion

6.3.1 *J*−*V* characteristics with monochromatic and white light

To investigate the effect of monochromatic laser illumination on the solar cell performance we measured *J*−*V* curves of a PDPP4TOP:PCBM bulk heterojunction solar cell with a 220 nm thick active layer under simulated solar illumination and under green (532 nm) and red (633 nm) cw laser illumination. In measuring the *J*−*V* under laser illumination the active area of the solar cell is covered with a mask with an aperture of 1 mm radius. The laser intensity was adjusted such that the current density at –4 V under laser illumination matches the current density at −4 V under simulated solar light. This ensures that the charge generation rate in the cell is identical for each illumination source. Figure 6.1 compares the *J*-*V* curves for 532 nm, 633 nm, and white light illumination. The *J*-*V* curves under 532 nm and 633 nm were slightly scaled to match exactly the solar illumination current density at −4 V. Before scaling the current densities at −4 V were 16.27, 16.03, and 16.49 mA/cm^2 for green, red, and white light illumination, respectively. This small deviation should have no effect on the shape of the *J*−*V* curves.

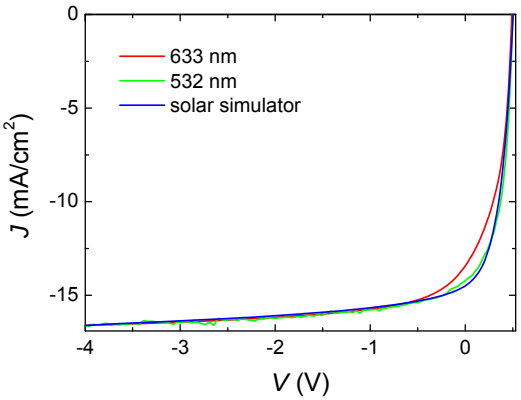

Figure 6.1: *J*−*V* characteristics of the PDPP4TOP:PCBM solar cell measured under solar simulated illumination and under green (532 nm) and red (633 nm) laser illumination.

Figure 6.1 shows that under red laser illumination the solar cell gives a lower fill factor and the illumination current is significantly less between −0.5 and 0.43 V, than for the green laser or white light illumination, which are more similar but also not

identical. The difference between the $J-V$ characteristics measured under red and green laser illumination can have several explanations. One possible explanation is that the effects are caused by differences in the shape of the absorption profile in the vertical direction of active layer under red, green, and white light illumination. As the solar cell consists of several layers with different refractive indices and layer thicknesses on the order of the wavelength, the layer stack forms an optical cavity and the optical electrical field in the layer will differ for different wavelengths. This can have an effect on the transport properties of generated carriers and therefore on the shape of the $J-V$ curve.[4-6] Another explanation is that the intensity profile on the solar cell of the green and red laser is different in the lateral direction. For illumination a lens was used to increase the divergence of the laser beam, which is then centered on an aperture of 1 mm radius to obtain a flattened intensity profile on the solar cell. However, the exact intensity profile is not known and it is possible that the profiles differ for the green and red lasers. When the intensity is adjusted to the reference current, the maximum intensity of a narrow profile will be higher than that of the wide profile. This can also lead to different $J-V$ curves. Below we investigate these possibilities.

6.3.2 Effect of beam intensity profile

We will first determine the intensity profile of the green and red laser at the position of the solar cell (aperture) during the $J-V$ measurement under laser bias. The intensity profile of both lasers is Gaussian:

$$I(x,d) = I_0 \exp\left(-2\frac{x^2}{w(d)^2}\right) \tag{6.1}$$

where x is the lateral direction, I_0 is the peak intensity, and w is the width of the beam. Both I_0 and w depend on the distance d from the laser. To determine the laser spot size the intensity profile has been measured using the blade method (see experimental) at the initial position of the solar cell ($d = d_i$) behind the lens. The recorded intensity of the red laser beam as function of the position a of the blade is shown in Figure 6.2(a). At a = 5 mm on the blade starts to cover the laser beam and the intensity decreases until at a = 10 mm the laser spot is fully covered and only the back ground light is recorded. The intensity as function of blade position is linked to the integral of Equation (6.1) in the following way:

$$I(a) = I_B + I_0 - I_0 \int \exp\left(-2\frac{(a-p)^2}{w^2}\right) da \tag{6.2}$$

with I_B the background intensity and p the peak position. The first derivative of the recorded intensity as function of blade position (Equation (6.1)) times −1 yield the Gaussian profile of the laser beam as shown in Figure 6.2(a). The normalized laser beam profiles of the green and red laser shown in Figure 6.2(b) were fitted to Equation (6.1). A beam width of w = 0.83 ± 0.05 mm and w = 1.20 ± 0.05 mm were obtained for the red laser and green laser beam, respectively. Clearly, the intensity profile on the active area of the solar cell, indicated by the overlap of the grey area with the beam profiles is not flat. For the 532 nm laser the intensity of the illuminated area on the solar cell drops to 30 % at the edges, while for 633 nm the illumination intensity drops to 5% at the edges of the aperture.

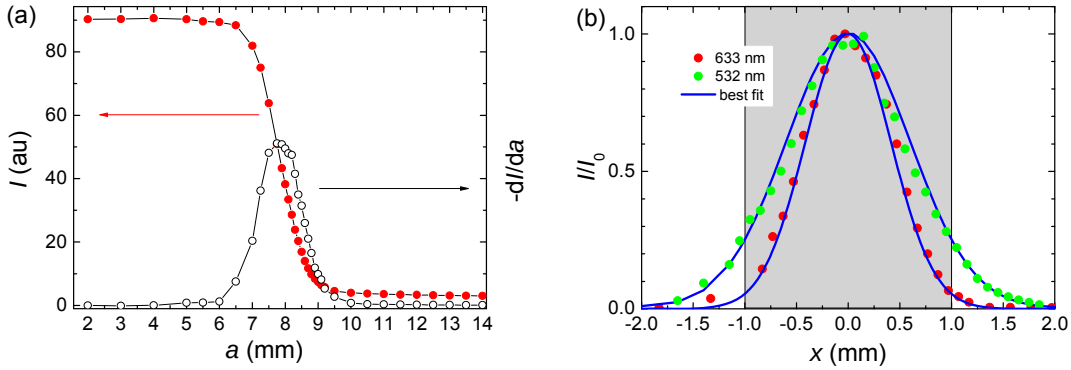

Figure 6.2: (a) Measured intensity as a function of blade position of the 633 nm laser beam and profile obtained from the first derivative of the intensity − blade position curve. (b) Profiles determined for the 532 nm and 633 nm laser beams (filled circles), fitted to a Gaussian profile (Equation (6.1), continuous line). Widths extracted from the fits are 1.20 and 0.83 mm for the 532 and 633 nm laser beams, respectively. The grey area corresponds to the diameter of the aperture of the mask used in the bias illumination.

The light intensity profile on the solar cell is narrower for the red laser than for the green laser. Because the intensity of the lasers are adjusted by equalizing the current density at −4 V, the peak intensity (I_0) of the red laser will be higher than for the green laser. As a consequence, local current densities in the active layer at the center of the illumination spot will be much higher for the red than for the green laser illumination.

To better compare the J−V characteristics measured under green and red laser light illumination the beam profiles of both lasers have to be similar. We measured the spot size of the red laser again at a distance $d = d_i + 6$ cm allowing a wider spot size. At $d = d_i + 6$ cm a width of w =1.35 mm is obtained, which is close to the width of the green laser (w = 1.2 mm) at $d = d_i$. The green laser profile at d_i and the red laser profile at $d = d_i + 6$ cm are very similar (Figure 6.3(a)). Therefore, the peak intensity of the illumination spot of the red laser intensity profile at $d = d_i + 6$ cm is expected

not to differ significantly from that of the green laser intensity profile at $d = d_i$ when both laser intensities are adjusted to the give the same current density at −4 V as measured with simulated solar illumination.

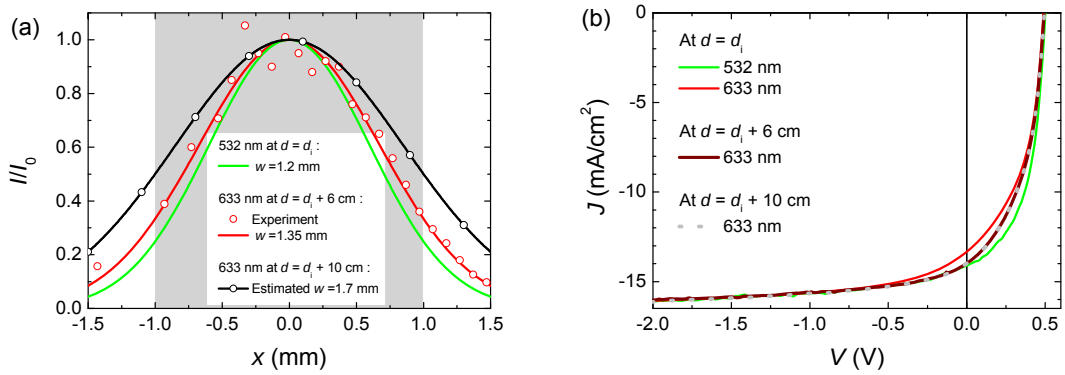

Figure 6.3: (a) Measured intensity profile of the 633 nm laser at $d = d_i + 6$ cm (red circles) and fit to Equation (6.2) (w = 1.35 mm, red line). Gaussian fit profile for 532 nm laser at $d = d_i$ (w = 1.2 mm, green line). Estimated intensity profile (black line and circles) for the 633 nm laser at $d = d_i + 10$ cm. (b) J–V characteristics of the PDPP4TOP:PCBM solar cell measured with the 532 nm laser at $d = d_i$ (green line) and with the 633 nm laser at $d = d_i$ + (red line), at $d = d_i + 6$ cm, (red wine line), and at $d = d_i$ +10 cm (grey dots).

Figure 6.3(b) compares the measured J–V characteristics recorded at $d = d_i + 6$ cm for 633 nm laser illumination, with those obtained at $d = d_i$ for both 532 and 633 nm light. The fill factor (*FF*) factor for 633 nm laser illumination improves significantly for $d = d_i + 6$ cm compared to $d = d_i$ and the shape of J–V characteristics is more similar to that obtained under 532 nm laser illumination. We conclude that the difference in *J-V* curves observed in Figure 6.1(a) for green and red illumination is primarily an artifact caused by a difference in the illumination intensity profile. Nevertheless, after adjusting the intensity profile of the red laser to that of the green laser intensity a small difference in current density remains, especially in the relevant range from $V = 0 - V_{OC}$ (Figure 6.3(b)). This may be due to a difference in the absorption profile at 532 nm and 633 nm in the vertical direction. The effect of different absorption profiles on the J–V characteristics will be investigated further on in this chapter using drift-diffusion and optical simulations. For the time being, we will investigate the effect of the intensity profile on the J–V curve.

When the distance of the solar cell is increased to $d = d_i + 10$ cm no further change is noticed in the J–V curve (Figure 6.3(b), grey dots) under 633 nm illumination. The width of the laser beam at 10 cm distance was determined from the following equation relating the beam divergence to the beam width at different positions:

$$\tan\left(\frac{\alpha}{2}\right) = \frac{w_2 - w_1}{d_{12}} = \frac{w_3 - w_2}{d_{23}} \tag{6.3}$$

where α is the laser beam divergence, w_i is the width of Gaussian profile at position d_i, and d_{ij} is the distance between position j and i. For clarity Equation (6.3) is illustrated in Figure 6.4. The validity of Equation (6.3) was verified for the 532 nm and 633 nm laser illuminations by measuring the width of the profile at three different positions after the laser beam was diverged by the lens. A width of w = 1.70 mm was calculated with Equation (6.3) for the 633 nm laser beam at $d = d_i + 10$ cm. From Figure 6.(b) shows that the effect of the laser beam width on the $J-V$ curve stops for w > 1.3 mm. For the 532 laser a similar behavior was observed. When the solar cell is moved away from the initial position the *FF* hardly changes. However, when the solar cell is moved closer to the lens the *FF* decreases. This suggest that also for green laser illumination the $J-V$ curve starts to vary significantly when the width of the intensity profile is reduced below 1.2 mm.

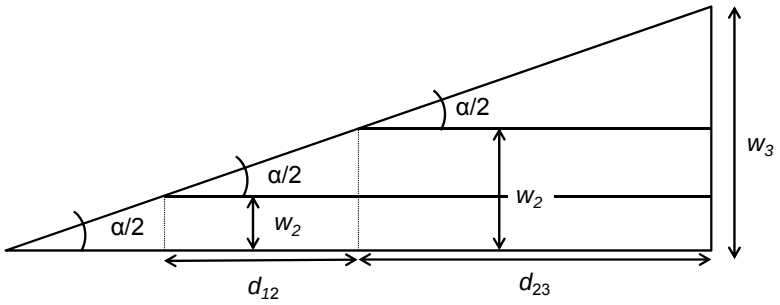

Figure 6.4: Beam divergence to illustrate Equation (6.3).

6.3.3 Analytical model describing the effect of a Gaussian intensity profile on the $J-V$ curves

To further explain the effect of the width of a Gaussian intensity profile on the measured $J-V$ characteristics we use an analytical model based on an analytical expression for the photocurrent and combine it with the 2D intensity profile projected on the active area of the solar cell. An expression of the photocurrent density as a function voltage and generation can be obtained from a simple analytical model that solves the rate equation for photogenerated carriers as shown by Koster and Kemerink *et al.*[7] In this model drift, diffusion, and bimolecular recombination of photogenerated carriers are considered, while space charge effects are neglected. In this chapter we will consider equal hole and electron mobilties. As a result, we can

omit any difference in the description of holes or electrons, such that some equations derived in Ref. [7] simplify. In the model the current density is given by the relation:

$$J = qf^{\text{drift}}pL \tag{6.4}$$

with q the elementary charge, f^{drift} the drift term of the extraction rate in the rate equation, p the hole density in the active layer, and L the active layer thickness. The drift term of the extraction rate is expressed by:

$$f^{\text{drift}} = 2\frac{\mu V_{\text{eff}}}{L^2} \tag{6.5}$$

where V_{eff} is the effective voltage on the active layer of the solar cell and μ the hole mobility. The hole density can be expressed as a function of the generation rate (G), bimolecular recombination constant (γ), and the extraction rate of carriers (f):

$$p = \frac{f}{2\gamma}\left[\sqrt{1+\frac{4\gamma G}{f^2}}-1\right] \tag{6.6}$$

the extraction rate is the sum of the drift and diffusion terms:

$$f = f^{\text{drift}} + f^{\text{diffusion}} \tag{6.7}$$

The diffusion term of the extraction rate is given by:

$$f^{\text{diffusion}} = 8\mu\frac{kT}{qL^2} \tag{6.8}$$

The bimolecular recombination constant (γ) is expressed as Langevin recombination:[8]

$$\gamma = \gamma_{\text{pre}} \frac{2q\mu}{\varepsilon_0 \varepsilon_r} \tag{6.9}$$

where γ_{pre} is a pre-factor which accounts for a reduced recombination in the active layer, ε_0 is the dielectric permittivity of vacuum, and ε_{r} is the relative permittivity. Combining Eqs. (6.4) to (6.9) an expression of a more general form of the photocurrent is obtained as a function of voltage and generation rate:

$$J(V_{\text{eff}}, G) = qLf^{\text{drift}}(V_{\text{eff}}) \frac{f(V_{\text{eff}})}{2\gamma} \left[\sqrt{1 + \frac{4\gamma G}{f(V_{\text{eff}})^2}} - 1 \right] \tag{6.10}$$

Equation (6.10) can be used to calculate the photocurrent − voltage curve for a given set of parameters (μ ,L, γ_{pre}, and ε_{r}).

To estimate the effect of the 2D illumination profile (Figure 6.5(a)) on the J−V curve we first divide the illumination profile in n infinitesimal surfaces (S_n) (1 disc and (n−1) rings) starting from the center of the illumination spot. Then, for each infinitesimal surface we calculate the photocurrent using Equation (6.10) using the intensity at the position of the infinitesimal surface and the area of the infinitesimal surface. Finally, the currents of all the individual infinitesimal surfaces are summed and divided by the area of the aperture to yield the total current density under 2D illumination.

For each surface S_n at n iteration, the position is defined by the radius (Figure 6.5(b)):

$$R_n = \Delta r(n - ½) \tag{6.11}$$

where $\Delta r = R_{\text{a}}/N$ is the increase of the radius from iteration n to n + 1 determined as the ratio of the aperture (R_{a}) and the number of iterations (N). The relative intensity at iteration n is considered constant for each surface of area A_n and is given by the Gaussian profile of the laser beam at position $x = R_n$ (Eq. (6.1)). When G_0 is the peak generation rate at the center of illumination spot, the generation rate at iteration

n is given by:

$$G_n = G_0 \exp\left(-2\frac{R_n^2}{w^2}\right) \tag{6.12}$$

and the current I_n of generated by the infinitesimal surface at iteration point n is given by:

$$I_n = A_n J(V_{\text{eff}}, G_n) \tag{6.13}$$

Where $A_n = \pi\Delta r^2(2n-1)$ is the area of a ring with outer radius $n\Delta r$ and inner radius $(n-1)\Delta r$, as illustrated in Figure 6.5(b). The total current density (J_{tot}) as a function of voltage and peak generation rate of the device is given by the sum of I_n over all rings divided by the aperture area $A_n = \pi R_a^2$:

$$J_{\text{tot}}(V_{\text{eff}}, G_0) = \frac{1}{A_a}\sum_{n=1}^{N} A_n J(V_{\text{eff}}, G_n) \tag{6.14}$$

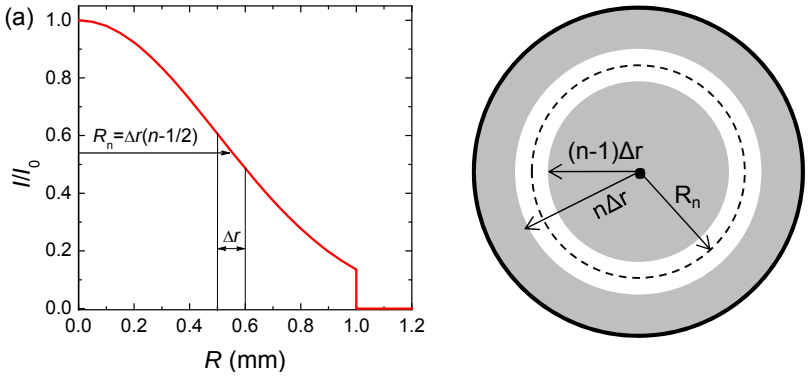

Figure 6.5: 2D intensity profile: (a) Relative intensity profile on the active area of the solar cell as a function of radius. (b) Top view of the aperture of the solar cell, illustrating the area A_n and the position R_n of the infinitesimal surface S_n (shown as a white ring).

Figure 6.6 shows the $J-V$ curves calculated using Eqs. (6.10) and (6.14) and the set of parameters summarized in Table 6.1 for a constant intensity profile with a fixed generation rate (G) and for a Gaussian profile, varying the width (w) and the peak

generation rate (G_0). For each curve G_0 was scaled such that the calculated current density at −4 V matches the calculated current density at −4 V for the constant intensity profile. This corresponds to the same situation as for the experimentally measured $J-V$ curves, where also the intensity of the laser was adjusted to match the saturation current density measured under simulated solar light.

Figure 6.6(a) shows the calculated $J-V$ curves for a solar cell with L = 200 nm illuminated by a flat intensity profile and for different Gaussian intensity profiles with widths varying from 0.5 to 1.5 mm. The calculations nicely reproduce the trend seen in the experimental $J-V$ curves. When the width of the intensity profile is reduced below the value of the aperture radius (1 mm), the calculated $J-V$ curves for Gaussian beam profile start to deviate significantly from the $J-V$ for flat intensity illumination. For a beam width smaller than 1 mm most current is generated close to the center of the illumination spot. To yield the same current at −4 V as for the flat intensity profile, G_0 has to be increased significantly when w becomes smaller than R_a. This creates a high carrier density at the center of the beam spot, enhancing bimolecular recombination. For intensity profiles with a width larger than 1 mm, the peak generation rate G_0 has to be increased less compared to the G of the constant profile and hence the local carrier densities are lower at the center and decrease more gradually towards the edges. As a result the local $J-V$ curves are less voltage dependent.

Table 6.1. Parameter set used to calculate the $J-V$ curves in Figure 6.6.

Parameter	Symbol	value	Unit
Electron (hole) mobility	M	10^{-8}	m^2/Vs
Langevin pre-factor	γ_{pre}	0.1	-
Relative permittivity	ε_r	3	-
Temperature	T	300	K
Active layer thickness	L	variable	M
Generation rate for a flat intensity profile	G	$5 \cdot 10^{27}$	$m^{-3}s^{-1}$
Peak generation rate for a Gaussian intensity profile	G_0	scaled to G	$m^{-3}s^{-1}$
Width of Gaussian profile	W	variable	mm
Radius of the aperture	R_a	1	mm
Number iteration	N	200	-

The divergence of the J-V characteristics for a constant and Gaussian light intensity profile increases with the active layer thickness as shown in Figure 6.6(b) for a Gaussian with w = 0.8. Thicker layers lower the effective electric field in the device resulting in a decrease of the extraction rate of carriers (Eq. 6.5) and an increase of bimolecular recombination. As a result the J-V curves will be more sensitive to the light intensity.

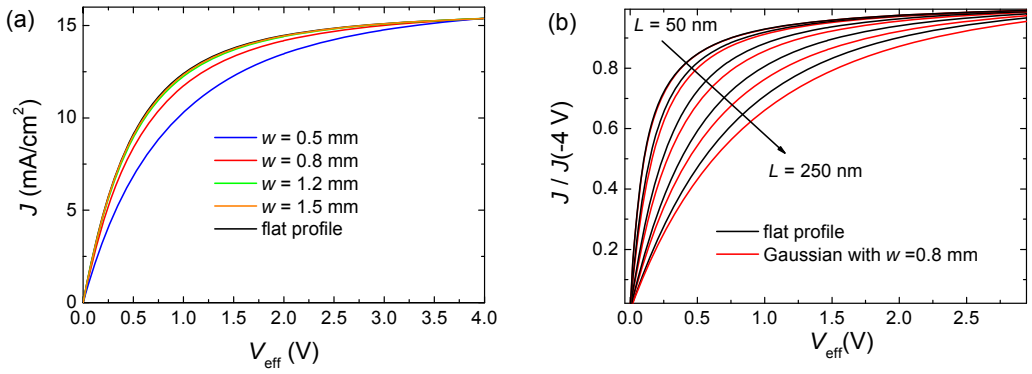

Figure 6.6: (a) Calculated $J-V$ curves for a 200 nm thick active layer under illumination of a flat intensity profile and under illumination of Gaussian intensity profiles with widths w = 0.5 to 1.5 mm. (b) $J-V$ curves calculated for a flat and Gaussian intensity profile with width w = 0.8 mm for layer thicknesses. The layer thickness is increased by steps of 50 nm from 50 to 250 nm.

6.3.4 Effect of monochromatic illumination on the *J-V* curve

In Figure 6.3(b) we compared the $J-V$ curves measured for 532 and 633 nm laser light with a Gaussian beam width of 1.2 and 1.35 mm, respectively. A small difference was observed between both $J-V$ curves for V in the range between 0 and V_{OC}. The question arises to which extend this difference can be due to the wavelength dependence of the absorption profile across the active layer. The absorption profile scales with the charge generation profile and the extraction efficiency of charges will depend on the position where they are generated. To address this question, we will combine optical with drift diffusion simulation.

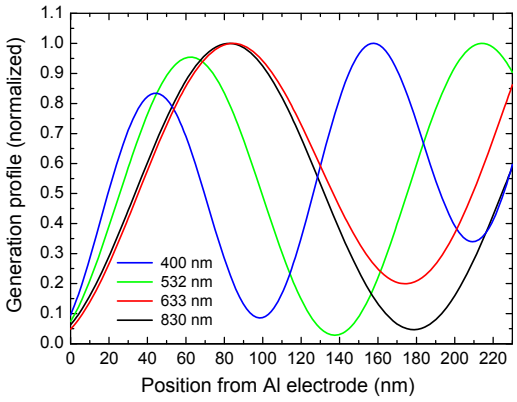

Figure 6.7: Calculated normalized charge generation profile across a 230 nm thick active layer for different illumination wavelengths.

To simulate the $J-V$ characteristics of a solar cell illuminated with different wavelength we calculated the generation profiles at four different wavelengths (400, 532, 633, and 830 nm) as shown in Figure 6.7.

The generation profiles at the different wavelength were scaled to match the experimental reverse (saturation) current density at −4 V of the PDPP4TOP:PCBM solar cell under 532 nm illumination. Because we do not have the exact electrical parameters of the PDPP4TOP:PCBM solar cell we simulate the $J-V$ characteristics with two different electrical parameter sets summarized in Table 6.2 which each gave a close fit to the $J-V$ measured under green laser illumination.

Table 6.2. Electrical input for parameter for two different set of simulations.

Parameter name	Symbol	Value set 1	Value set 2	unit
Electron (hole) mobility	μ	$0.8 \cdot 10^{-8}$	$10 \cdot 10^{-8}$	m^2/Vs
Langevin pre-factor	γ_{pre}	0.007	0.17	-
Relative permittivity	ε_r	3	3	-
Temperature	T	295	295	K
Active layer thickness	L	230	230	m
Effective energy gap	E_g	0.85	0.97	eV

The $J-V$ curves for the four different wavelengths simulated using parameter set 1 (Figure 6.8(a)) show a clear dependence of the $J-V$ curves on the charge generation profile. The lower *FF* going from 532 to 633 nm illumination is similar to the effect observed experimentally. The *FF* even decreases further for 830 nm illumination.

In contrast, the effect of the illumination wavelength on the $J-V$ curve simulated using parameter set 2 (Figure 6.8(b)) is much less pronounced. Only a small difference is observed between the $J-V$ curves for 532 and 633 nm illumination and the effect on the *FF* is opposite with an increase in *FF* for 633 and 800 nm compared to 532 nm illumination. The differences between the two parameter sets show that the generation profile affects the collection of charge carriers, but not in a unique way. Figure 6.8 reveals that the generation profile under different illumination wavelengths affects the transport properties in a rather complex way. The distribution of the carrier density will simultaneously influence the recombination rate, the diffusive currents by the density gradient of the carriers, and the electric field across the device influenced by the electron and hole density distribution. The combined effect of these interrelated processes on the performance of the solar cell is not easy to predict and will vary with each different active layer material.

The simulations presented in this section show that monochromatic illumination does have an effect on the $J-V$ characteristic of an organic solar cell. To avoid a deviation of the device performance from standard test condition, it is recommended to illuminate the solar cell with simulated solar light that approaches the AM 1.5 G

solar irradiance. This approach, however, cannot be used for tandem cells, where some spectral light bias is needed to isolate the subcell of interest.

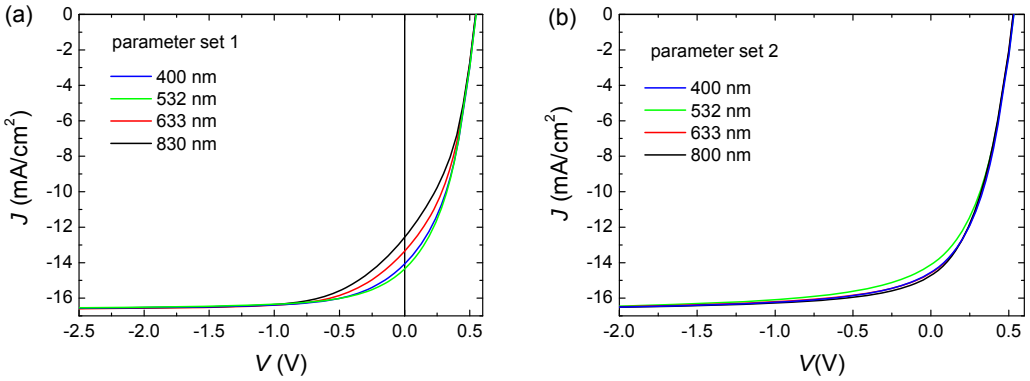

Figure 6.8: Simulated $J-V$ curves for different illumination wavelengths for parameter set 1 (a) and set 2 (b), see Table 6.2. The corresponding charge generation profiles are shown in Figure 6.7.

6.4 Conclusion

In this chapter we examined the effect of monochromatic laser illumination on the $J-V$ characteristics of an organic solar cell. We showed experimentally and analytically that the width of a Gaussian intensity profile has a pronounced effect on the $J-V$ characteristic when it is smaller than the radius the illuminated cell area. The effect is due light intensity dependent losses and increases for thicker photoactive layers where bimolecular recombination becomes more pronounced. From the experiments we infer that it is crucial to determine the spot size of the laser beam and ensure that the Gaussian width of the intensity profile is larger than the radius of the aperture used to mask the active area of the solar cell. Only under this condition the intensity profile under laser illumination is sufficiently constant over the illuminated area of the solar cell. Even for homogenously illuminated cell areas, an influence of the illumination wavelength on the $J-V$ characteristic remains. This effect is due to a different absorption profile in the active layer for different wavelengths, which results in a different charge generation and collection.

For accurately determining the solar cell performance it is advised to use a solar simulator light source that approaches the AM 1.5 G reference spectrum and gives a homogenous intensity profile instead of a monochromatic light. Especially for single junction organic solar cells, spectral response measurements are preferably performed with simulated solar light bias as described in Chapter 5. For spectral response measurements of tandem cells, monochromatic (or at least spectrally shifted) illumination for two different wavelengths is needed to determine the spectral response of the individual subcells.[1] To perform these measurements accurately two

requirements need to be fulfilled. First, the width of intensity profile of both complementary monochromatic light sources has to be identical and larger than the radius of the aperture of the mask. Second, one should verify that the $J-V$ characteristics of single junction cells corresponding to the subcells on the tandem do not vary significantly from the $J-V$ measured under simulated solar light.

6.5 References

[1] J. Gilot, M. M. Wienk, R. A. J. Janssen, *Adv. Funct. Mater.* **2010**, *20*, 3904.

[2] K.H. Hendriks, manuscript in preparation.

[3] L. J. A. Koster, E. C. P. Smits, V. D. Mihailetchi, P. W. M. Blom, *Phys. Rev. B* **2005**, *72*, 085205.

[4] J. D. Kotlarski, P. W. M. Blom, *Appl. Phys. Lett.* **2012**, *100***,** 079901

[5] J. R. Tumbleston, Y. C. Liu, E. T. Samulski, R. Lopez, *Adv. Energy Mater.* **2012**, *2*, 477.

[6] J. Mescher, N. Christ, S. Kettlitz, A. Colsmann, U. Lemmer, *Appl. Phys. Lett.* **2012**, ***101***, 073301.

[7] L. J. A. Koster, M. Kemerink, M. M. Wienk, K. Maturová, R. A. J. Janssen, *Adv. Mater.* **2011**, *23*, 1670.

[8] P. Langevin, *Ann. Chim. Phys. VII*, **1903**, *28*, 433.

Summary

Physical processes in organic solar cells

For a sustainable future of humankind on this planet a change from fossil fuels as primary energy source to renewable energy sources is needed. Photovoltaics – direct conversion of light into electricity – has a high power per area density compared to other renewable energy sources and can therefore provide a significant contribution to the future energy demand. The growing energy demand requires low cost, fast and large scale power production. Organic solar cells have the potential to meet these requirements, due to the fact that their photoactive layer can consist of cheap organic materials and can be fabricated from solution by fast roll to roll processes. The power conversion efficiency of an organic solar cell strongly relies on the different physical processes involved in the generation of electricity. Each physical process from absorption of light to the generation, transport, and collection of free carriers is crucial for the solar cell's efficiency. The work described in this thesis focuses on improving our understanding of physical processes that affect the operation and efficiency of organic solar cells. Also a strong aim of the work presented in this thesis is to explore new experimental techniques and improve existing experimental techniques to characterize organic solar cells and study physical processes occurring in organic solar cells.

In Chapter 2, electroabsorption (EA) spectroscopy is explored as a non-invasive optical experimental technique to probe electric fields in organic tandem and in organic single junction solar cells. The electric field across the active layer is crucial for efficient charge transport and collection. Especially for organic tandem solar cell it is presently not fully understood how the intermediate recombination contact distributes the electric fields over the individual sub cells. EA-spectra varying with the applied voltage bias have been recorded for single junction and tandem solar cells. The individual contributions of the wide and small band gap photoactive layers can be identified and distinguished in the EA-spectra of the tandem cell. However, the observation of a non-linear voltage bias dependence of the tandem's EA-signal prevents the determination of the correct electric field distribution in the tandem cell. In the small band gap single junction solar cell, the non-linear dependence of the EA-signal with applied bias voltage is also observed. We were able to attribute this non-linear voltage dependence of the EA-signal to the contribution of two different electro-modulated (EM) signals with different electric field dependencies. The EM-signals are determined to be the EA-signal due to the Stark effect and an EM-signal that results from induced charges in the active layer. Despite the identification of

these EM-signals, it was not possible to separate the voltage dependence of the EA-signal from the Stark effect and from the EM-signal from induced charges. Due to the mixing of different EM-signals we concluded that EA-spectroscopy is not a suitable technique to probe routinely electric fields in organic tandem solar cells.

Photocurrents are studied experimentally and theoretically in Chapters 3 and 4. The photocurrent in an organic solar cell is defined as the difference between illumination and dark current. Photocurrent − voltage (J_{ph}−V) measurements provide information about the electric field dependence of generation, transport, collection, and recombination of generated carriers. In Chapter 3, photocurrents in organic solar cell are studied experimentally and theoretically with drift-diffusion modeling. In the measured J_{ph}−V curves a reduced photocurrent is observed in forward bias with respect to reverse bias. This reduction is primarily an artifact, caused by the series resistance of the electrodes. Without correcting the measured photocurrent for the series resistance, it is even not qualitatively correct. After correcting for the series resistance, the photocurrent is actually not reduced in forward bias. With drift diffusion simulations the effects of increased recombination rate and different injecting properties of the contacts on the photocurrent are studied. The simulations show that the photocurrent can be reduced in forward bias by bimolecular recombination between photogenerated and injected charges. Furthermore, the simulations show that band-bending or self-selective contacts are not needed to reduce the photocurrent in forward bias. With a simple analytical model we show that the photocurrent under high forward bias can be expressed by:

$$J_{ph} = \frac{J_{max}}{1 + \xi \gamma_{pre}}$$

Where γ_{pre} is the Langevin prefactor, ξ a positive constant and J_{max} is the reverse saturation current. The equation represents the saturation current in forward bias which is related to the reverse bias saturation current and to the strength of bimolecular recombination. For very low γ_{pre}, the forward bias photocurrent is expected to saturate close to J_{max}. The reverse saturation current scales with the generation rate in the device and consequently the photocurrent cannot exceed the photon flux.

In contrast to this, we show in Chapter 4 that it is possible to observe in forward bias a larger photocurrent than the saturation current in reverse bias for non-annealed and annealed thick P3HT:PCBM solar cells. A larger photocurrent than the number of photons absorbed per unit time is related to a photomultiplication mechanism. Because the photocurrent is defined as the difference between illumination and dark

current, photomultiplication occurs in forward bias when the injection current is enhanced under illumination. Photomultiplication can also be observed in drift-diffusion simulation for very low Langevin prefactors or when electron and hole mobilties are different in combination with a low Langevin prefactor. The simulations show that photocurrent multiplication results from a modification of the space charge in the device under illumination.

In Chapter 5, we demonstrate experimentally and analytically that the commonly method used to measure spectral responsivity of a solar cell with bias illumination is not correct when the solar cell presents non-linear light intensity dependent losses. A new method is proposed that determines accurately the spectral response under bias illumination. With the new method a much more accurate estimate of the power conversion efficiency can be obtained under bias illumination. The external quantum efficiency (EQE) is defined as the ratio of the number of collected charges at short circuit to the number of photons incident on a solar cell. Typically, the EQE is measured as function of wavelength and is used to determine the short circuit current at the AM 1.5 G solar emission spectrum. It is common practice to illuminate the solar cell at an equivalent intensity of 1 sun to account for intensity dependent losses in the solar cell. In this thesis it is shown that this leads to underestimated EQE values when intensity dependent losses are present in the solar cell. An alternative method to determine EQE values at 1 sun equivalent intensity has been developed. It is shown experimentally and theoretically that the new method to determine EQE at 1 sun equivalent intensity is correct.

In Chapter 6, the use of lasers as monochromatic bias illumination on organic solar cell is investigated. Compared to traditional white light bias sources such as halogen or xenon lamps, laser illumination is much easier to handle due to the extremely low beam divergence. Furthermore, monochromatic illumination is required to measure the spectral response of the individual subcells of an organic tandem solar cell. Although, monochromatic laser illumination is more easy to use than white light to bias organic tandem solar cells, it is not clear under which conditions this can be done. The effect of the laser beam intensity profile and the effect of the monochromatic illumination on the *J-V* characteristics is addressed. We show experimentally and by a 2D analytical model that a non homogenous light intensity profile over the active area of the cell associated with laser light can reduce the performance of the solar cell through a loss in fill factor. This effect can easily be minimized by increasing the beam width. We further show by combined optical and drift diffusion modeling that the wavelength of the monochromatic light does influence the generation profile and can thereby influence the collection of charges via a complex combination of effects. Therefore, a difference in the simulated *J-V*

curves can be observed for different illumination wavelength. Because, the *J-V* characteristics of an organic solar cell can be dependent on the illumination profile and on the intensity profile of the laser, we advise the use of a solar simulator that approaches the AM 1.5 G reference spectrum and has an uniform intensity for the accurate determination of the organic solar cell's performance.

Samenvatting

Fysische processen in organische zonnecellen

Voor een duurzame toekomst van de mensheid op deze planeet is een verandering van fossiele brandstoffen als primaire energiebron naar hernieuwbare energiebronnen nodig. Fotovoltaïsche zonne-energie - directe omzetting van licht in elektriciteit - heeft een hoog vermogen per oppervlakte-dichtheid in vergelijking met andere hernieuwbare energiebronnen en kan daardoor een belangrijke bijdrage aan de toekomstige vraag naar energie leveren. De groeiende vraag naar energie vergt lage kosten en snelle, grootschalige productie van elektriciteit. Organische zonnecellen hebben het potentieel om aan deze eisen te voldoen vanwege het feit dat de fotoactieve laag kan bestaan uit goedkope organische materialen en de cellen kunnen worden vervaardigd via printen met snelle rol naar rol processen. Het rendement van een organische zonnecel is sterk afhankelijk van de verschillende fysische processen. Elk fysisch proces, de absorptie van licht voor de productie van vrije ladingsdragers, het ladingstransport en het verzamelen ervan, is van cruciaal belang voor de efficiëntie van de zonnecel.

Het werk beschreven in dit proefschrift richt zich op het verbeteren van ons begrip van de fysische processen die de werking en efficiëntie van organische zonnecellen beïnvloeden. Daarnaast richt dit proefschrift zich op de ontwikkeling van nieuwe experimentele technieken en de verbetering van bestaande technieken om organische zonnecellen te karakteriseren en de fysische processen die zich in organische zonnecellen te bestuderen.

In hoofdstuk 2 wordt electroabsorption (EA) spectroscopie onderzocht als een niet-invasieve optische experimentele techniek om elektrische velden in organische tandems en enkele junctie zonnecellen te meten. Het elektrische veld in de actieve laag is cruciaal voor efficiënt ladingstransport en collectie. In het bijzonder voor organische tandem zonnecellen is het op dit moment niet helemaal duidelijk hoe het intermediaire recombinatie contact de elektrische velden over de afzonderlijke sub-cellen distribueert. Voor enkele tandem zonnecellen zijn EA-spectra opgenomen waarbij de aangelegde spanning werd gevarieerd. De individuele bijdragen van de hoge en lage bandafstand fotoactieve lagen kunnen worden onderscheiden en geïdentificeerd in de EA-spectra van de tandem cel. De waarneming van een niet-lineaire spanningsafhankelijkheid van het tandem EA-signaal maakt de bepaling van de juiste elektrische veldverdeling in de tandem cel onmogelijk. Ook in de lage bandafstand enkele junctie zonnecel wordt de niet-lineaire afhankelijkheid van het

EA-signaal met toegepaste voorspanning waargenomen. We waren in staat om deze niet-lineaire spanningsafhankelijkheid van het EA-signaal toe te schrijven aan de bijdrage van twee verschillende elektro-gemoduleerde (EM) signalen met verschillende elektrische veldafhankelijkheden. De EM-signalen worden bepaald door een EA-signaal van het Stark-effect en een EM-signaal als gevolg van geïnduceerde ladingen in de actieve laag. Ondanks de identificatie van deze EM-signalen, was het niet mogelijk de spanningsafhankelijkheid van het EA-signaal als gevolg van het Stark-effect en die van het EM-signaal als gevolg van geïnduceerde ladingen, te scheiden. Door het mengen van verschillende EM-signalen concludeerden we dat EA-spectroscopie geen geschikte techniek is voor het meten van elektrische velden in organische tandem zonnecellen.

Fotostromen zijn experimenteel en theoretisch onderzocht in de hoofdstukken 3 en 4. De fotostroom in een organische zonnecel is gedefinieerd als het verschil tussen belichting- en donkerstroom. Fotostroom - spanning (J_{ph} - V) metingen geven informatie over de elektrische veldafhankelijkheid van ladingsproductie, het transport, de collectie aan de electrodes, en recombinatie van gegenereerde ladingsdragers. In hoofdstuk 3 worden fotostromen in organische zonnecellen experimenteel en theoretisch bestudeerd met drift-diffusie modellen. In de gemeten J_{ph} - V krommen wordt een gereduceerde fotostroom waargenomen in de doorlaatrichting in vergelijking tot de sperrichting. Deze vermindering is vooral een artefact veroorzaakt door de serieweerstand van de elektroden. Zonder correctie van de gemeten fotostroom van de serieweerstand is het zelfs niet kwalitatief correct. Na correctie voor de serieweerstand wordt de fotostroom inderdaad niet verkleind in de doorlaatrichting. Met drift-diffusie simulaties van de effecten op de fotostroom, van verhoogde recombinatiesnelheid en verschillende injectie-eigenschappen van de contacten, worden bestudeerd. De simulaties laten zien dat de fotostroom kan worden verminderd in de doorlaatrichting door bimoleculaire recombinatie tussen licht geïnduceerde- en geïnjecteerde ladingsdragers. Bovendien laten de simulaties zien dat het buigen van de energiebanden of zelf-selectieve contacten niet nodig zijn om de fotostroom in de doorlaatrichting te reduceren. Met een eenvoudig analytisch model laten we zien dat de fotostroom onder hoge voorwaartse spanning kan worden uitgedrukt door:

$$J_{ph} = \frac{J_{max}}{1 + \xi\gamma_{pre}}$$

waarin γ_{pre} de Langevin voorfactor is, ξ een positieve constante en J_{ph} de omgekeerde verzadigingsstroom. De vergelijking geeft de verzadigingsstroom in de

doorlaatrichting die gerelateerd is aan de verzadigingsstroom in de sperrichting en de sterkte van bimoleculaire recombinatie. Voor zeer lage γ_{pre} is te verwachten dat de fotostroom in de doorlaatrichting vlakbij J_{max} verzadigt. De verzadigingsstroom in de sperrichting schaalt evenredig met de generatiesnelheid in de zonnecel waaruit volgt dat de fotostroom niet hoger kan zijn dan de fotonflux.

In tegenstelling hiermee laten we in hoofdstuk 4 zien dat het mogelijk is om een grotere fotostroom in de doorlaatrichting waar te nemen dan de verzadigingsstroom in de sperrichting voor geannealde en niet-geannealde dikke P3HT: PCBM zonnecellen. Een grotere fotostroom dan het aantal fotonen geabsorbeerd per tijdseenheid hangt samen met een fotomultiplicatie mechanisme. Omdat de fotostroom wordt gedefinieerd als het verschil tussen belichtings- en donkerstroom, treedt fotomultiplicatie op onder voorwaartse spanning als de injectiestroom verbeterd onder verlichting. Fotomultiplicatie kan ook worden waargenomen in drift-diffusie simulaties voor zeer lage Langevin voorfactors of wanneer elektron en gat mobiliteiten verschillend zijn in combinatie met een lage Langevin voorfactor. Uit de simulaties blijkt dat fotostroom vermenigvuldiging het resultaat is van een verandering in het aantal beschikbare sites voor ladingen in de zonnecel tijdens verlichting.

In hoofdstuk 5 tonen we experimenteel en analytisch aan dat de algemeen gebruikte methode om de spectrale respons van een zonnecel te meten met compensatieverlichting, niet juist is wanneer de zonnecel niet-lineaire lichtintensiteitsafhankelijke verliezen laat zien. Een nieuwe methode wordt voorgesteld die de spectrale respons met compensatieverlichting nauwkeurig bepaalt. Met de nieuwe werkwijze kan met compensatieverlichting een veel nauwkeurigere schatting gemaakt worden van het rendement. De externe kwantumefficiëntie (EQE) wordt gedefinieerd als de verhouding van het aantal verzamelde ladingen bij kortsluitstroom en het aantal fotonen dat op de zonnecel instraalt. De EQE wordt gemeten als functie van de golflengte en wordt gebruikt om de kortsluitstroom bepalen zoals die onder het AM 1,5 G zonneemissiespectrum zou zijn. Het is gebruikelijk om de zonnecel te verlichten op een gelijkwaardige intensiteit van 1 zon om rekening te houden met intensiteit afhankelijke verliezen in de zonnecel. In dit proefschrift wordt aangetoond dat dit leidt tot onderschatte EQE-waarden wanneer intensiteit afhankelijke verliezen aanwezig zijn in de zonnecel. Een alternatieve methode is ontwikkeld om EQE-waarden te bepalen onder 1 zon intensiteit. Het is experimenteel en theoretisch aangetoond dat de nieuwe methode om EQE te bepalen onder de intensiteit van 1 zon correct is.

In hoofdstuk 6 wordt het gebruik van lasers als monochromatische compensatieverlichting op organische zonnecel onderzocht. Vergeleken met de

traditionele wit licht bronnen zoals halogeen of xenon-lampen, is laser verlichting veel makkelijker te hanteren door de extreem lage divergentie van de lichtbundel. Bovendien is monochromatische verlichting nodig om de spectrale respons van de individuele subcellen van een organisch tandem zonnecel te meten. Hoewel monochromatische laserverlichting makkelijker te gebruiken is dan wit licht om organische tandem zonnecellen mee te verlichting is het niet duidelijk onder welke omstandigheden dit kan worden gedaan. Het effect van het intensiteitsprofiel van de laserstraal en het effect van de monochromatische verlichting op de *J - V* karakteristiek worden behandeld. We tonen experimenteel en met een 2D analytische model aan dat een niet-homogeen lichtintensiteitsprofiel over het actieve gebied van de cel, zoals met laserlicht, de prestaties van de zonnecel verminderen door een verlies in vulfactor. Dit effect kan gemakkelijk worden geminimaliseerd door het vergroten van de bundelbreedte. Verder laten we zien met gecombineerde optische- en drift-diffusie modellen, dat de golflengte van het monochromatisch licht het generatieprofiel beïnvloedt en daardoor ook de collectie van ladingen via een complexe combinatie van effecten. Zo kan een verschil in de gesimuleerde *J - V* krommen worden waargenomen voor verschillende belichtingsgolflengten. Omdat de *J - V* kenmerken van een organische zonnecel af kunnen hangen van het belichtingsprofiel en het intensiteitsprofiel van de laser, adviseren wij, voor de nauwkeurige bepaling van de prestaties van organische zonnecellen, het gebruik van een zonnesimulator die het AM 1,5 G referentiespectrum dicht nadert en een uniforme intensiteit heeft.

Curriculum Vitae

Dominique Wehenkel was born on the 19th of March 1979 in Luxembourg city, Luxembourg.

After receiving his high school degree with honors from the Lycée Technique des Arts et Métiers in Luxembourg city in 2000, he started his first year university in chemistry at the Centre Universitaire du Luxembourg. Subsequently he continued with the second year of university in France at the Université Montpellier II where he obtained the "diplôme d'études universitaires générales science et technologie, mention science de la matière" in 2002. He then continued to study physical chemistry and received a "licence de chimie physique" with honors in Monpellier in 2003. Dominique left Montpellier to obtain his "maîtrise de chimie physique" at the Université Pierre et Marie Curie in Paris in 2004, again with honors. At that point, he returned to Luxembourg to work as an assistant conservator for nearly one year in the Museum of History and Nature of Luxembourg city in the department of geology.

In 2005, Dominique moved to the Netherlands to study a master of nanoscience at the University of Leiden and Delft University of Technology. He performed his master thesis project in the Molecular Electronics and Devices group in Delft under the supervision of prof. Alberto Morpurgo and dr. Jeroen Oostinga on the electronic transport properties of graphene nanoribbon devices. In 2008 he obtained his "master of science" in nanoscience.

In June 2008 he started his PhD project at the Eindhoven University of Technology in the group "Molecular Materials and Nanosystems", under the supervision of prof. René Janssen and dr. Martijn Wienk. The most relevant results of his PhD research are presented in this thesis.

List of Publications

"Probing electric fields in polymer tandem and single junction cells with electroabsorption spectroscopy"
D. J. Wehenkel, M. M. Wienk, R. A. J. Janssen
In preparation

"The effect of bias light on the spectral responsivity of organic solar cells"
D. J. Wehenkel, K. H. Hendriks, M. M. Wienk, R. A. J. Janssen
Organic Electronics **2012**, *13*, 3284

"*Influence of injected charge carriers on photocurrents in polymer solar cells"*
D. J. Wehenkel, L. J.A. Koster, M. M. Wienk, R.A. J. Janssen
Phys. Rev. B **2012**, *85*, 125203.

"Measuring the light emission profile in organic light-emitting diodes with nanometre spatial resolution'
S. L. M. van Mensfoort, M. Carvelli, M. Megens, D. Wehenkel, M. Bartyzel, H. Greiner, R. A. J. Janssen, R. Coehoorn
Nature Photonics **2010**, *4*, 329.

"Observation of Aharonov-Bohm conductance oscillations in a graphene ring"
S. Russo, J. B. Oostinga, D. Wehenkel, H. B. Heersche, S. S. Sobhani, L. M. K. Vandersypen, A. F. Morpurgo
Phys. Rev. B **2008**, *77*, 085413.

Acknowledgements

Foremost, I wish to thank my supervisors René Janssen and Martijn Wienk for everything they taught me and for their support during these four years of my PhD. Certainly, I learned a lot from them concerning organic photovoltaics (electronics), experimental skills, and other scientific skills. However, I am in particular grateful for the soft-skills they taught me, such as to communicate effectively. René, what I appreciated a lot from you is that you are always friendly and keep a smile, this makes the M2N group are very pleasant place to work. Martijn, you taught me everything about solar cell fabrication and characterization. I enjoyed all the fruitful discussions we had together and especially appreciated your stimulating critical questioning. Then, I have also to thank in particular Jan Anton Koster, who joined our group as a young and bright post doc during my second year of PhD, which became a good friend and a third mentor. Jan Anton, you taught me a lot concerning device physics, transport properties, and numerical simulation of organic solar cells. Furthermore, I truly enjoyed the constructive discussions and the nice collaboration we had. Additionally, I am very grateful to Prof. Dr. Jenny Nelson, Dr. Carsten Deibel, Prof. Dr. Reinder Coehoorn, and Prof. Dr. Rint Sijbesma for being part of my reading and defense committee.

To Stefan Meskers I am grateful for his valuable and constructive suggestions and advices. I also enjoyed the chats about different topics we had close to the coffee machine. I would also like to thank Wijnand Dijkstra and Gerard Wijers for creating cabling for the electroabsorption setup, for designing and fabricating a sample holder for the flow cryostat, and for useful tips about noise reduction and vacuum systems. Next, I would like to thank Jan Gilot for borrowing the tandem solar cells used for the measurements in Chapter 2 and for the useful discussion we had about organic tandem solar cells. To Koen Hendriks, I am very grateful that he made his weird polymer PDPP4TOP which showed in organic solar cells a significant reduction of the EQE under illumination and that he did not accept this observation as a simple fact. This led to a very nice and important collaboration, which is presented in Chapter 5.

Then I would like to warmly thank Gert-Jan Wetzelaer, Jan Harkema, and Martijn Kuik for hosting me in their lab in Groningen, showing me around and helping me in my quest for making the perfect hole-only devices. It was a very fruitful experience to see how other people make and characterize devices.

Karel Sastrowiardjo, Stefan Oosterhout, Daniele Di Nuzzo, Dhritiman Gupta, and Benjamin Bory became very good friends during my PhD in the M2N group. I would

like to thank them for their support, their suggestion, their advices, and for the good time we had together. A special thank to Daniele and Dhritiman for contributing to this thesis by helping with equipments, discussing certain scientific topics, and your suggestion how to measure the spot size of a laser. In the end, Dhritiman's suggestion (the blade method) was the method which worked best and which was used in Chapter 6 to determine the laser beam profiles. Karel thanks a lot for sharing your joy and enthusiasm, it meant a lot to me. Stefan it was a lot of fun flying with you RC planes and RC helicopters in the sport centrum. Benjamin thanks for leaving funny sticky notes on my desk and for paying my ciders in Fort.

Also I would like to thank my (former) office mates from STO 4.30 (Veronique Gevaerts, Johan Bijleveld, Arjan Zoombelt, Mindaugas Kirkus, Benjamin Bory) and STO 4.24 (Marie-France Falzon, Weiwei Li, Ratheesh Kunnathodi, Gijs van Pruissen, Dhritiman, Daniele, Alice Furlan) for sharing their expertise, for useful discussion, and all the fun we had together. Veronique thanks for explaining important details on TEM. Arjan, Johan, Marie-France, and Mindagaus thank you for answering my questions about organic chemistry. Gijs thanks a lot correcting my Dutch Zamenvatting. The other PhD students and post docs I would like to acknowledge for various reasons are: Aránzazu Aguirre, Sandra Kouijzer, Girish Lakhwani, Marco Carvelli, Harm van Eersel, Rein de Vries, Wijnand Germs, Klára Maturová, Dirk Veldman, Erik Roeling, Stephan van Reenen, Francisco Bloom, Serkan Esiner, Tom van der Hofstad, Fatemeh Gholamrezaie, Wenshan Zhang, Svetlana van Bavel, Erwin Rossen, Kevin van de Ruit, and Bram Karsten.

Aránzazu, Girish, and Marco thanks for sharing your interest in photophysics. Aránzazu was always ready to explain me her latest experiment, while Girish showed me with great enthusiasm how to use ellipsometry on thin organic films. Siebe, I would like to thank you for sharing your expertise in drift diffusion simulation of OLEDs and in mobility measurements of charge carriers in hole-only devices. Rein thanks a lot for all the useful discussion concerning EA spectroscopy. Also a special thanks to Francisco for his good advices on experiments and explaining me OMAR. Erik and Wijnand (Germs) thanks for the crash course in impedance measurements.

Also I would like to acknowledge Reinder Coehoorn for the pertinent questions and suggestions he gave me during M2N meetings. Martijn Kemerink, I would like to thank you for introducing me to impedance spectroscopy. I would like to thank all the people from SMO and M2N for their help and their kindness. Then I would like to thank the Joint Solar Programme (JSP) for funding this research and for organizing interesting and nice summer meetings.

Last but not least, I would like to thank my parents, my sister and my Anastasia for their support, their love and their patience during these four years. Thanks a lot to

“maya lioubliou Kissinka” for your help and advices concerning the design of this thesis or my presentations and all the love you gave me during theses years. Furthermore I owe you also all the friends I made from your department. Daniel (“The alligator”), Carol (the alligator’s wife), Gustavinio, Oliver, Nicole (wife of King Julian), Aida and Naza, Gamze (and Eric), Widy from Indonesia and her Bulgarian lover, the Brazilian Ana and Ivan, the lovely Iranian beauties: Sarah, Eli and Zuzu, Joana and Gordan, and Bruno (the big Serbian) thanks a lot for all nice time and fun we had together in Eindhoven. Also thank a lot to Fennec, Plons, and Rampage for their support during the writing of this thesis.